LIBRARY
[redacted]
NAVAL POSTGRADUATE SCHOOL
MONTEREY, CALIFORNIA 93940

NPS-PH-93-007

NAVAL POSTGRADUATE SCHOOL

Monterey, California

CHAOS METRICS FOR TESTING LAGRANGIAN PARTICLE MODELS

BY

R. F. KAMADA

January 31, 1993

TECHNICAL REPORT

FOR PERIOD 03 March 1992 through December 1992

Approved for public release; distribution unlimited

Prepared for:
United States Air Force Space & Missile Center
Monterey, California 93943-5005

FEDDOCS
D 208.14/2
NPS-PH-93-007

Feddocs
D 208.14/2:NPS-PH-93-007 c.2

NAVAL POSTGRADUATE SCHOOL
Monterey, California

Rear Admiral T. A. Mercer
Superintendent

Provost H. Shull

The work reported herein was supported by and prepared for the U.S. Air Force Space Systems Division at Los Angeles AFB, California.

Reproduction of all or part of this report is authorized.

Author for this report was

DUDLEY KNOX LIBRARY
NAVAL POSTGRADUATE SCHOOL
MONTEREY CA 93943-5101

REPORT DOCUMENTATION PAGE

Form Approved
OMB No 0704-0188

1a REPORT SECURITY CLASSIFICATION: Unclassified	1b RESTRICTIVE MARKINGS
2a SECURITY CLASSIFICATION AUTHORITY	3 DISTRIBUTION/AVAILABILITY OF REPORT: approved for public release distribution unlimited
2b DECLASSIFICATION/DOWNGRADING SCHEDULE	
4 PERFORMING ORGANIZATION REPORT NUMBER(S): NPS-PH-93-007	5 MONITORING ORGANIZATION REPORT NUMBER(S)
6a NAME OF PERFORMING ORGANIZATION	6b OFFICE SYMBOL (If applicable) / 7a NAME OF MONITORING ORGANIZATION
6c ADDRESS (City, State, and ZIP Code)	7b ADDRESS (City, State, and ZIP Code)
8a NAME OF FUNDING/SPONSORING ORGANIZATION: USAF Space & Missile Center	8b OFFICE SYMBOL (If applicable): USAF/SMC/CLGR / 9 PROCUREMENT INSTRUMENT IDENTIFICATION NUMBER: MPIR FY76169200541
8c ADDRESS (City, State and ZIP Code): MONTEREY, CALIFORNIA 93943-5005	10 SOURCE OF FUNDING NUMBERS — PROGRAM ELEMENT NO / PROJECT NO / TASK NO / WORK UNIT ACCESSION NO

11 TITLE (Include Security Classification)

CHAOS METRICS FOR TESTING LAGRANGIAN PARTICLE MODELS

12 PERSONAL AUTHOR(S)

R.F. KAMADA

13a TYPE OF REPORT	13b TIME COVERED	14 DATE OF REPORT (Year, Month, Day)	15 PAGE COUNT
technical	FROM 3-92 TO 12-92	JAN 31, 1992	111

16 SUPPLEMENTARY NOTATION

17 COSATI CODES		
FIELD	GROUP	SUB-GROUP

18 SUBJECT TERMS (Continue on reverse if necessary and identify by block number)

atmospheric dispersion/diffusion, Lagrangian particle models chaos, self-affine fractals, turbulence, atmospheric boundary layer, strange attractors, Monte Carlo models, Lyapunov

19 ABSTRACT (Continue on reverse if necessary and identify by block number)

The Lorenz and Henon attractors and two atmospheric Lagrangian particle models were tested using self-affine fractal dimension, D_A, Shannon information entropy, S, and the Lyapunov exponent, λ, along with turbulent kinetic energy, vertical variance, and Brunt-Vaisala Frequency. Results show that 1) chaos metrics are a new set of tools to assess the micro behavior of Lagrangian particle models, 2) that periodicity in bifurcatory systems differs from wave behavior in fluids, since wave states are not limited to amplitude extrema.
3) Non-spectral particle models lead to unrealistic variations in the chaos metrics with changes in buoyant stability.
4) S and D_A behave oppositely at times, implying that diffusion and dispersion are not equivalent, even in the absence of mean windflow.

20 DISTRIBUTION/AVAILABILITY OF ABSTRACT	21 ABSTRACT SECURITY CLASSIFICATION
[X] UNCLASSIFIED/UNLIMITED [ ] SAME AS RPT [ ] DTIC USERS	UNCLASSIFIED
22a NAME OF RESPONSIBLE INDIVIDUAL: R.F Kamada	22b TELEPHONE (Include Area Code): (408) 646-2674 / 22c OFFICE SYMBOL: PH

TABLE OF CONTENTS

I. INTRODUCTION 1

II. THEORY 3

A. FRACTAL DIMENSION (D_A) 3

B. SHANNON ENTROPY (S) 7

C. LYAPUNOV EXPONENT (λ) 10

D. GEOPHYSICAL TURBULENCE MEASURES 11

E. 1 AND 2-D CHAOS. 14

1. The Logistics Difference Equation 14

2. Graphical Analysis of Logistics Equation . 15

3. Bifurcation Diagrams 19

4. The Henon Equations 19

G. 3-D ATMOSPHERIC PARTICLE DIFFUSION MODELS . . . 24

1. The McNider Diffusion Model 24

2. The LPM Diffusion Model 28

3. Random Number Generator Kernel 37

III. ANALYSIS 40

A. LOGISTICS DIFFERENCE AND HENON EQUATIONS . . . 40

1. Analyzing the Logistics Difference Equation 40

2. Henon Function Analysis 54

3. Conclusions on chaos metrics and equations 67

B. ATMOSPHERIC DIFFUSION MODEL ANALYSIS 67

1. Method 67

2. Results from the McNider Model Analysis . . 68
3. Results from the LPM Model Analysis 81
4. Conclusions on Atmospheric Diffusion 97
IV. OVERALL CONCLUSIONS 98
REFERENCES 103
DISTRIBUTION LIST 107

I. INTRODUCTION

Unlike the simple linear relationships studied in basic physics, natural phenomena often exhibit complex nonlinear behavior which leads to what is known as chaos. For example, the behavior of neutrally buoyant particles floating in the atmosphere is determined to quantum mechanical levels. But in turbulence any departure from exact knowledge of all conditions affecting the particle will admit an uncertainty much more severe than Heisenberg's. I.e., in turbulent regimes the paths of two particles, initially side by side, will diverge with time at a rate faster than exponential. Chaotic systems are defined as those in which the distance between any two arbitrarily close particles will diverge at an exponential or greater rate with time. With our limited measurement accuracy and resolution, one practical implication of atmospheric chaos is that weather forecasts also diverge quickly from reality; so detailed deterministic predictability becomes impossible beyond periods of several days (Gleich, 1987; Devaney, 1990).

Though chaos severely limits predictability, exponential divergence and other chaos induced features can also serve to test our ability to simulate turbulent behavior. Rather than weather systems, our interest here is in the computer simulation of smaller scale atmospheric diffusion by the use of Lagrangian particles. This concerns public, military, and industrial safety because such simulations are used to predict plume dispersion from sources such as biochemical warfare agents, natural gas tanks and tankers, nuclear reactor and weapons, chemical plants, rocket and missile launch emissions, aborts, and test firings.

However, tests of Lagrangian particle models have been limited. The aggregate diffusion of many Lagrangian particles has been compared with the results of Gaussian plume statistical theories and measurements of dispersing clouds. These tests show that some particle models vary greatly from reality in certain atmospheric conditions (Venkatram and Wyngaard, 1988).

Another set of tools which may be useful in analyzing particle diffusion models are recently developed chaos metrics such as fractal dimension, D_A, Shannon information entropy, S, and the Lyapunov exponent, λ (McHardy and Czerny, 1987; Baker and Gollub, 1990). Each of these metrics can be used to focus on different aspects of particle behavior. Unlike previous turbulence measures, D_A can resolve apparent nocturnal gravity waves from true turbulence and even the dissipation of such waves into turbulence because it measures the intensity ratio of small to large scale fluctuations (Kamada 1992b). This is important because gravity waves disperse quite differently from turbulence. The other chaos

metrics are different in that the Shannon entropy measures the evenness of distribution of particles within a set of possible states, while the Lyapunov exponent measures the divergence rate of particles and thus is an actual test for chaos.

Our question is whether such metrics can be used to assess the ability of Lagrangian particle models to mimic real atmospheric diffusion. These metrics are first applied to the one and two-dimensional attractors known as the logistics difference recursion relation and the Henon system. First fixed then strange attractors appear when these simple equations are recursed iteratively over varying coefficient values. The three chaos metrics based on these recursion patterns display both similarities and differences. We then study two three-dimensional Monte Carlo Lagrangian scattering routines designed to simulate atmospheric diffusion as representatives of more complex real world systems.

II. THEORY

A. FRACTAL DIMENSION (D_A)

The self-similar fractal dimension, D_B, can be described readily with the Cantor set (Devaney, 1990). To form this set, a straight line is drawn with the middle third removed, as in the second line of fig. 1. The two resulting straight lines, which are one-third the original line length, are then similarly subdivided. The four new lines, all 1/9th the original line length, are further subdivided, *ad infinitum*. From top to bottom in fig. 1, the resulting sets of lines are **self-similar**; i.e., the alteration of the geometry is repeated at all successive levels of resolution.

Another self-similar figure, the Koch snowflake [fig. 2], is produced from an equilateral triangle by replacing the middle third of each side with two pieces of equal length to create a six-pointed star (Devaney, 1990). This star has 12 sides, all of length 1/3. The riddle third of each of the 12 sides is again removed and replaced with two pieces of length 1/9. Again, the process is repeated *ad infinitum*. Like the Cantor set, the Koch snowflake is also self-similar. The jagged sides appear to be geometrically similar at increasing levels of resolution.

The self-similar fractal dimension is defined by (Devaney, 1990) as

$$D_B = \frac{\ln (\textit{Total length of pieces})}{\ln (\textit{resolution})} \quad . \qquad \text{(II-1)}$$

In the Cantor set example, the total length of segments of unit length at level n is 2^n, and the resolution level is 3^n, so that

$$D_B = \frac{\ln 2^n}{\ln 3^n} = \frac{n \ln 2}{n \ln 3} \approx 0.6309 \quad . \qquad \text{(II-2)}$$

Similarly for the Koch snowflake, there are 4 pieces for each level of n with a magnification of 3, so that

$$D_B = \frac{\ln 4^n}{\ln 3^n} \approx 1.262 \quad . \qquad \text{(II-3)}$$

With geometric figures, D_B is unitless; it involves a length divided by a length. But we cannot use this self-similar fractal dimension directly on a time series trace, since it involves the

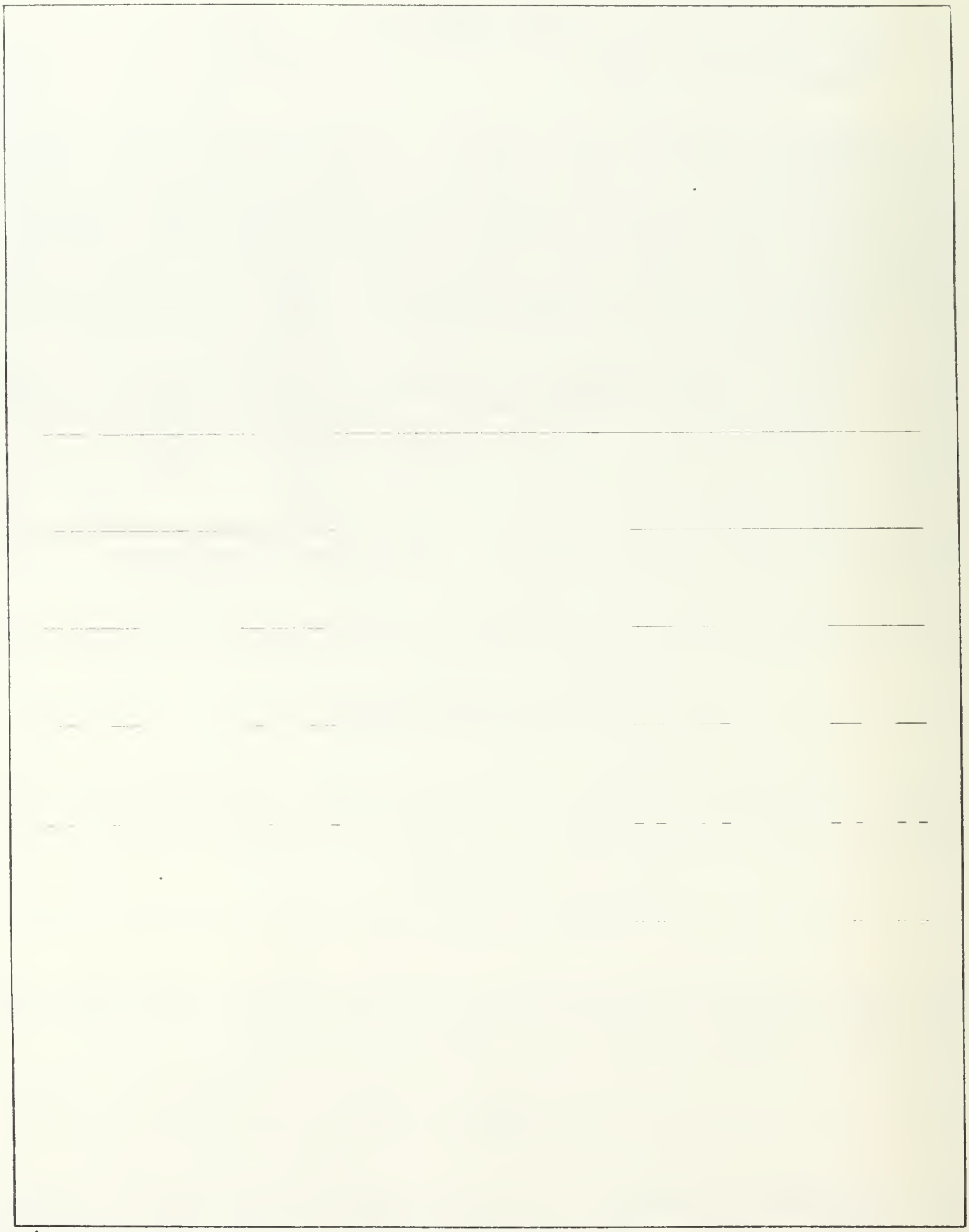

Figure 1, Construction of the Cantor Set.

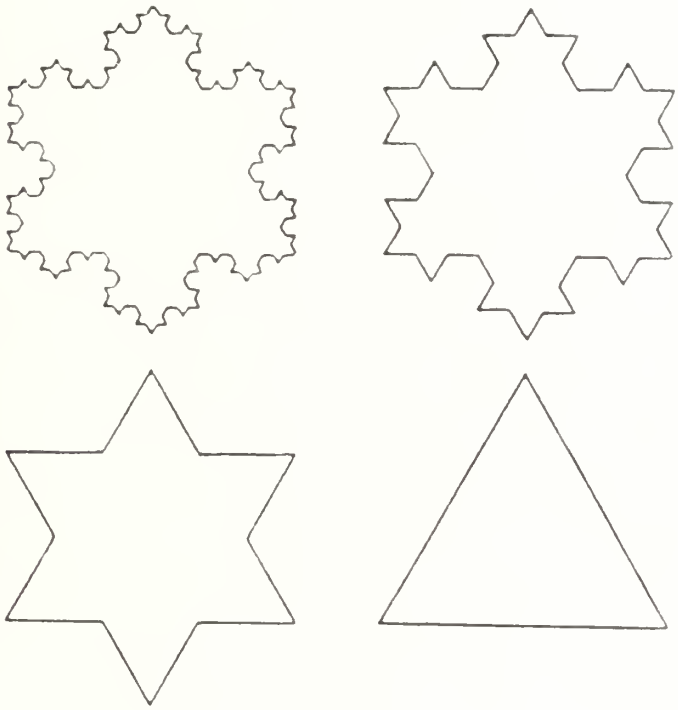

Figure 2. Construction of the Koch Snowflake. From Devaney (1990).

square root of the amplitude squared plus the time squared, i.e.,

$$D_B = \frac{\ln \left[\sum_0^T \sqrt{\Delta A^2 + \Delta t^2} \right]}{\ln \delta t} \quad . \qquad \text{(II-4)}$$

So this form needs some adjustment to ensure that it is independent of any arbitrary unit scaling between amplitude and time.

There are other ways to characterize the fractal dimension of a system. For a more suitable times series measure, McHardy and Czerny (1987) redefined the length metric as

$$L(\epsilon) = \frac{1}{\epsilon} \int_0^T |F(t+\epsilon) - F(t)| \, dt \, , \qquad \text{(II-5)}$$

where F is the amplitude of the time series at time, t, ϵ is the time increment, and T is the time window over which L is defined.

This definition obviates the units scaling problem. Since the inverse time in $1/\epsilon$ cancels the time units in the integral, $L(\epsilon)$ is only in units of amplitude. The fractal dimension then becomes

$$D_A \equiv - \frac{d \ln L(\epsilon)}{d \ln \epsilon} \quad . \qquad \text{(II-6)}$$

McHardy and Czerny (1987) applied D_A to the time variance of X-ray luminosity data from the Seyfert galaxy NG5506. Recently, Kamada (1992b) used D_A to distinguish waves from turbulence in nocturnal atmospheric boundary layer data. D_A is self-affine, meaning that each time the resolution, ϵ, changes, the length is re-normalized affinely, i.e., in the same way, by ϵ itself.

To actually compute D_A, the integral is approximated with a numerical summation, so that

$$L(\epsilon) = \frac{\delta t}{\epsilon} \sum_0^T |F(t-\epsilon) - F(t)| \quad . \qquad \text{(II-7)}$$

Since at each resolution $\delta t=\epsilon$, the length formulation can be shortened to,

$$L(\epsilon) = \sum_{t}^{T} |F(t-\epsilon) - F(t)| \quad . \tag{II-8}$$

Thus $L(\epsilon)$ is the total amplitude change over a time series of length, T, for a given resolution, ϵ. Here it is quite clear that time is removed from the length determination, so $L(\epsilon)$ does not depend on some arbitrary scaling between amplitude and time.

B. SHANNON ENTROPY (S)

When a particle is first released, its initial location is known and completely specified, so the information entropy (defined later) for its location is zero. Later, according to given equations of motion, its position diverges from the initial point. If the range of its possible positions is partitioned into equal segments, then for a given time interval, T, its motion can be recorded in terms of occupancy time for each segment. Then the particle diffusion rate might be measured by the seeming degree of randomness of occupancy time or evenness of the state probability distribution over time period, T. Shannon or information entropy is defined by the state probability distribution, so entropy may be regarded as a measure of diffusion rate for a time series of particle states. This can apply to the actual particle position, its velocity, or its phase velocity. Shannon entropy is defined simply as (Baker and Gollub, 1990)

$$S = - \sum_{i=1}^{N} p_i \ln p_i \quad , \tag{II-9}$$

where

$S \equiv$ *system entropy,*

$N \equiv$ *number of permitted states, and*

$p_i \equiv$ *probability of state i, such that* $\sum_{i=1}^{N} p_i = 1.0$.

Then, for N permitted states (or position intervals), the maximum possible entropy corresponds to equal occupancy time in each of the N states, so p_i is 1/N for all i. That is,

$$S_{max} = - \sum_{i=1}^{N} \frac{1}{N} \ln \frac{1}{N} \quad . \tag{II-10a}$$

Expanding the summation results in

$$S_{max} = \frac{1}{N} \ln \frac{1}{N} + \frac{1}{N} \ln \frac{1}{N} + \frac{1}{N} \ln \frac{1}{N} + \ldots \quad , \tag{II-10b}$$

and collapsing the common multiples gives

$$\begin{aligned} S_{max} &= -N \left(\frac{1}{N} \ln \frac{1}{N} \right) \quad , \\ S_{max} &= \ln N \quad , \end{aligned} \tag{II-10c}$$

which corresponds to total randomness, or completely even particle distribution across all allowable states. Also,

$$S_{min} = 0 \quad , \tag{II-11}$$

which corresponds to all particles being in one state.

The computation is similar for a randomly moving particle in a 2-D space. The 2-D space is divided into say a 100 X 100 grid. If the particle motion is completely random at time, t, it may be in any grid box with equal probability. Entropy for this system is then

$$\begin{aligned} S &= - \left[\left(\frac{1}{100^2} \ln \frac{1}{100^2} \right) + \left(\frac{1}{100^2} \ln \frac{1}{100^2} \right) + \ldots \right] \quad , \\ S &= - 100^2 \left(\frac{1}{100^2} \ln \frac{1}{100^2} \right) \quad , \end{aligned} \tag{II-12a}$$

which collapses to

$$S = \ln 100^2 = S_{max} \quad . \qquad \text{(II-12b)}$$

1. Shannon Entropy for an N-D System

For a 1-D system, the domain is simply partitioned into n intervals and the probability computed for each interval. For a simple system such as recursion of the logistics difference equation,

$$x_{n+1} = \mu x_n (1 - x_n) \quad . \qquad \text{(II-13)}$$

The probability for the ith interval, p_i, is simply the number of times the interval has been occupied after n number of recursion steps, divided by the total number of steps.

Note that the number of partitions should be appropriate for the total number of steps. Too few intervals will fail to resolve states and give a misleadingly low S value. For instance, with only one interval, $p_1 = 1$, and $S = 0$. Ideally, the number of intervals for maximum entropy resolution is $e^{\lambda N}$, where λ is the positive Lyapunov exponent for the system and N is the number of steps (Baker and Gollub, 1990, pp. 126-129). With λ typically of order unity, $e^{\lambda N}$ can easily be a computationally intractable number.

Again, for 3-D systems, assuming N equal segments along each axis, the number of partitions will be N^3, so computation quickly becomes unwieldy for large N. Some authors have used an N of order 10^2 to 10^3 as a compromise between entropy resolution and computational efficiency (Baker and Gollub, 1990, pg. 88). In analyzing real data the number of partitions should be related ideally in some direct fashion to the maximum resolution, ϵ_i, of the measuring devices and the total measurement time, T. The total number of partitions should probably not exceed T/ϵ_i, otherwise even a completely random distribution would still result in unoccupied intervals.

2. Ln vs Log_2

Wolf maintains that the Shannon entropy should be computed with $\log_2$ rather than the natural logarithm, $\log_e$ (Wolf, 1986, pg. 276). With $\log_2$, the Shannon entropy relates directly to binary coded information, since a bit can occupy only one of two states, i.e., true/false, on/off, one or zero. That is, the $\log_2$ basis sets the

entropy equal to the minimal length of binary code required to describe the state of the system. If all particles occupy only one state, turning "on" the bit for that state suffices to specify the system state. If the particles are evenly distributed among all states, the length of binary code required to specify the system is equal to the number of states, which means that the system is completely random (Tribus and McIrvine, 1971). But for this study, the Shannon entropy can also be written in the following form:

$$S = -K\sum_{i=1}^{N} p_i \ln p_i \quad . \tag{II-14}$$

The only difference between using the natural logarithm versus base two is the value imposed on the arbitrary constant, K. Most work assumes that K = 1.

B. LYAPUNOV EXPONENT (λ)

For an expanding cloud of particles, a direct measure of chaos is the two-particle divergence rate which can be characterized by Lyapunov exponents. The Lyapunov exponent, λ, also measures the system's sensitivity to initial conditions. In an N-dimensional syster, there will be N Lyapunov exponents; these do not correspond necessarily to coordinate axes. So in a Cartesian system, λ_1, λ_2, and λ_3 are locally defined Lyapunov exponents which generally cannot be described as λ_x, λ_y, and λ_z. Direction is adjusted for each point along the trajectory. In one-dimension, the Lyapunov exponent is defined by

$$\lambda = \lim_{N\to\infty} \frac{1}{N} \sum_{i=0}^{N-1} \ln \left| f'(i) \right| \quad , \tag{II-15}$$

which can be described over a map domain as the integral,

$$\lambda = \int_0^N p_i \ln \left| f'(i) \right| di \quad . \tag{II-16}$$

λ measures the **average** local stretching rate of the particle trajectory, as indicated by the log of the slope length, $|f'(i)|$, weighted by the probability of encountering that slope (Wolf, 1986). λ is also related to information loss rate. E.g., if a measured position is known to a precision of 16 bits, and $\lambda = 2$ bits per second, then the particle's future trajectory cannot be predicted to any degree of precision beyond a period of 8 seconds.

The Lyapunov exponent is readily computed for one dimension, but in higher dimensions the calculation becomes more complex. In three dimensions, the directions of trajectory divergence and contraction must be defined in terms of local tangents which vary from point to point, so calculations for the exponents must constantly adjust for each change in direction. Wolf has developed algorithms for computing higher dimensional Lyapunov exponents which involve reorienting the major axis of an ellipse for each point, then renormalizing the function after every few points so that the unit ellipsoid does not overlap an attractor (Wolf, 1986).

In 3-D, three Lyapunov exponents are required to classify the system. A negative exponent indicates a dissipative dimension. If all three exponents are negative, the system is dissipative, e.g., a pendulum settling down to a fixed point. If an exponent is zero, the system orbits about a fixed point in what is known as a limit cycle. If one of the three exponents is positive, the system is chaotic; the orbital trajectories diverge.

C. GEOPHYSICAL TURBULENCE MEASURES

Geophysicists use several standard turbulence metrics described below. Turbulent kinetic energy and Brunt-Vaisala frequency are used later to examine the McNider and LPM diffusion models.

1. Turbulent Kinetic Energy (tke)

The mean turbulent kinetic energy, or TKE, is defined as

$$tke \equiv \frac{1}{2}(\sigma_u^2 + \sigma_v^2 + \sigma_w^2) \quad , \qquad \text{(II-17)}$$

where

$\sigma_u \equiv$ standard deviation, u component of particle velocity,
$\sigma_v \equiv$ standard deviation, v component of particle velocity,
$\sigma_w \equiv$ standard deviation, w component of particle velocity.

2. Gradient Richardson Number (Ri)

The gradient Richardson number is defined as

$$Ri \equiv \frac{g}{\theta} \frac{\frac{\partial \overline{\theta}}{\partial z}}{\left[\left(\frac{\partial \overline{u}}{\partial z}\right)^2 + \left(\frac{\partial \overline{v}}{\partial z}\right)^2\right]} \quad . \qquad \text{(II-18)}$$

The overbars signify time averages, and

$g \equiv$ earth's gravitational acceleration,
$z \equiv$ vertical position above the surface,
$\theta \equiv$ potential temperature, i.e., the temperature normalized for adiabatic expansion with pressure. So

$$\theta \equiv T\left(\frac{p}{p_0}\right)^{\frac{R_d}{C_p}} \quad . \qquad \text{(II-19)}$$

Here R_d is the dry air gas constant and C_p is specific heat at constant pressure. Ri is used in lieu of the Reynolds number as a dynamic indicator of turbulence when the atmosphere displays a non-neutral density profile. The numerator is related to the buoyant production or destruction rate of tke, depending on negative or positive sign, respectively. The denominator is related to the shear generation rate of tke, which is nearly always positive. Thus, a positive Richardson number indicates a stable atmosphere (increasing potential temperature with height) and suppression of turbulence. Commonly, when the buoyant destruction rate of tke exceeds 1/4 the shear production rate, turbulence is suppressed, i.e., when Ri > 1/4 (Stull, 1988, pg. 176).

3. Brunt-Vaisala Frequency (BVF)

The Brunt-Vaisala frequency, BVF, is defined by

$$BVF \equiv \sqrt{\frac{g}{\overline{\theta}_v} \frac{\partial \overline{\theta}_v}{\partial z}} \quad , \qquad \text{(II-20)}$$

and in principal gives the highest gravity wave frequency which a fluid can support. It is undefined for negative temperature gradients, i.e., an unstable atmosphere (Sorbjan, 1989, p. 35).

4. Buoyancy Length (l_B)

The buoyancy length, l_b, is the standard deviation of the vertical velocity divided by the Brunt-Vaisala frequency,

$$l_B \equiv \frac{\sigma_w}{BVF} \quad . \tag{II-21}$$

The buoyancy length is meant to be a measure of the dominant eddy scale (Stull, 1988, pg. 310).

5. Obukhov Length (L)

The Obukhov length is given by

$$L \equiv -\frac{u_*^3 \theta}{g k \overline{w'\theta_0'}} \quad , \tag{II-22a}$$

where

$$\overline{w'\theta_0'} \equiv \textit{surface temperature flux} \; , \qquad k \equiv \textit{von Karman constant} \approx 0.4 \quad . \tag{II-22b}$$

$$\textit{and} \;\; u_* = \frac{V}{\sqrt{\ln \frac{z}{z_0} - \psi_m}} \quad . \tag{II-22c}$$

u_* is friction velocity, a measure of surface drag due to turbulent friction. ψ_m, is a stability correction approximated by

$$\psi_m = \begin{cases} -5\frac{z}{L} \; , & \frac{z}{L} > 0 \; (\textit{stable}) \; , \\ \dfrac{0.15961583 - 5.4151107\frac{z}{L}}{1 - 3.59002232\frac{z}{L} - 0.799168457\left(\frac{z}{L}\right)^2} \; , & \frac{z}{L} \le 0 \; (\textit{unstable}) \; . \end{cases} \tag{II-22d}$$

(Kamada, 1992d).

In a convective boundary layer, L is proportional to the height at which the tke buoyant generation rate matches the shear generation rate. L is the primary stability measure for the atmospheric surface layer and is also used in combination with the inversion height, z_i, to characterize boundary layer stability. An $L > 0$ indicates a stable boundary layer where vertical turbulence is suppressed by positive density gradients with height, z. An $L < 0$ indicates an unstable surface layer where upward vertical motion is encouraged by negative density gradients. Stability implies that a vertically displaced air parcel tends to return to its original height, i.e., its neutrally buoyant level (Businger, 1973).

D. 1-D AND 2-D CHAOS EQUATIONS.

The initial focus of this study is to compare and test some simple potential diffusion metrics. The fractal dimension, D_A, Shannon entropy, S, and Lyapunov exponent, λ, are simple expressions which can monitor transitions between periodic and chaotic behavior, akin to the transition between laminar and turbulent behavior in real fluids. Two such expressions described in the literature are the logistics difference equation:

$$x_{n+1} = \mu x_n (1 - x_n) \quad , \tag{II-23}$$

and the Henon system:

$$\begin{aligned} x_{n+1} &= 1 - a x_n^2 + y_n \quad , \\ y_{n+1} &= b x_n \quad . \end{aligned} \tag{II-24}$$

(Gould and Tobochnik, 1988, pp.152-178; Baker and Gollub, 1990).

1. The Logistics Difference Equation

Though simple and one dimensional, recursive iteration of the logistics difference equation results in chaotic behavior for certain parameters. For $0 < x_0 < 1$ and $\mu < 1$, x_n converges to 0. For $1 < \mu < 3$, and the same range for x_0, x_n converges to $\mu/4$. For $3 < \mu < 3.6$, x_n fluctuates between 2^n discrete points; while beyond $\mu \simeq 3.6$, the solution is nearly random, i.e., chaotic [fig. 3].

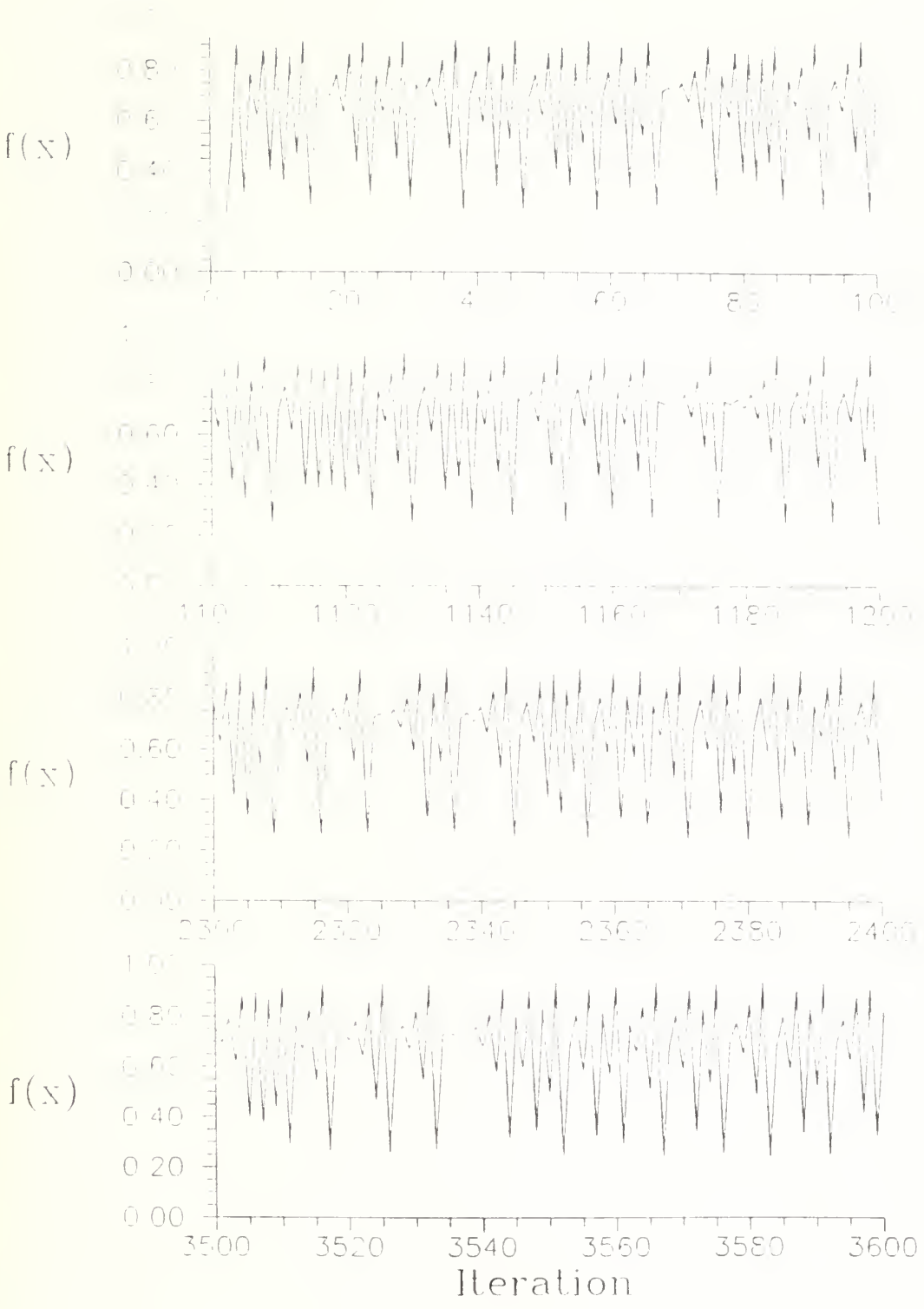

Figure 3. Logistics Difference Equation: 1-D Chaotic Motion. $x_{n+1} = 3.72x_n(1-x_n)$, with $x_0 = 0.01$.

2. Graphical Analysis of the Logistics Difference Equation

The logistics difference equation is parabolic, so that for an initial x_0 (given as 0.04 with μ=2.9 in fig. 4), drawing a vertical line to the parabola corresponds to x_1. Then a horizontal line drawn to the inscribed straight line of slope unity corresponds to recursing x_{n-1} to a new value for x_n. Reiterating this procedure marches the solutions to a final value of 0.655.

This final value can be determined exactly from the original function. At steady state, $x_{n+1} = x_n$. Then for fig. 4, where μ = 2.9,

$$x_{n+1} = 2.9\,x_n(1-x_n) \ , \qquad \text{(II-25)}$$

and solving for x_n:

$$x_n = 0 , \quad x_n = 0.65517 \ . \qquad \text{(II-26)}$$

Note since the equation is quadratic, that there are two solutions. The x_n=0 solution is unstable in a mathematical rather than physical sense (as defined below). The general rule is: if the magnitude of the slope of the function in the region of the solution is greater than 45°, the fixed point is an unstable solution; if the slope is less than 45°, the fixed point is a stable solution.

When the function is chaotic, there are still only two solutions to the quadratic equation. However, both points are unstable: they both repel rather than attract the value of x_{n+1}. The two points can still be computed, resulting in

$$x_n = 0 , \quad x_n = 0.74 \ . \qquad \text{(II-27)}$$

Another way of looking at this is by taking the derivative of x_{n+1} with respect to x_n:

$$\frac{d\,x_{n+1}}{d\,x_n} = \mu\,(1 - 2x_n) \ . \qquad \text{(II-28)}$$

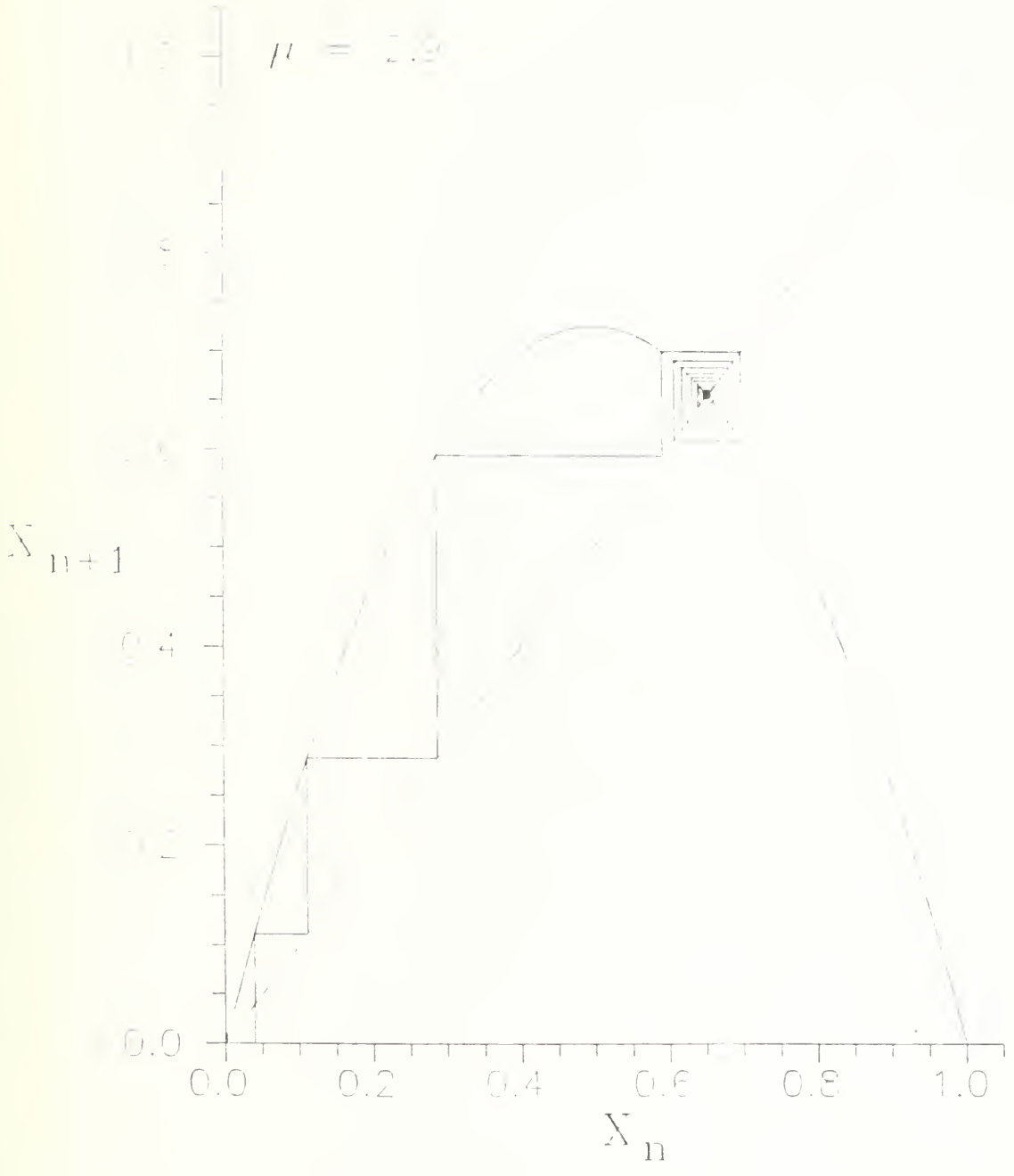

Figure 4. Logistics Difference Equation Graphical Analysis. $x_{n+1} = 2.9x_n(1-x_n)$.

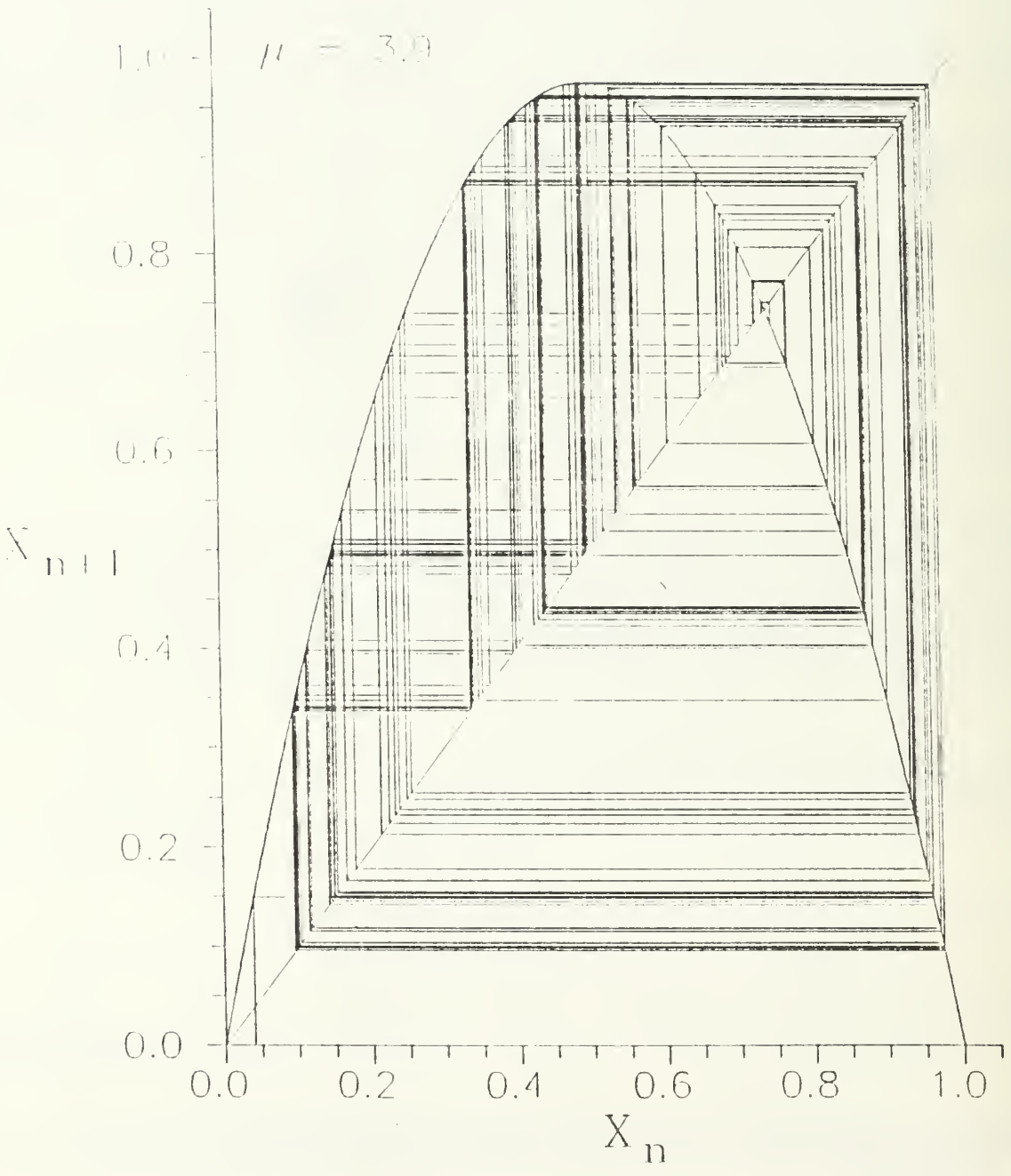

Figure 5. Logistics Difference Equation Graphical Analysis. $x_{n+1} = 3.9x_n(1-x_n)$

Checking the chaotic system of fig. 5, when $x_n = 0.74$, the slope is

$$\frac{dx_{n+1}}{dx_n} = 3.9(1 - 2(0.74)) \approx -1.87 \quad , \qquad \text{(II-29)}$$

which is less than -1, and hence unstable.

This concept is vital when visualizing what the Lyapunov exponent is measuring. Any time both solutions are at points where the slope is greater than 45° or less than -45°, the Lyapunov exponent is greater than zero (ln of the slope, which is greater than unity), and the system is chaotic.

3. Bifurcation Diagrams

A map of the possible values of x_n for various μ is called a bifurcation diagram [fig. 6]. With the bifurcation diagram, the complete behavior of the function can be determined. For example, for $0 \leq \mu \leq 3$, x_n tends to only one value; the repetitive recursion of x_{n+1} to x_n points to one attracting fixed point, corresponding to a dissipative system. At $\mu \geq 3$, the bifurcation diagram splits into two fixed points. The solution of x_{n+1} bounces back and forth between these two points. This is period doubling to period 2. Note for still larger values of m that there is another split to period 4, then 8, followed by a rapid series of bifurcations culminating in chaos, where the points appear to be distributed over a wide range of x_n.

Another curiosity appears in the bifurcation diagram. There are numerous "windows" within the chaotic region. The most obvious is around $\mu \simeq 3.82$, where the period 4 and 8 behavior seems to appear again. Increased resolution would show many more such windows. Also note that period widths get progressively narrower, and that higher periods are difficult to distinguish from chaos.

4. The Henon Equations

As with the logistics difference equation, the Henon set has stable solutions for a range of parameters, a and b, which correspond to one fixed point. Other values for a and b result in two fixed points, or period doubling [fig. 7], and period 4 and higher. For still higher values of a and b, the result is chaotic behavior; the possible positions appear to be spread throughout a discrete range of x and y [fig. 8].

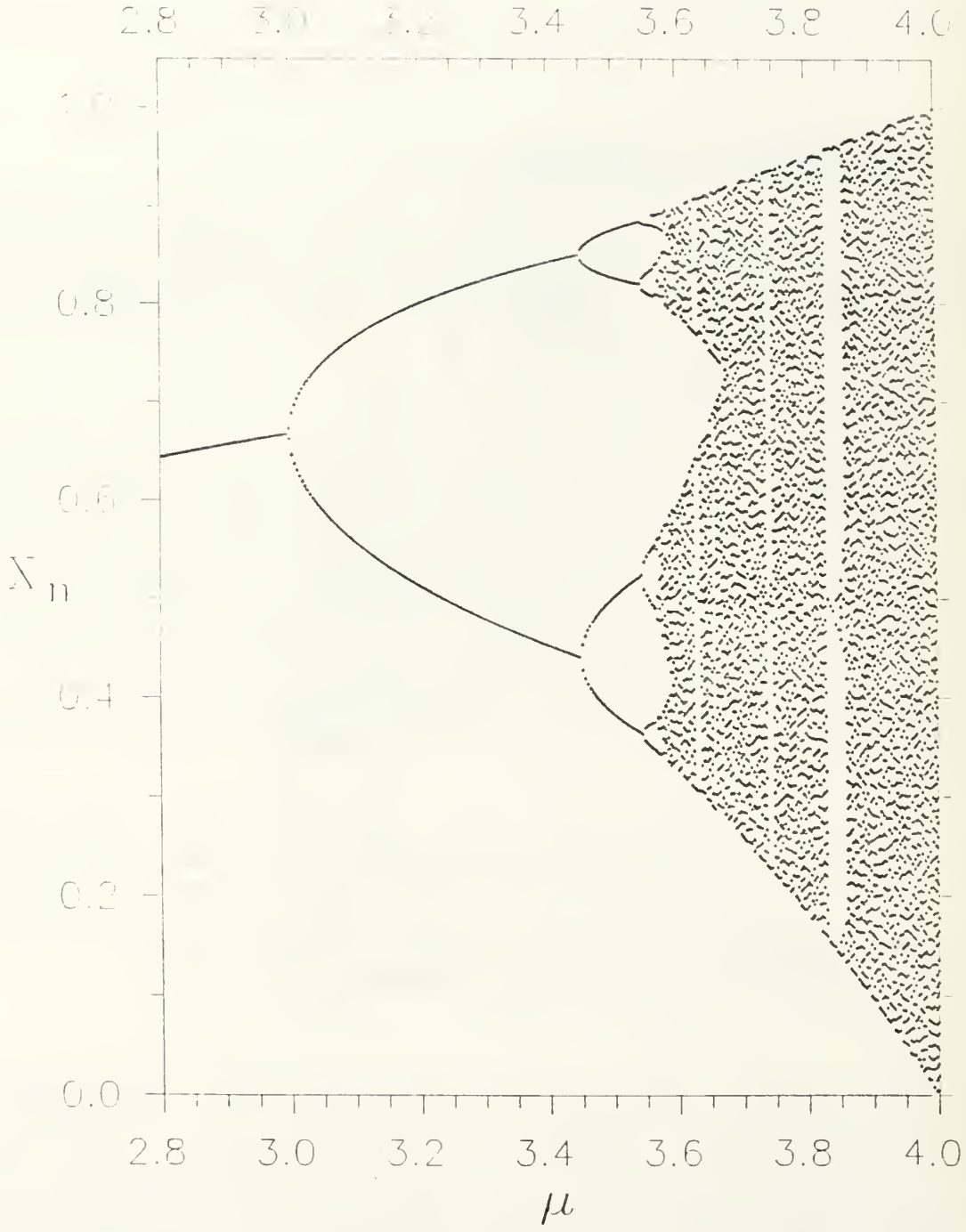

Figure 6. Logistics Difference Equation Bifurcation Diagram.
$x_{n+1} = \mu x_n(1-x_n)$.

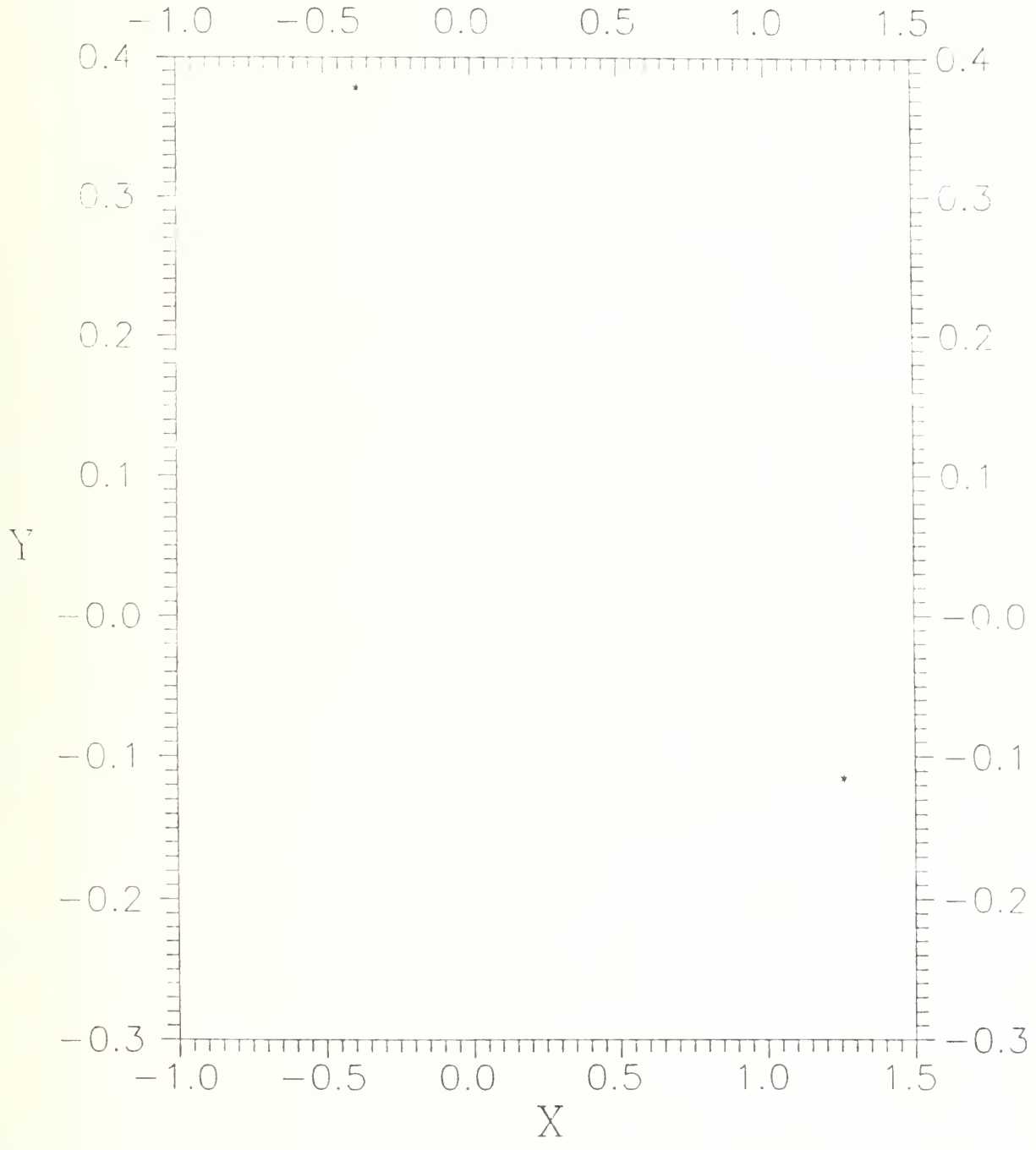

Figure 7. Henon System: Period 2, $x_{n+1} = 1-0.8x_n^2+y_n$, $y_{n+1} = 0.3x_n$.

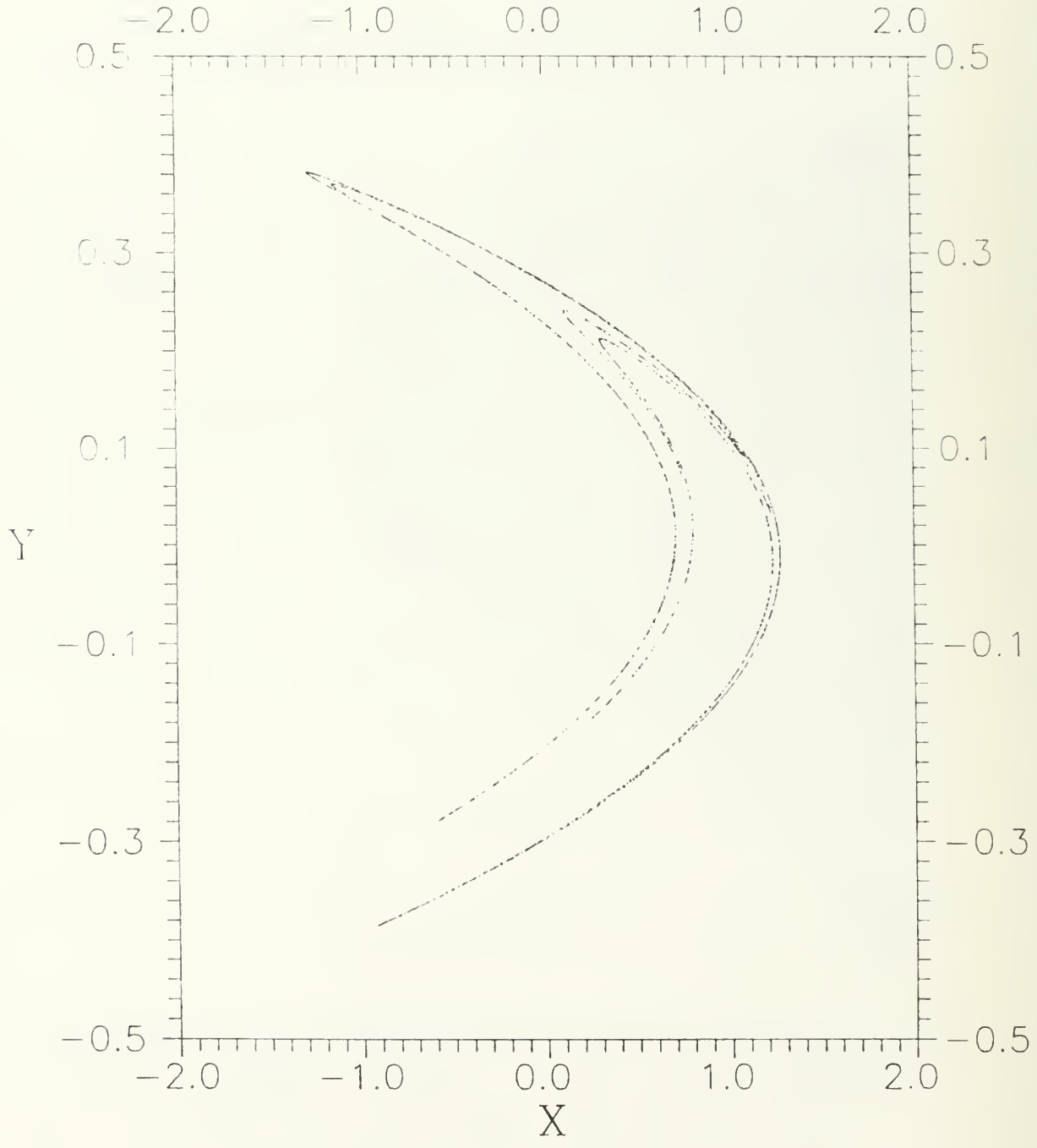

Figure 8. Henon System: Chaos, $x_{n+1} = 1-1.4x_n^2+y_n$, $y_{n+1} = 0.3x_n$.

The Henon bifurcation diagram resembles the logistics difference diagram, but has some obvious differences [fig. 9]. 1) it does not show symmetric splitting, but rather is skewed downward from the centerline. 2) At the value, a = 1.08 (with b = 0.3), a window appears in the bifurcation map with new values for x_n; the periodicity in this region occurs at points outside the previous range of x_n. These new points seem to appear out of nowhere, and are not linked to previous points by bifurcation.

E. 3-D ATMOSPHERIC PARTICLE DIFFUSION MODELS

Once we have gained some familiarity with chaos metrics, the second focus here is to study them as performance measures for three dimensional atmospheric diffusion models. The McNider diffusion model simulates pollutant clouds as the aggregate of numerous Lagrangian point particles. It has been used to estimate atmospheric transport and diffusion based on wind flow predictions from the Colorado State Regional Atmospheric Modeling System (RAMS) (Pielke, 1984). For this study, a wide range of possible atmospheric stabilities, $-0.2 \leq 1/L \; 0.1$, was studied. To render computations tractable and focus on diffusion, steady state mean flow profiles were obtained directly from boundary similarity (Sorbjan, 1990; Kamada, 1992a,c) rather than from a mesoscale windflow model. Several weaknesses were perceived in the McNider formulation. So an amended Lagrangian particle (LPM) model was also developed and tested.

1. The RAMS McNider Diffusion Model

For this study, mean flow components are neglected in order to focus on turbulent fluctuations. The RAMS McNider Diffusion Model computes Cartesian particle positions in a Lagrangian manner using

$$x_i(t + \Delta t) = x_i(t) + u_i(t)\Delta t. \qquad \text{(II-30)}$$

u_i refers to the turbulent velocity components along the three axes (Pielke ,1984). The velocity components are given by

$$u_i(t) = u_i(t - \Delta t)R_{u_i}(\Delta t) + u_i'(t - \Delta t). \qquad \text{(II-31)}$$

R_{ui} refers to the Lagrangian autocorrelation for each velocity component, an exponentially decaying function of Δt. The second terms on the right are random but normally distributed fluctuations having zero mean and standard deviations given by the following empirical formulas for the horizontal,

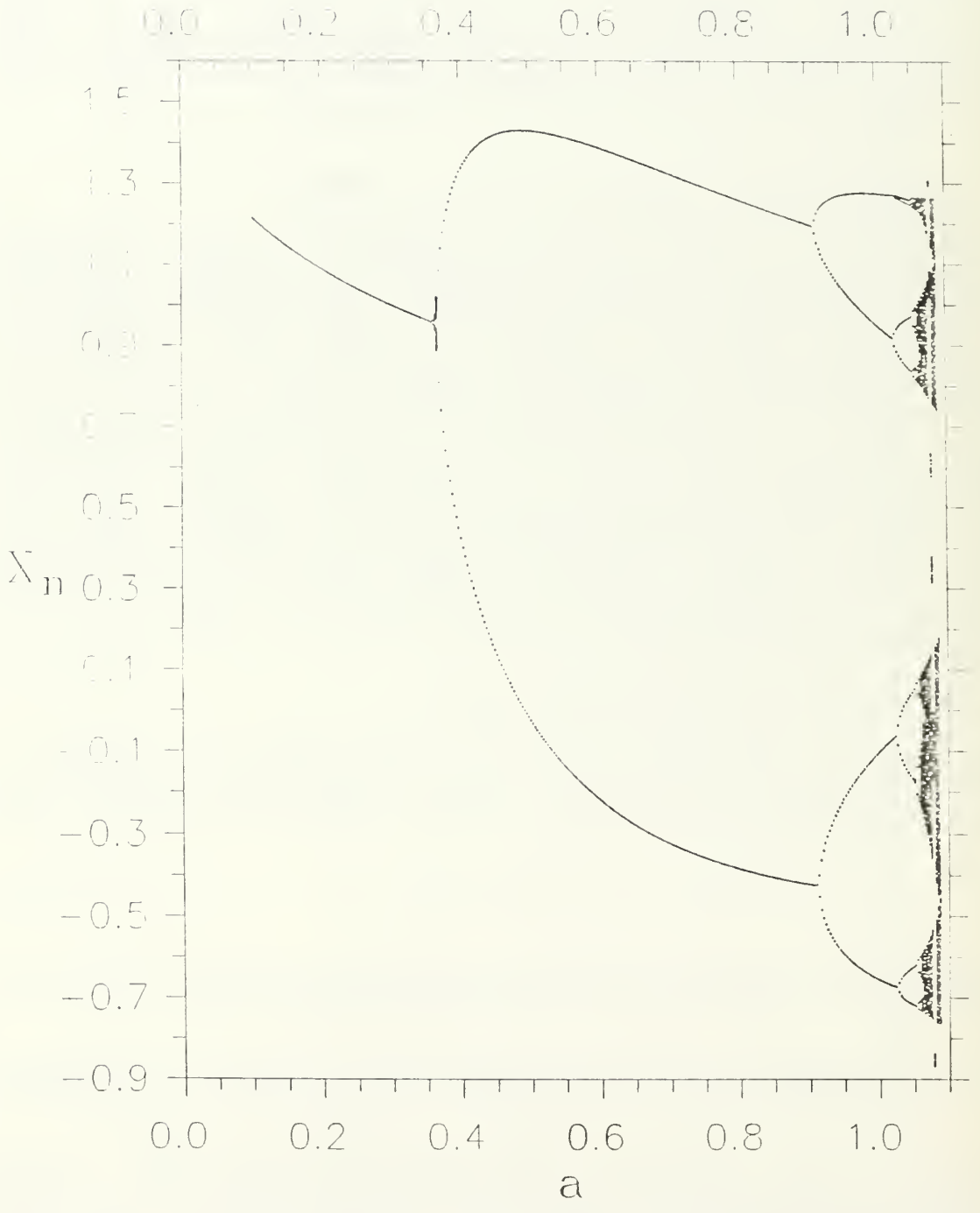

Figure 9. Henon System: Bifurcation Diagram, $x_{n+1} = 1-ax_n^2+y_n$, $y_{n+1} = 0.3x_n$

$$\sigma'_{u_i} = \sigma_{u_i}\sqrt{1 - R^2_{u_i}(\Delta t)} \quad , \tag{II-32}$$

and vertical components,

$$\sigma_w = \begin{cases} \dfrac{K_m}{A\lambda_{m_w}}, & \dfrac{z}{L} \le 0 \quad , \\ 1.21\left(\dfrac{Ri_c - Ri}{Ri_c}\right)^{0.58}\sqrt{\left(\dfrac{\partial \bar{u}}{\partial z}\right)^2 + \left(\dfrac{\partial \bar{v}}{\partial z}\right)^2}, & \dfrac{z}{L} > 0 \quad ; \end{cases} \tag{II-33}$$

here

$$\sqrt{\left(\frac{\partial \bar{u}}{\partial z}\right)^2 + \left(\frac{\partial \bar{v}}{\partial z}\right)^2} = \frac{2.5u_*}{z}\left(1 + 4.7\frac{z}{L}\right)^{\frac{n}{2}}\left(1 - \frac{z}{z_i}\right)^{\frac{n}{2}} \quad , \tag{II-34}$$

and

$$l = \begin{cases} 0.35z, & z < 205m \quad , \\ 70m, & z \ge 205m \quad . \end{cases} \tag{II-35}$$

K_m is the local exchange coefficient, described later in the LPM model discussion, A is a proportionality factor, and z_i denotes the top of the planetary boundary layer. The maximum wavelength in the vertical velocity spectrum is given by

$$\lambda_{m_w} = \begin{cases} \dfrac{z}{\left(0.55 + 0.38\dfrac{z}{L}\right)} \quad , & 0 \le z \le |L| \quad , \\ 5.9z \quad , & L < z \le 0.1z_i \quad , \\ 1.8z_i\left[1 - \exp\left(\dfrac{-4z}{z_i}\right) - 0.0003\exp\left(\dfrac{8z}{z_i}\right)\right] \quad , & 0.1z_i < z < z_i \quad , \end{cases} \tag{II-36a}$$

for z/L < 0, and

$$\lambda_{m_*} = \frac{z}{\left(0.55 + 0.8\frac{z}{L}\right)}, \quad for \quad \frac{z}{L} \geq 0 \quad . \tag{II-36b}$$

Ri was given in eqn. II-19; the critical Richardson number, Ri_C, is

$$Ri_C = 0.115\ \Delta z^{0.175} \quad , \tag{II-37}$$

where Δz is measured in centimeters. The horizontal components are

$$\sigma_u = \sigma_v = \begin{cases} u_*\left(12 + \frac{z_i}{2|L|}\right)^{\frac{1}{3}} , & \frac{z}{L} \leq 0 \quad , \\ 2.3\,u_* , & \frac{z}{L} > 0 \quad . \end{cases} \tag{II-38}$$

The Lagrangian velocity autocorrelations are determined by

$$R_{u_i}(\Delta t) = \exp\left(\frac{-\Delta t}{T_{L_{u_i}}}\right) \quad . \tag{II-39}$$

T_L, the integral or e-folding time for velocity autocorrelations, is determined from the turbulence spectra with

$$T_{L_{u_i}} = 0.2\,\beta_{u_i}\lambda_{m_{u_i}}/\overline{V} \quad , \tag{II-40}$$

where λ_{mu_i} is the dominant wavelength for each component. The average velocity is defined by

$$\overline{V} = \sqrt{\overline{u_i^2}} \quad . \tag{II-41}$$

β, the ratio of Lagrangian to Eulerian time scales, is given by

$$\beta_{u_i} = 0.6\,\frac{\overline{V}}{\sigma_{u_i}} \quad . \tag{II-42}$$

where β is restricted to $\beta \leq 10$. So T_L is in fact proportional to the dominant wavelength divided by the velocity standard deviation.

The horizontal components for peak wavelength are given by

$$\lambda_{z_u} = \lambda_{z_v} = \begin{cases} 1.5 z_i , & \frac{z}{L} \le 0 , \\ 0.7 z_i \sqrt{\frac{z}{z_i}} , & \frac{z}{L} > 0 . \end{cases} \qquad \text{(II-43)}$$

The proportionality constant, A, varies as a function of stability in the unstable boundary layer, and is computed from

$$A = \begin{cases} 0.31 \left(1 - 3\frac{z}{L}\right)^{-\frac{1}{3}} \left(1 - 15\frac{z}{L}\right)^{0.25} \left(0.55 + 0.38\frac{z}{L}\right) , & \left|\frac{z}{L}\right| \le 1 , \\ 0.05 \left(1 - 3\frac{z}{L}\right)^{-\frac{1}{3}} \left(1 - 15\frac{z}{L}\right)^{0.25} , & 0.1 \left|\frac{z_i}{L}\right| > \left|\frac{z}{L}\right| > 1 . \end{cases}$$

(II-44)

Values of $u'(t-\Delta t)$ and $v'(t-\Delta t)$ are determined randomly from a normal probability distribution with zero mean.

A small drift velocity correction (Legg and Raupach, 1982),

$$w_c = T_{L,w} \frac{\partial \sigma_w^2}{\partial z} \left[1 - \exp\left(-\frac{\Delta t}{T_{L,w}}\right)\right] , \qquad \text{(II-45)}$$

was also added to the model to thwart an unrealistic particle drift toward regions of lower tke over long time scales. The real turbulence distribution of vertical velocity is skewed [fig. 10]. So, in the original formulation (McNider, 1981), the normal distribution was modified by altering w according to

$$w(t - \delta t) = \begin{cases} \alpha \omega^+ + \frac{\omega^-}{\alpha} - \eta , & \frac{z}{L} \le 0 , \\ \frac{\omega^+}{\alpha} + \alpha \omega^- + \eta , & \frac{z}{L} > 0 , \end{cases} \qquad \text{(II-46)}$$

where

$$\alpha = -0.028 + 0.6 |P| ,$$
$$\eta = 0.54 |P| , \qquad \text{(II-47a)}$$

and

$$P = \begin{cases} 0.1 + \dfrac{0.6}{0.68\left(1 - 15\dfrac{z}{L}\right)^{-0.25} - 1.8\dfrac{z}{L}}, & \dfrac{z}{L} \le 0 \\ 0.1 - 0.2\left(\dfrac{z}{L}\right)^{0.2}, & \dfrac{z}{L} > 0 \end{cases} . \qquad \text{(II-47b)}$$

The variables ω^+ and ω^- were random values obtained from a normal probability distribution with zero mean and standard deviation, σ_w. Pielke (1984), noted that this method depended on the particular random number generator. Our own tests showed unrealistically large turbulence velocities for convective conditions. The skewness routine is apparently absent from more recent versions of McNider and so has not been employed in this study.

2. The LPM Diffusion Model

As stated, L, the Obukhov length, was proscribed for this study, while V, the mean windspeed at two meters height was set to 3ms^{-1} and the surface vegetative canopy roughness length was set to be 0.05m. Other flow parameters needed by the atmospheric diffusion models were obtained from boundary layer formulae, given here and by Panofsky and Dutton (1984), Sorbjan (1990) and Kamada (1992a,c). Many algorithms listed here are in the windflow simulation already used to drive the McNider model. From the windflow profile the McNider model uses: turbulent diffusivity, K_m, gradient Richardson number, Ri, vertical windshear, windspeed at height z, v_z, and u_*.

u_* is computed from L, using ψ_m from eqn. II-24, and the square root of the surface drag coefficient,

$$C_{dn}^{1/2} = \frac{k}{\ln\left(\dfrac{z}{z_0}\right) - \psi_m} , \qquad \text{(II-48)}$$

so that

$$u_* = MAX\left(C_{dn}^{1/2}, 0.01\right) . \qquad \text{(II-49)}$$

Given L and u_* and using eqn. II-22, one can compute the surface vertical temperature flux,

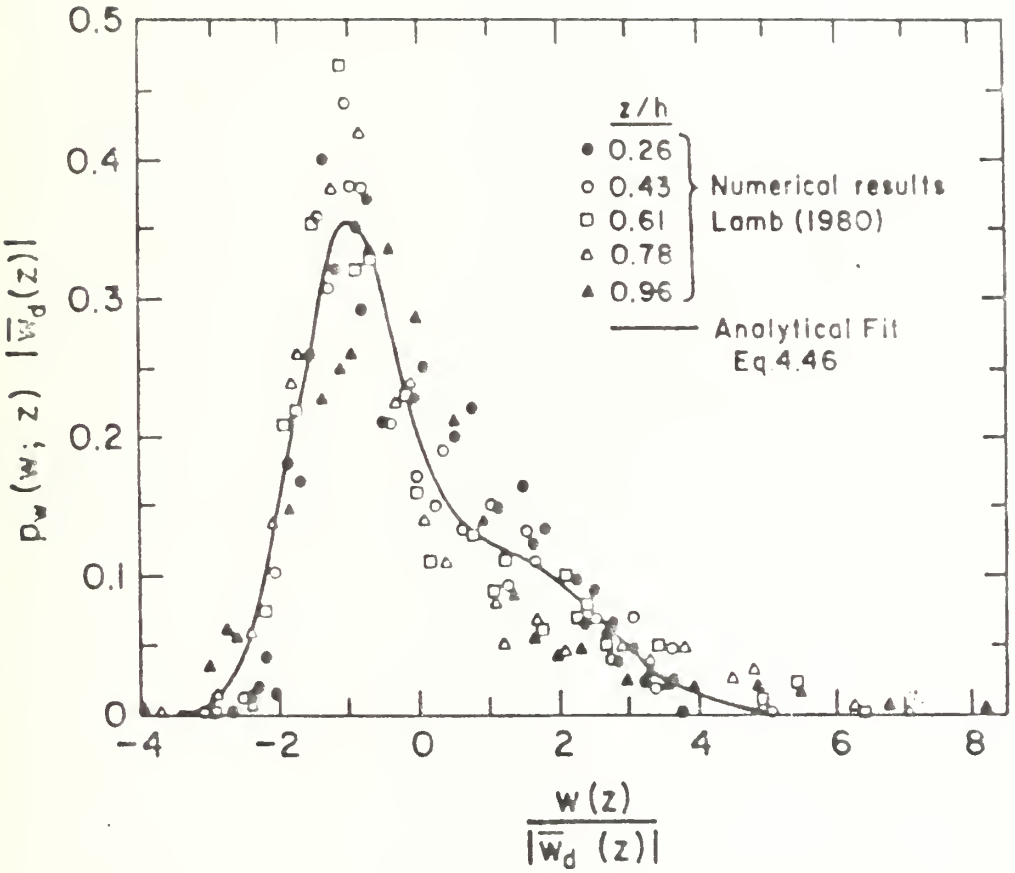

Figure 10. Probability density function of vertical velocity in the convective boundary layer. From Weil, Dispersion in the Convective Boundary Layer, Lectures on Air Pollution Modelling, Venkatram and Wyngaard, 1988.

$$\overline{w'\theta_v'} = -\frac{u_*^3\theta}{kgL} \quad . \tag{II-50}$$

This allows an estimate of the free convective boundary layer turbulent velocity scale (for L < 0),

$$w_* \equiv \left(gz_i\frac{\overline{w'\theta_0'}}{\theta}\right)^{1/3} \quad . \tag{II-51}$$

This can be modified to include shear induced surface layer turbulence (forced convection) (Kamada, 1992a,c) as

$$w_{*s} = \left\{\frac{1.0 - \frac{L}{z_i}\left[\frac{5}{4} - 0.65\left(\frac{L}{z_i}\right)\ln\left|\left(1 - 150\frac{z_0}{L^{1/3}}\right) - 1\right|\right]}{0.65\left(\frac{L}{z_i}\right)}\right\} w_* \quad . \tag{II-52}$$

For z/L < -0.5, i.e., above the surface layer, the following forms were used. The vertical velocity variance was given by

$$\sigma_w^2 = w_{*s}^2\left[1.1\left(\frac{z}{z_i}\right)^{2/3}\left(1 - \frac{z}{z_i}\right)^{2/3} + R^{2/3}\left(\frac{z}{z_i}\right)^{2/3}\left(1 - \frac{z}{z_i} + D\right)^{1/3}\right] \quad , \tag{II-53}$$

where R ≃ 0.2 and D ≃ 0.1 are ratios of the inversion/surface temperature flux and entrainment zone/boundary layer depth (Sorbjan, 1990).

In a standard atmospheric windflow model with second order turbulence closure scheme, the tke is computed prognostically. If σ_w^2 is supplied as above, the horizontal variances follow by subtraction. Without such a model, we show here that σ_u^2 and σ_v^2 can be obtained diagnostically as follows.

The Andre (1978) third order turbulence closure used the following prognostic form for vertical velocity variance,

$$\partial\frac{\overline{w^2}}{\partial t} = -\partial\frac{\overline{w^3}}{\partial z} + 2\beta\overline{w'\theta'} - C_4\epsilon\left(\frac{\sigma_w^2}{\bar{e}} - \frac{2}{3}\right) - \frac{2}{3}\epsilon \quad . \tag{II-54}$$

Assuming steady state and neglecting diffusion, this can be truncated to estimate the anisotropy, $\sigma_w^2/\bar{e}$, where $\bar{e}$ is tke. Mason and Thompson's (1987) large eddy simulation of neutrally stable flow showed that $\sigma_w^2/\bar{e} \simeq 1/3$ near the surface and increased with height. This occurs because the surface restricts vertical motion. Also, most boundary layer turbulence results from "surface no-slip" induced shear which creates mostly horizontal tke. The increase with height occurs because the shear drops rapidly, so $\sigma_w^2/\bar{e}$ gradually approaches the isotropic 2/3 value through pressure redistribution.

ϵ, the molecular dissipation rate of tke, decays roughly linearly with height. For convective boundary layers, Sorbjan (1990) parameterized ϵ as,

$$\phi\epsilon = \frac{3(1 - z/z_i)}{4} + Rz/z_i \quad , \text{ and} \tag{II-55}$$

$$\epsilon = \phi\epsilon w_*^3/z_i \quad . \tag{II-56}$$

This means that the tke anisotropy ratio can be parameterized as

$$\frac{\sigma_w^2}{\bar{e}} = \frac{2\epsilon_0 - \epsilon}{3\epsilon_0} + \frac{\beta\overline{w'\theta'_z}}{\epsilon} \tag{II-57}$$

(Kamada and Drake, 1992). The first term on the right hand side accounts for height dependence under neutral stability, while buoyancy flux in the second term accounts for non-neutral stability. This form actually corresponds to the Lenschow et al. (1980) measurements better than the Andre model itself or derivatives thereof (Therry and Lacarrere, 1980).

So the horizontal turbulent velocity variances become

$$\sigma_u^2 = (5/9)\sigma_w^2(2\bar{e}/\sigma_w^2 - 1) \quad , \text{ and} \tag{II-58a}$$

$$\sigma_v^2 = 0.8\sigma_u^2 \quad . \tag{II-58b}$$

This allows one to compute tke as,

$$\bar{e} = (\sigma_u^2 + \sigma_v^2 + \sigma_w^2)/2 \quad . \tag{II-59}$$

The molecular the dissipation length scale is parameterized as

$$l_\epsilon = 1/(1/z + 1.4\epsilon\bar{e}^{1/2}) \quad , \tag{II-60}$$

from which the turbulent mixing length is estimated as,

$$l_k = MIN(3l_\epsilon \sigma_w^2/\bar{e},\ z) \quad . \tag{II-61}$$

This finally yields the required turbulent diffusivity,

$$K_m = 0.44 l_k \bar{e}^{1/2} \quad , \tag{II-62}$$

(Kamada and Drake, 1992). To obtain θ and buoyancy, the buoyancy gradient for the unstable boundary layer is given by

$$\beta\partial\theta/\partial z = 0.6\theta_*/z_i((1-z/z_i)^{2/3}/(z/z_i)^{1/3} - 2R^{2/3}(z/z_i)^{2/3}/(1 - z/z_i + D)^{2/3}) \quad , \tag{II-63}$$

where $\theta_* = \overline{w'\theta'}_0/u_*$ (II-64)

(Sorbjan, 1990). The above formulations were applied to the convective (unstable) boundary layer ($z/L < -0.5$) above the surface layer.

For the unstable surface layer ($L < 0$, but $z/L > -0.5$),

$$\phi_m = (1 - 28z/L)^{-1/4} \quad , \tag{II-65}$$

$$K_m = ku_*z/\phi_m \quad , \tag{II-66}$$

$$\bar{e} = (5.6K_m/z_i)^2 \quad , \tag{II-67}$$

$$Ri = z/L \quad , \tag{II-68}$$

$$\phi_1 = (12 - 0.5z_i/L)^{1/3} \quad , \tag{II-69}$$

$$\phi_2 = \phi_1 \quad , \tag{II-70}$$

$$\phi_3 = (1 - 14z/L)^{1/4} \quad , \tag{II-71}$$

$$\phi_\epsilon = (1 + .75*(-z/L)^{2/3})^{3/2} \quad , \tag{II-72}$$

and finally

$$\epsilon_0 = u_*^3 \phi_\epsilon / z_i \quad , \tag{II-73}$$

where the subscript 0 refers to the surface value (Sorbjan, 1990).

For neutral to stable boundary and surface layers, where $L \geq 0$, we assume from Sorbjan (1990) that

$$\alpha \simeq 2 - 10/L \quad , \text{ and} \tag{II-74}$$

$$\beta \simeq 3 - 20/L \quad , \tag{II-75}$$

So that,

$$\phi_1 = 2.5(1 - 0.8\ z/z_i)^{\alpha/2} \quad , \tag{II-76}$$

$$\phi_2 = 1.9(1 - 0.8\ z/z_i)^{\alpha/2} \quad , \text{ and} \tag{II-77}$$

$$\phi_3 = 1.6(1 - 0.8\ z/z_i)^{\alpha/3} \quad . \tag{II-78}$$

The local friction velocity and Obukhov lengths were characterized in Sorbjan (1990) as

$$u_l = u_*(1 - z/z_i)^{\alpha/2} \quad , \text{ and} \tag{II-79}$$

$$L_l = L(1 - z/z_i)^{3\alpha/2-\beta} \quad . \tag{II-80}$$

and the temperature flux at height, z, was given by

$$\overline{w'\theta'}_z = \overline{w'\theta'}_0(1 - z/z_i)^{\beta} \quad . \tag{II-81}$$

The Brunt-Vaisala frequency at height, z, was given by

$$BVF = 4.3u_*\theta_*^2(1 + 3.7z/L)(1 - z/z_i)^{\beta+\alpha}/z \quad . \qquad \text{(II-82)}$$

The tke dissipation rate at z was parameterized as

$$\phi_\epsilon = 3.6(1 + 3.7z/L)(1 - z/z_i)^{\beta}/z \quad , \text{ and} \qquad \text{(II-83)}$$

$$\epsilon = \phi_\epsilon u_*^3 \quad . \qquad \text{(II-84)}$$

The Richardson number was estimated as

$$Ri = \frac{z}{5z + L} \quad , \qquad \text{(II-85)}$$

and the momentum diffusivity was given roughly by

$$K_m = \frac{ku_*z(1 - z/z_i)}{1 + 5\ z/L} \qquad \text{(II-86)}$$

(Sorbjan, 1990). Both the unstable surface layer and neutral to stable boundary layer cases used:

$$\sigma_u = u_*\phi_1 \quad , \qquad \text{(II-87a)}$$

$$\sigma_v = u_*\phi_2 \quad , \qquad \text{(II-87b)}$$

$$\sigma_w = u_*\phi_3 \quad , \qquad \text{(II-87c)}$$

$$\psi_h = 2ln[\ (1 + (1 - 14z/L)^{1/2})/2\ ] \quad , \text{ and} \qquad \text{(II-88)}$$

$$\theta_z = \theta + \theta_*(\ ln(z/z_0) - \psi_h\ )/k \quad . \qquad \text{(II-89)}$$

The mean wind at height z and its shear were estimated to be

$$V_z = u_*(\ ln(z/z_0) - \psi_m\ )/k \quad , \text{ and} \qquad \text{(II-90)}$$

$$\partial V_z/\partial z = u_*(1 + 4.7z/L)^{a2}(1 - z/z_i)^{a2}/kz \qquad \text{(II-91)}$$

(Panofsky and Dutton, 1984 and Sorbjan, 1989).

The following details only the significant items distinguishing the LPM and McNider models. The LPM particle model utilized the above formulations for the velocity variances and tke rather than those from McNider. For the LPM particle model, the Lagrangian vertical timescale was also estimated differently according to

$$T_{lw} = \lambda_{mw}/\sigma_w \qquad (L > 0) \quad \text{, and} \qquad \text{(II-92)}$$

$$T_{lw} = 0.3z_i/w_* \qquad (L < 0) \quad . \qquad \text{(II-93)}$$

Noting that the horizontal/vertical eddy aspect ratio decreases with increasing stability in the convective boundary layer, the horizontal Lagrangian integral timescales were estimated by

$$T_{lu} = (2 - 40/L)\, T_{lw} \quad \text{, and} \qquad \text{(II-94)}$$

$$T_{lv} = T_{lu} \quad . \qquad \text{(II-95)}$$

The McNider algorithms for horizontal integral timescales were retained for stable cases.

Non-stochastic buoyant forcing was also added to the LPM particle model for non-zero density gradients. For pure buoyancy driven motion, the force balance is just

$$\frac{\partial w}{\partial t} = -g\frac{\delta\theta}{\theta} \quad , \qquad \text{(II-96)}$$

where w is vertical velocity. In a domain where $\partial\theta/\partial z \neq 0$, $\delta\theta$ is the potential temperature change due to a displacement, δz, from the particle's neutral buoyancy height. The initial release height of the particle is taken to be the neutral buoyancy height. Then,

$$\partial w = - \frac{g}{\theta} \delta\theta \, \partial t \quad . \tag{II-97}$$

If the particle's "memory" were perfect, then after a time, t, its buoyancy forced velocity would simply be

$$w = - \frac{g}{\theta} \int_0^t \delta\theta \, \partial t \quad . \tag{II-98}$$

However, to simulate dilution by ambient fluid, the particle must gradually forget its neutral buoyancy level. Its mnemonic e-folding time will be T_{lw}, the integral eddy coherence time scale already used to compute the stochastic component. So at each time step the particle's memory dims by the factor,

$$M = e^{\frac{-\delta t}{T_{lw}}} \quad . \tag{II-99}$$

In this case, after one time step,

$$w_1 = -(g/\theta)\delta\theta_1 \delta t \quad , \tag{II-100}$$

as before. But for subsequent time steps, the solutions are

$$w_2 = -(g/\theta)\delta t(M\delta\theta_1 + \delta\theta_2) \quad , \tag{II-101}$$

$$w_3 = -(g/\theta)\delta t(M^2\delta\theta_1 + M\delta\theta_2 + \delta\theta_3) \quad , \tag{II-102}$$

or in general,

$$w_m = -(g/\theta)\delta t \sum_1^m \delta\theta_i \, M^{m+1-i} \quad . \tag{II-103}$$

This series grows quickly with m. However, we also observe that

$$w_{i+1} = Mw_i - (g/\theta)\delta\theta_{i+1}\delta t \quad , \tag{II-104}$$

3. Random Number Generator Kernel

The diffusion models utilize normally distributed random numbers to generate the fluctuating velocity. These fluctuations are scaled by the standard deviation of the velocity components to relate them to the turbulent kinetic energy of the flow field. As noted by Pielke (1984), these depend on the random number generator.

We tested several random number generation and normal distribution algorithms. The method used to generate random numbers in this study was a variation of the congruence method. The normal distribution algorithm was a variation of the inverse method, and is listed in subroutine NORNG. To check the distribution of the random number generation routine, the count distribution was plotted versus standard deviation [fig. 11], and the bias computed. Although it appears to have a generally Gaussian shape with perhaps slight skewness to the left of center for the 3600 iterations used in this test, the corputed bias was only -1.8×10^{-4}. We tried several other random number and normal distribution algorithms, with the following results:

Random Number Generator Analysis

METHOD	TIME (3700 iterations)	BIAS
linear congruential(2) w/direct method(5)	~ 25 sec	+2.8 E-02
linear congruential(2) w/inverse method(4)	~ 28 sec	-1.8 E-04
old random generator(2) w/direct method(5)	~ 26 sec	+5.3 E-03
old random generator(1) w/inverse method(4)	~ 26 sec	+3.4 E-02
old random generator(1) w/old inverse method(3)	~ 25 sec	+4.7 E-03

Method 1. Peerless Engineering Service, 1989: FORTRAN Scientific Subroutine Library Version 2.0, John Wiley & Sons, New York, pp. 276-277.

Method 2. McCracken, D., and W. Salmon, 1988: Computing for Engineers and Scientists with FORTRAN 77, John Wiley & Sons, New York, pp. 562-566.

Method 3. Peerless Engineering Service, 1989: FORTRAN Scientific Subroutine Library Version 2.0, John Wiley & Sons, New York, pp. 278-279.

Method 4. Abramowitz, A., and I. Stegun, ed., 1972: Handbook of Mathematical Functions with Formulas, Graphs, and Mathematical Tables, National Bureau of Standards, Applied Math Series, **55**, Ninth Printing, pp. 952-953.

Method 5. Abramowitz, A., and I. Stegun, ed., 1972: Handbook of Mathematical Functions with Formulas, Graphs, and Mathematical Tables, National Bureau of Standards, Applied Math Series, **55**, Ninth Printing, pg. 953.

Times determined using an IBM PC with Intel 386 CPU and Intel 387 math coprocessor running PROFORT.

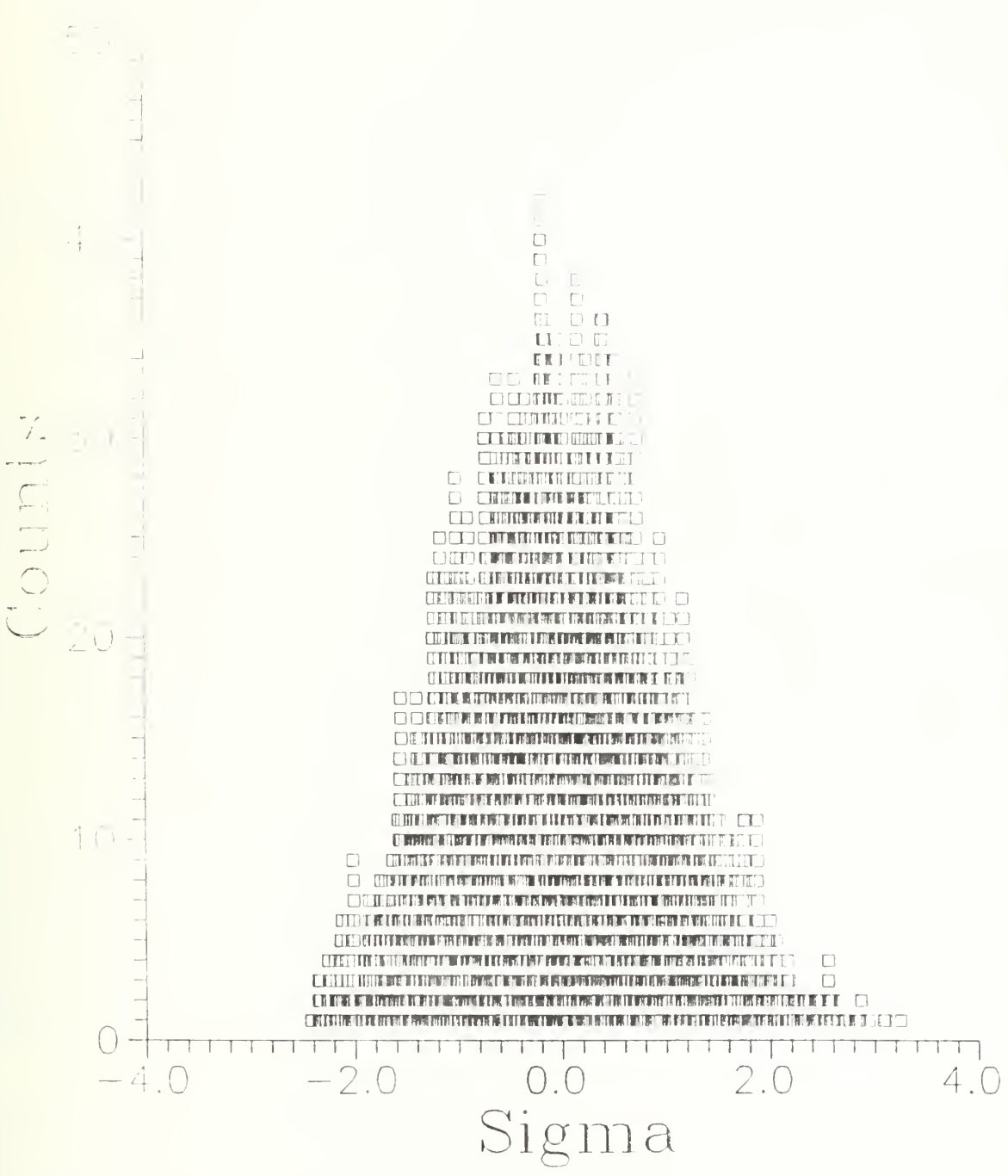

Figure 11. Random Number Generator, Distribution of 3600 Total Counts in units of Standard deviation, Congruence Method

III. ANALYSIS

All models were written in ANSI FORTRAN-77, and run on Intel 386-based PCs using the IBM PROFORT compiler. All graphs were produced with Golden Software's Grapher and Surfer programs.

F. LOGISTICS DIFFERENCE AND HENON EQUATIONS

1. Analyzing the Logistics Difference Equation

Since generation of the logistics difference attractor involves recursive iteration of a function rather than successive displacements in time, an iterative rather than time series results. So the fractal lengths must be redefined using

$$L(i) = \frac{i}{\epsilon} \int_0^T |F(i-\epsilon) - F(i)| \, di \quad . \tag{III-1}$$

This is approximated numerically by

$$L(i) = \sum_{i=K,k}^{N} |F(i+k) - F(i)|, \tag{III-2}$$

where

$F(i) \equiv$ *value of the function at the ith iterate,*

$i \equiv$ *iteration step,*

and $k \equiv$ *resolution in terms of number of iterations.*

Like the Lagrangian particle models studied below, the resulting iterative series describes a single particle which shifts position, so that each successive iteration is in many ways analogous to a time step. To insure independence from initial values, the first 100 points were discarded from each run of 3700 iterations. So N = 3600 point data sets were obtained for all plots. Since recursion prohibits non-integer iterations, the values of k had to be integer divisors of 3600. This allows 45 different k values with sufficient dynamic range to generate plots.

A standard linear regression routine then determined D_A from a series of k values for L(k) for a given μ (see eqn. II-25, p. 14). The standard deviation of D_A was very small in chaotic situations, but large during period doubling. Reasons are discussed below.

The last three values of L(k) and k were discarded in computing D_A because, as Kamada and DeCaria (1992) showed for sine waves and also noted for time-series data, the curve flattens for K > N/3, since resolved lengths do not change much when the resolution (iteration span) approaches the period. In the particular case of the parabolic logistics difference equation, another reason for rejecting the highest k values is that the particle trajectories are confined to the unit interval by the left-right symmetry or fold at mid-parabola. The distance traversed during a fold crossing is not fully accounted when compared to a system without folds. The change in "apparent" traversed distance will be lessened as more fold crossings are involved and the number of fold-crossings increase with larger k. This results in decidedly non-linear slopes for log L(k) versus log k for k which are a sizeable fraction of the total window span.

For values of μ corresponding to a fixed point, the plot of $Log_{10}L(k)$ vs $Log_{10}(k)$ is fairly flat, and the corresponding D_A value is small [fig. 12]. For values of μ corresponding to period doubling (period 2), the plot shows large jumps from a baseline, corresponding to multiple harmonics of 2 [fig. 13]. The baseline corresponds to a zero length. For these plots, the zero was adjusted by adding one to avoid a baseline at $-\infty$, a result of $Log_{10}(0)$. Without it, $D_A \to \infty$ for all periodic functions.

A period 4 plot still shows regularity [fig. 14]. There appear to be three sets of overlapping slope patterns: one, a baseline of slope zero; the other two with similar slopes but different amplitudes. Again, this can be ascribed to harmonics. The length is zero for every fourth data point, and so will remain zero for harmonics having k values of 4, 8, 16, etc. The length is nonzero for every second data point, not including multiples of four. There is similarity in lengths for k values of 2, 6, 10, 18, etc. Likewise, there is similarity in lengths for k values which are not multiples of 2, e.g., 1, 3, 5, etc.

At the onset of chaos (μ = 3.569946) as in fig. 15, all L(k) lift off the baseline. I.e., without any fixed point attractors and periodicity, lengths cannot remain zero for any k. Thus, D_A must increase while σ_{D_A} decreases. We also observe another chaos characteristic, a sensitivity to initial conditions for identical values of μ. Figure 16, with x_0 = 0.04, differs from fig. 14 with x_0 = 0.1. However, fig. 15, with x_0 = 0.1, is virtually identical to fig. 17, with x_0 = 0.01. There may be an intrinsic pattern to this sensitivity to initial conditions. Perhaps the fold crossing patterns might provide further insight, but this question strays from the present focus.

For full chaos, σ_{D_A} becomes relatively small and the plot becomes almost linear [fig. 18]. This highlights why the last three points

Figure 12. Logistics Difference Equation, $x_{n+1} = 2.8x_n(1-x_n)$, $x_0 = 0.01$, Fixed Point Attractor.

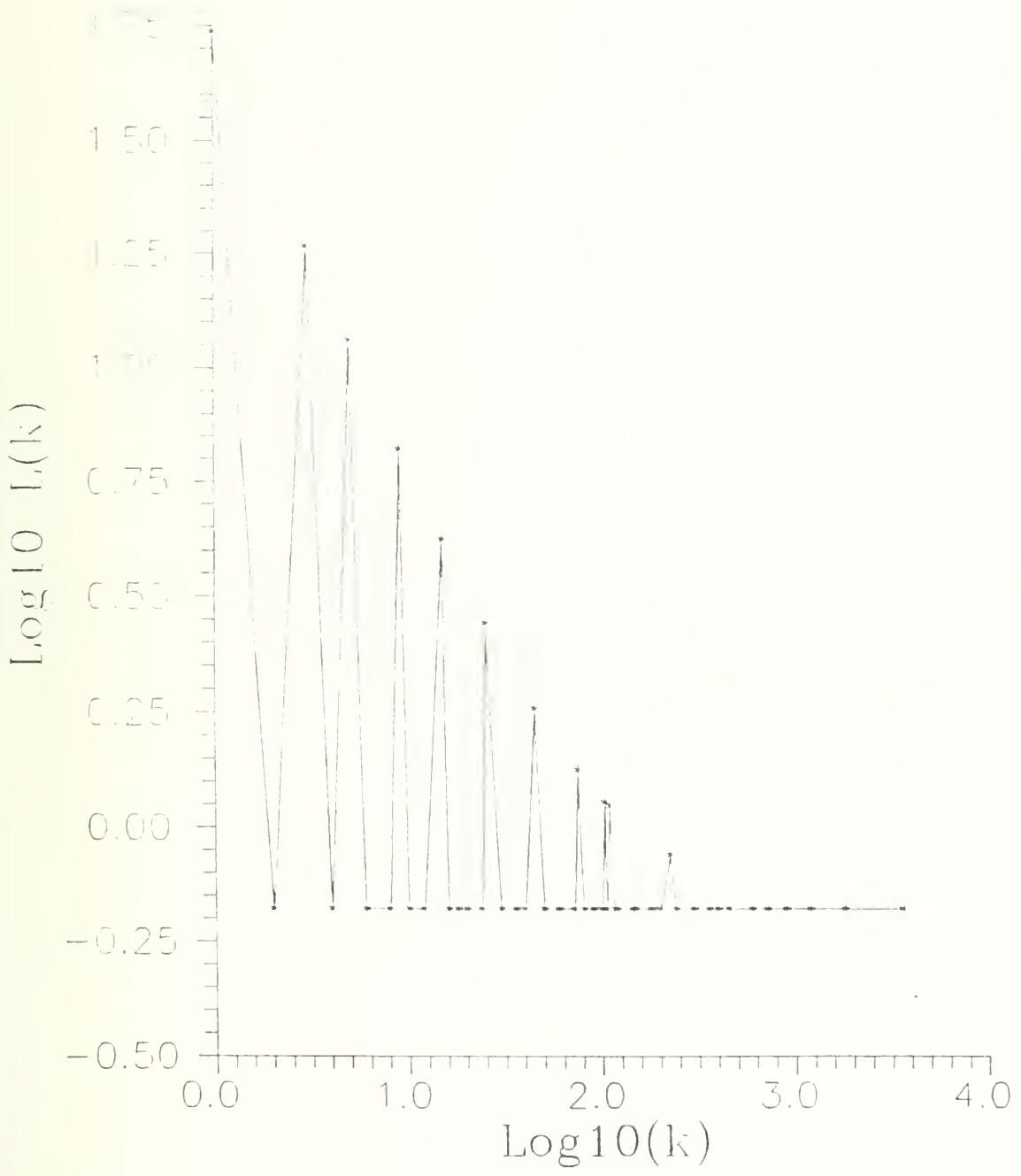

Figure 13. Logistics Difference Equation. $x_{n+1} = 3.0x_n(1-x_n)$, $x_0 = 0.01$, Period 2.

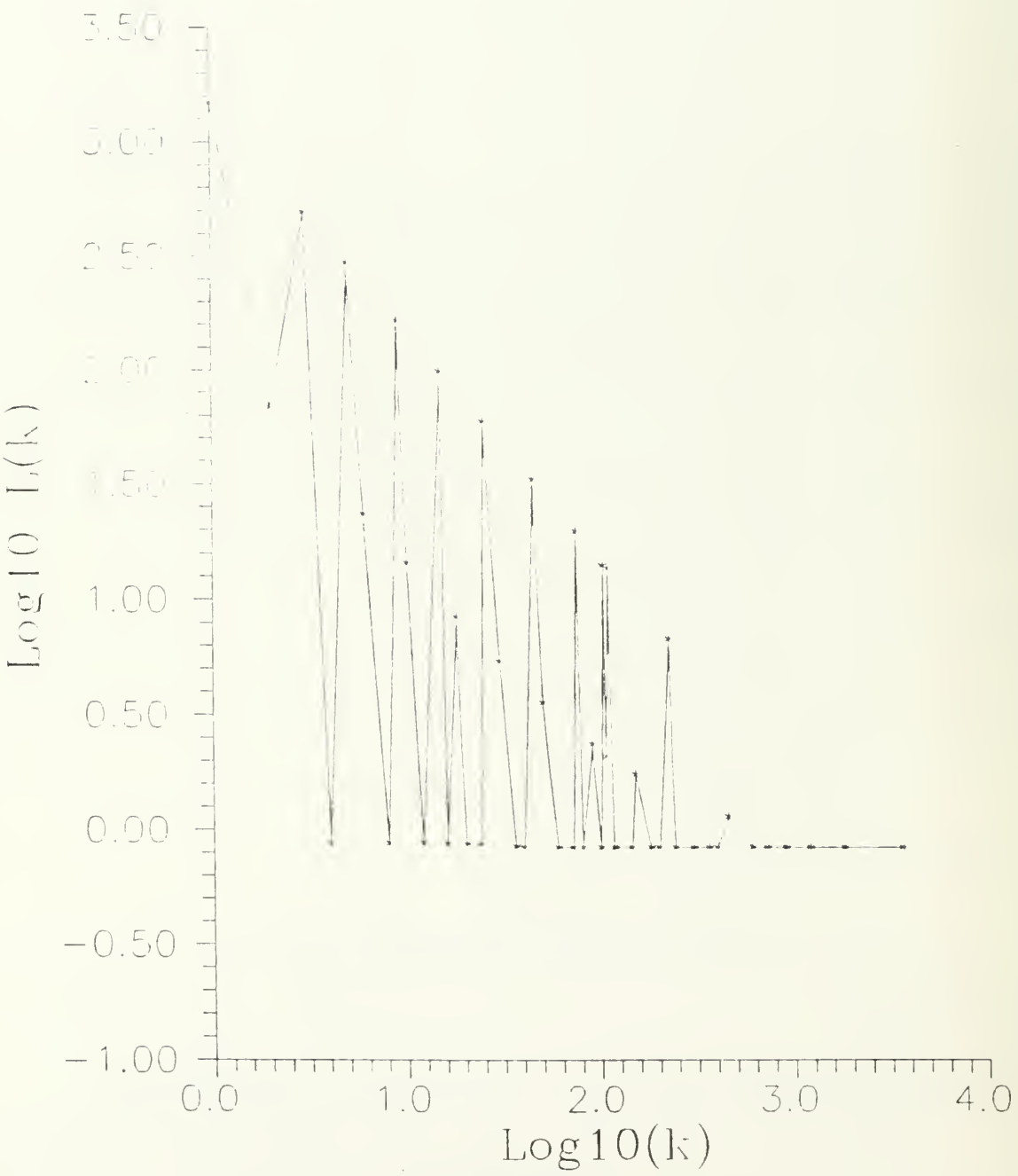

Figure 14. Logistics Difference Equation, $x_{n+1} = 3.48x_n(1-x_n)$, $x_0 = 0.01$, Period 4.

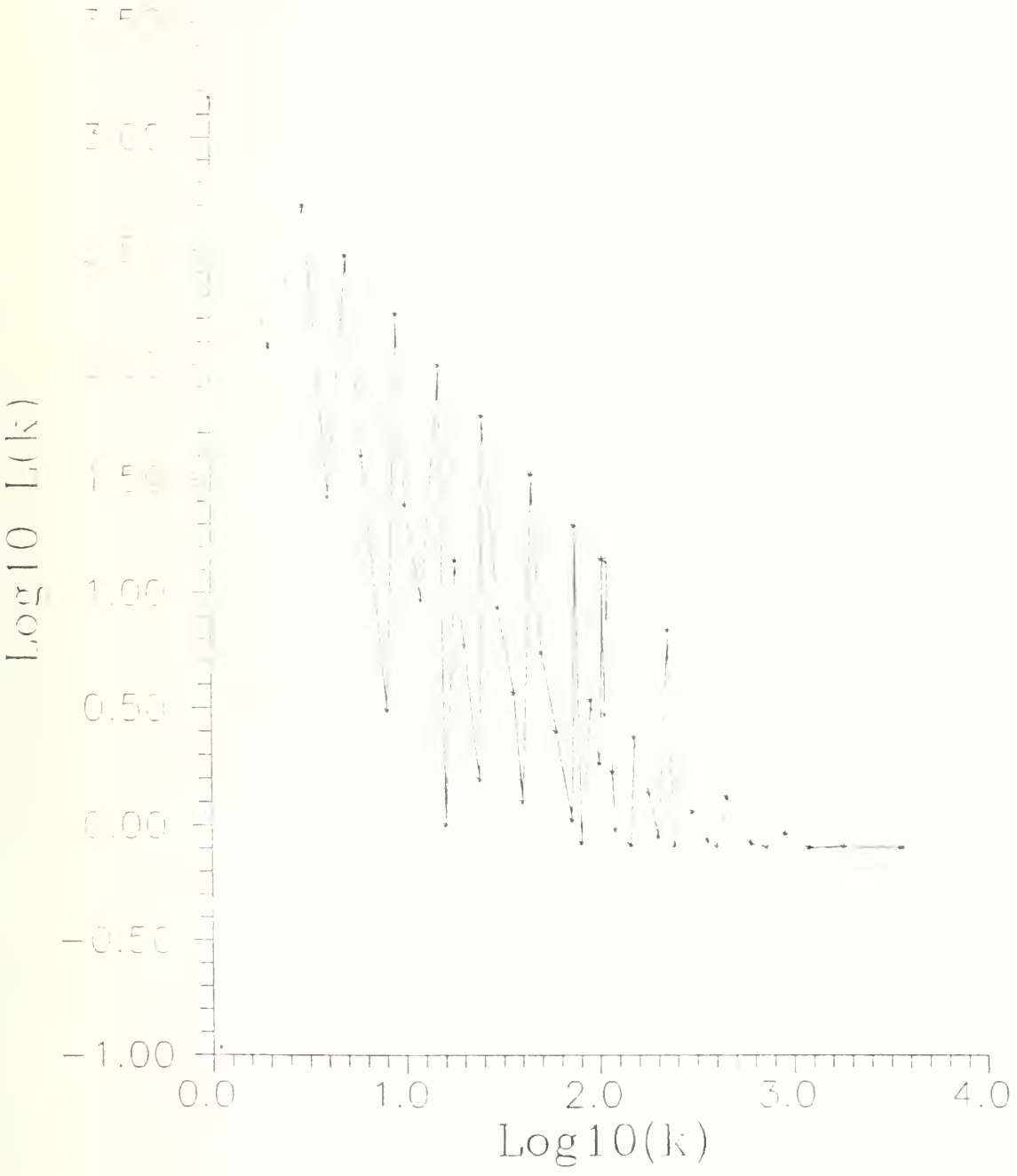

Figure 15. Logistics Difference Equation, $x_{n+1} = 3.56994568x_n(1-x_n)$, $x_0 = 0.1$, Onset of Chaos.

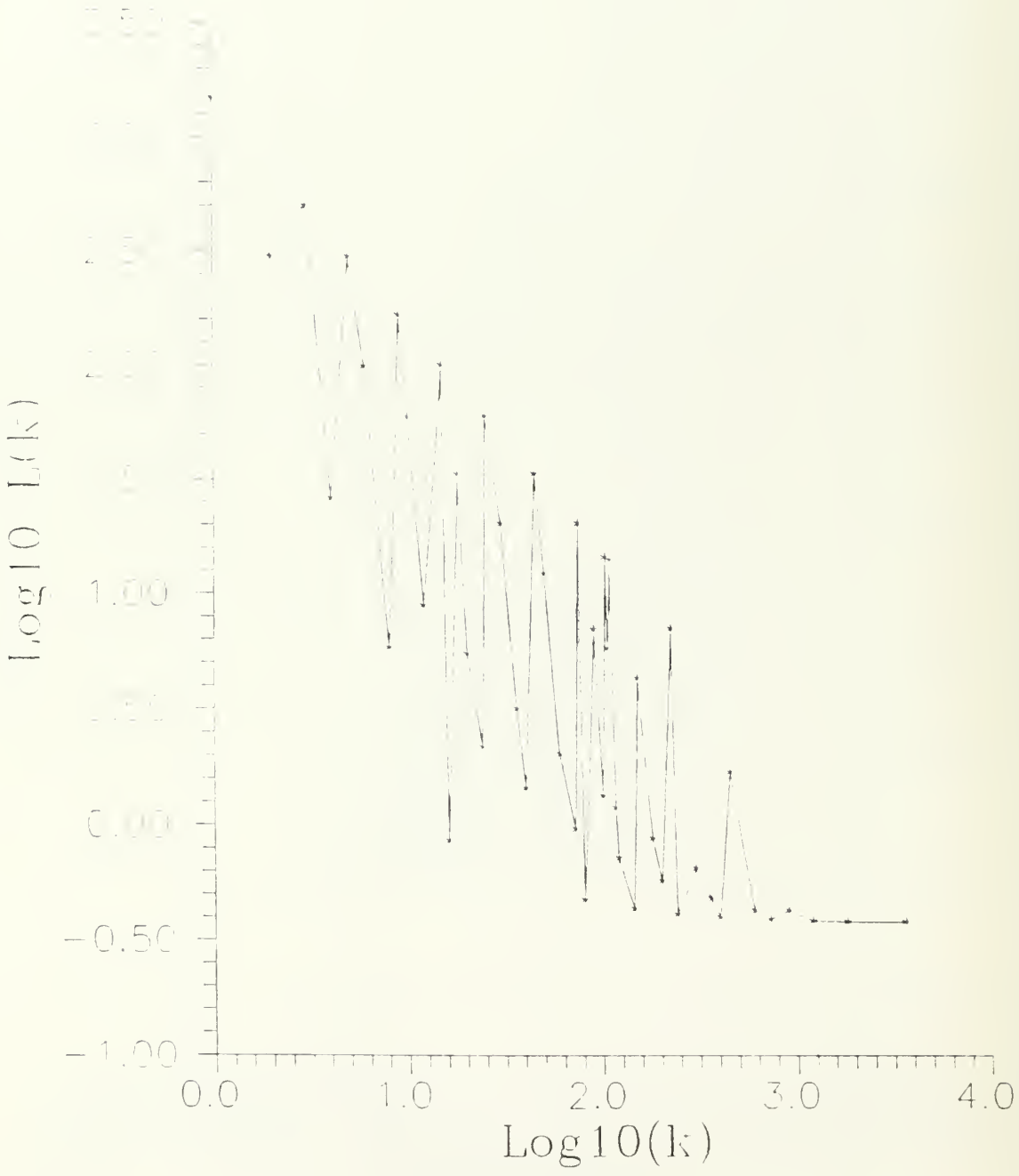

Figure 16. Logistics Difference Equation, $x_{n+1} = 3.56994568x_n(1-x_n)$, $x_0 = 0.04$, Onset of Chaos

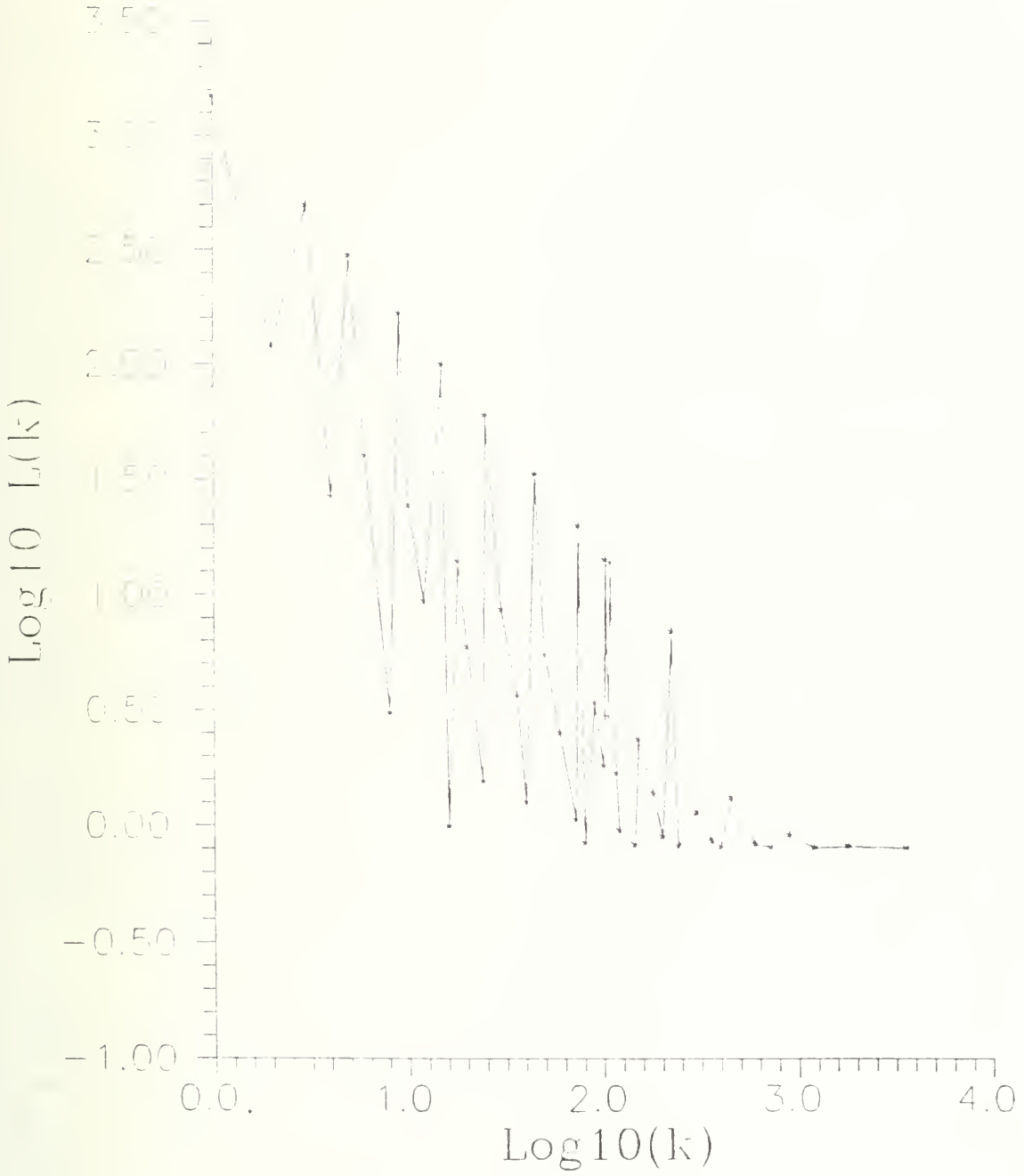

Figure 17. Logistics Difference Equation, $x_{n-1} = 3.56994568x_n(1-x_n)$, $x_0 = 0.01$, Onset of Chaos.

were discarded in computing D_A; the plot remains very linear sans large values of k. The main reason is the fold crossing patterns mentioned earlier. Besides, not enough data points are kept in the length computation for large k values to retain similarity. For k=1200 and N=3600, the computed length is the sum of only three distance measurements, which is not enough to develop a good statistical mean length.

A plot of D_A versus μ shows many of the features noted in the previous bifurcation plot [fig. 19]. At $\mu \approx 3.0$ D_A jumps from zero (corresponding to a fixed point) to ≈ 0.58, corresponding to period 2. At $\mu \approx 3.45$ we see a transition to period 4. Higher μ values display regions of periods 8 and 16. However, at this level of resolution period 32 or higher order bifurcations cannot be discerned. Within the chaos regime, about $\mu \approx 3.6$, D_A seems to oscillate, and shows several sharp peaks and dips. The apparent window at $\mu \approx 3.85$ corresponds to a period 4 oscillation.

A plot of S, the Shannon entropy, versus μ shows similar features [fig. 20]. Regions of period 2, 4, and 8 are apparent. As with D_A differences in S between period 16 and above and chaos cannot be discerned at this level of resolution. The large window of low periodicity at $\mu \approx 3.85$ is also seen, as are several other windows of periodicity at roughly $\mu \approx 3.63$ and $\mu \approx 3.73$.

The Lyapunov exponent also shows the trends seen in the fractal dimension and entropy [fig. 21]. λ dips sharply at $\mu \approx 3.25$, 3.5, and 3.55, the centers for periods 2, 4, and 8. Again, changes beyond period 16 are hard to resolve.

In the period doubling region, $\lambda = 0$ marks the transition to the next bifurcation, a fixed point fissioning to two fixed points. For $\lambda > 0$, the function is chaotic. There are also many "windows of periodicity" within the chaos which appear in the bifurcation, fractal dimension, and entropy plots, but are more readily seen in the Lyapunov exponent; if $\lambda <$ zero, the function is periodic.

Figure 22 shows strong correlations between S, D_A, and λ. Chaos and periodicities are apparent for each metric, as are differences. D_A sometimes peaks where S and λ dip, as at $\mu \approx 3.725$. The low values of λ and S indicate periodic regions, for which D_A sometimes sharply increases. The bifurcation map [fig. 6] provides no immediate cause. But we reason that, **if successive fixed points are more widely spaced than the average distance between successive points in the surrounding chaos, then D_A will be relatively large. This is less likely for real fluid motions constrained by physical forces and conservation laws. But it points to a potential difference between dispersion and diffusion rates even without mean flow, a point we expand on below.**

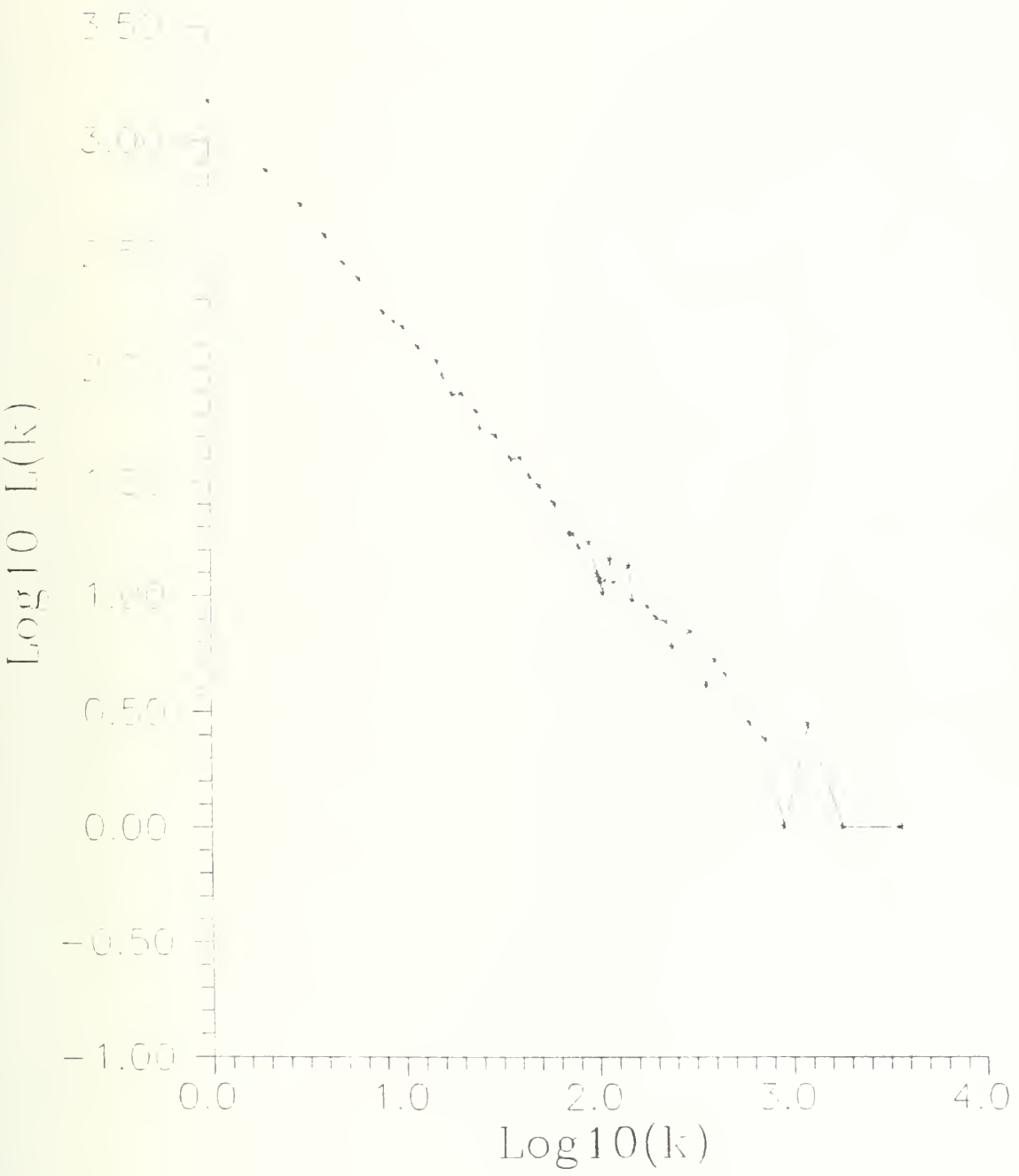

Figure 18. Logistics Difference Equation, $x_{n+1} = 3.9996x_n(1-x_n)$, $x_o = 0.01$, fully chaotic regime

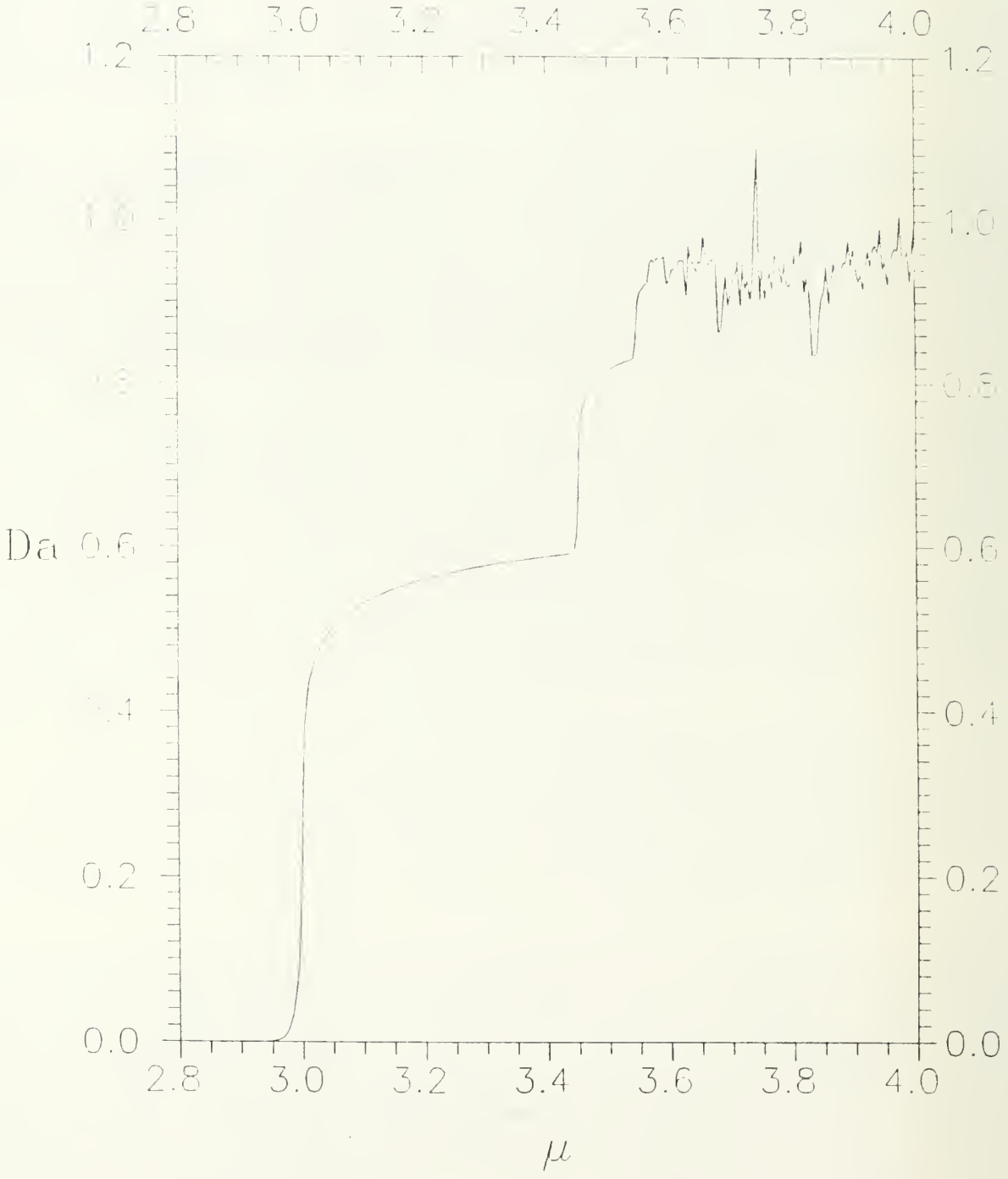

Figure 19. Fractal Dimension Analysis of Logistics Difference Equation, $x_{n+1} = \mu_n(1-x_n)$.

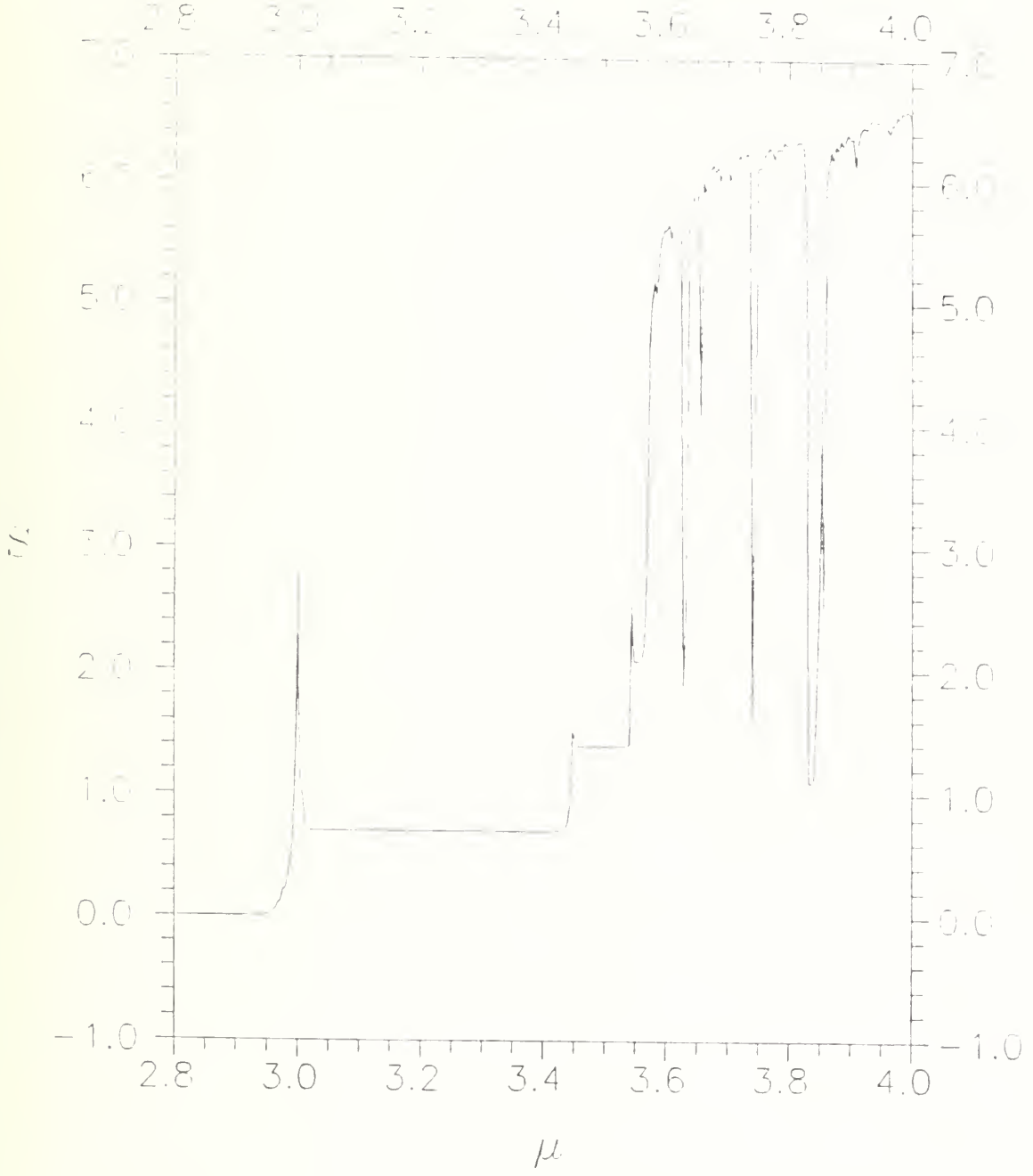

Figure 20. Shannon Entropy Analysis of Logistics Difference Equation, $x_{n+1} = \mu x_n(1-x_n)$.

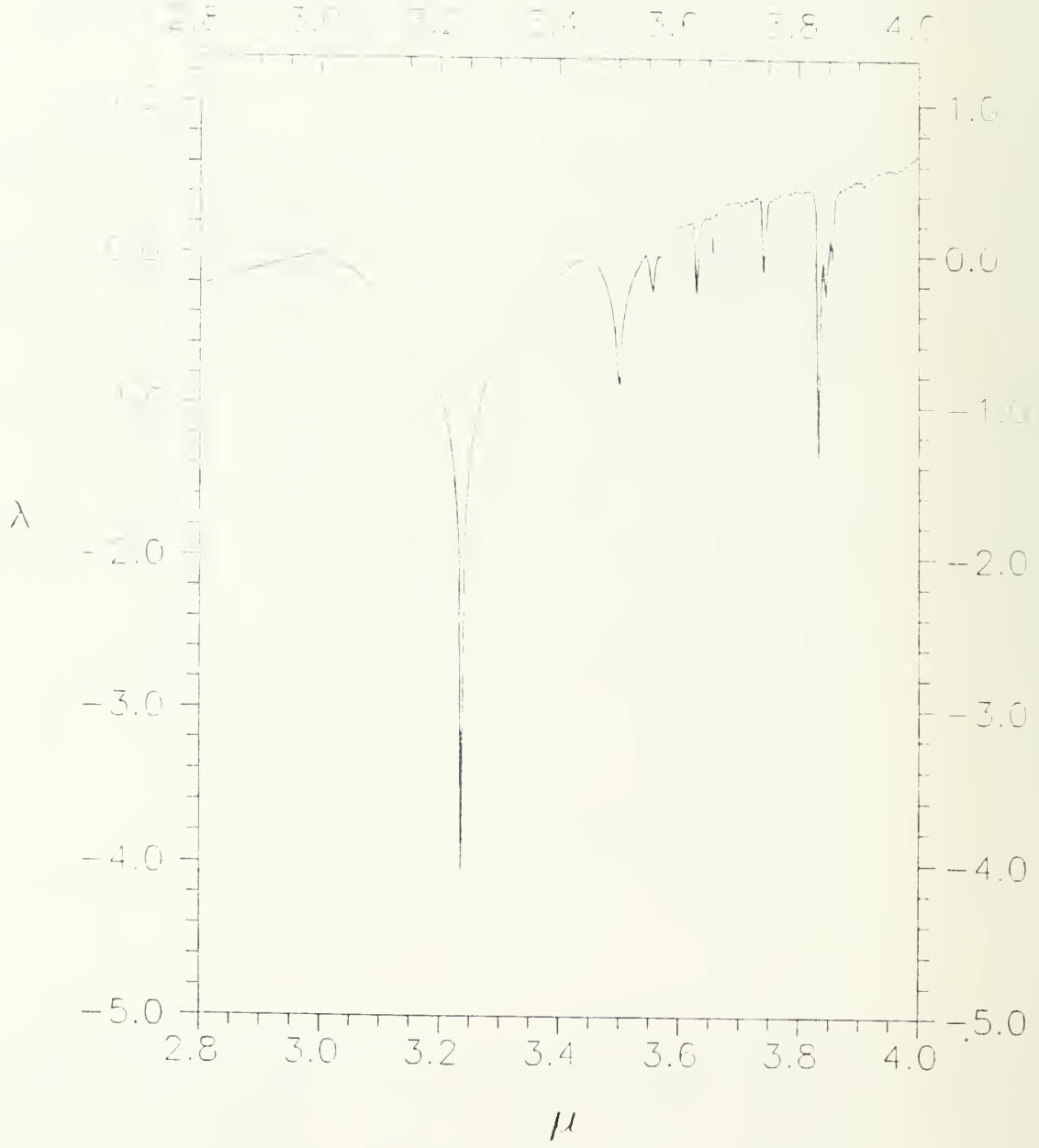

Figure 21. Lyapunov Exponent (λ) Analysis of Logistics Difference Equation, $x_{n+1} = \mu x_n(1-x_n)$.

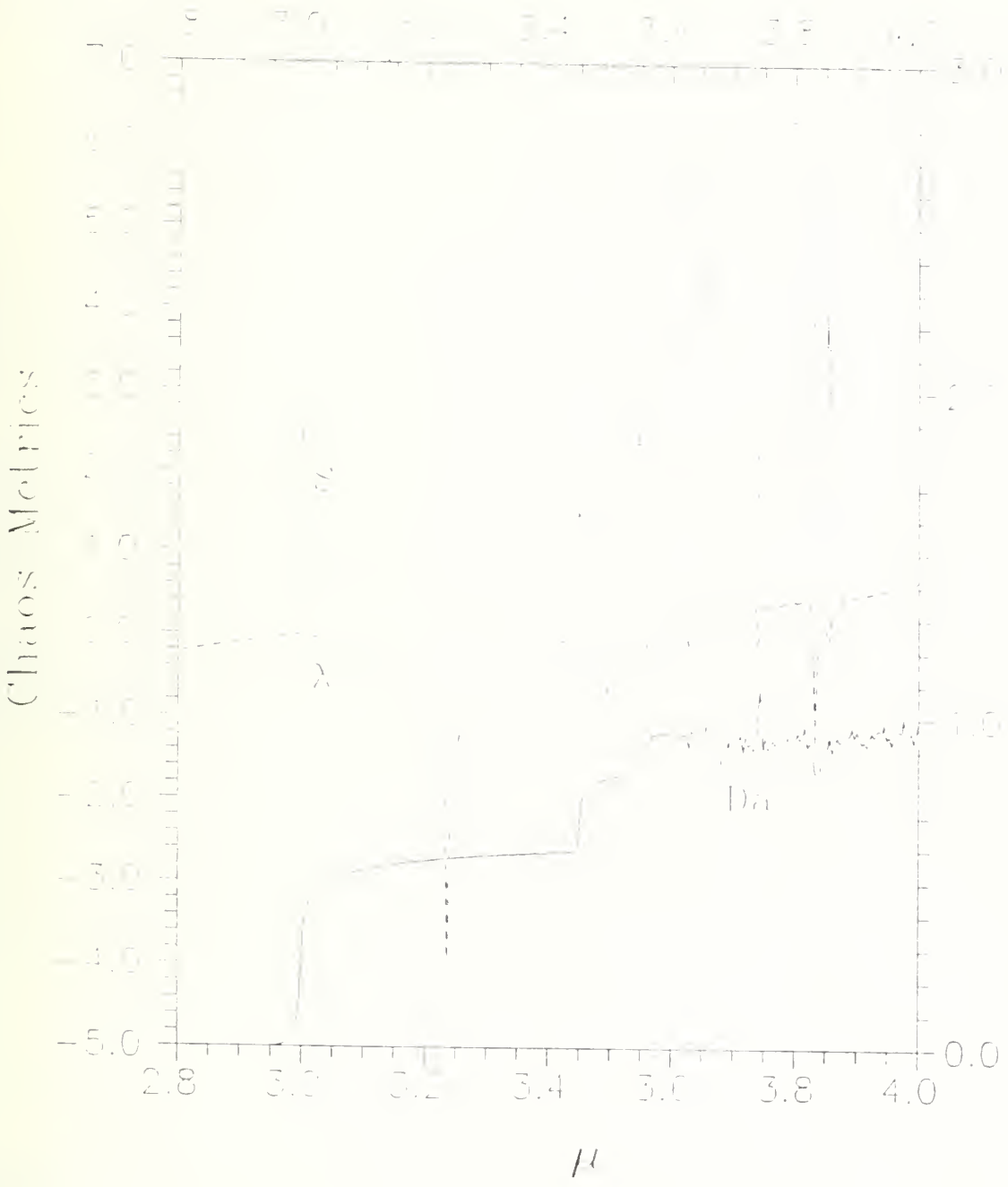

Figure 22. Fractal Dimension (D_A), Shannon Entropy (S), and Lyapunov Exponent (λ) for Logistics Difference Equation. Left axis λ; right axis S and D_A.

2. Henon Function Analysis

Since the Henon equations are a 2-D extension of the logistics difference equation, similar behavior is expected. With two dimensions, the length measurement is modified to

$$\Delta r = \sqrt{(x_{n+1} - x_n)^2 + (y_{n+1} - y_n)^2} \quad . \qquad \text{(III-3)}$$

In the period 2 case [fig. 7], a plot of $\mathrm{Log}_{10}L(k)$ vs $\mathrm{Log}_{10}k$ is very similar to the logistics difference recursion for period 2 [fig. 23]. Again, length drops to zero for every k divisible by 2. There are two slope patterns: a baseline of zero, and an upper non-zero slope (corresponding to non-even k-values). This upper slope seems quite straight, except for the largest k value.

At the onset of chaos [fig. 24], the baseline lifts again, due to the disappearance of any fixed point attractors, and the overall slope deviation becomes smaller [fig. 25]. Also $\mathrm{Log}_{10}L(k)$ only approaches zero when k is quite large. As before, for large k there are not enough distance measurements to define a mean length, nor enough points to adequately define periodicity.

When fully chaotic [fig. 7], $\mathrm{Log}_{10}L(k)$ vs $\mathrm{Log}_{10}k$ is so linear that D_A can be defined with just two data points, *i* and *o*, corresponding to a small inner and a large outer scale [fig. 26]. Then D_A is

$$D_A \equiv - \frac{\partial \ln \left[\frac{1}{\epsilon} \int_0^N |F(i+\epsilon) - F(i)| di \right]}{\partial \ln \epsilon} \quad ,$$

$$\approx \frac{\ln\left(\frac{L_o}{\epsilon_0}\right) - \ln\left(\frac{L_i}{\epsilon_i}\right)}{\ln\epsilon_0 - \ln\epsilon_i} = \frac{\ln\left(\frac{L_i}{L_0}\right)}{\ln\left(\frac{\epsilon_0}{\epsilon_i}\right)} - 1 \quad . \qquad \text{(III-4)}$$

This shows immediately that an increase in D_A implies a relative increase in the apparent magnitude of the fluctuations discernible at higher resolutions, i.e., a shift in the amplitude and hence energy spectrum toward smaller scales. It also suggests that low D_A and S may imply slowly diffusive but perhaps still highly dispersive behavior. These interpretations will be useful in analyzing the atmospheric Lagrangian particle models discussed

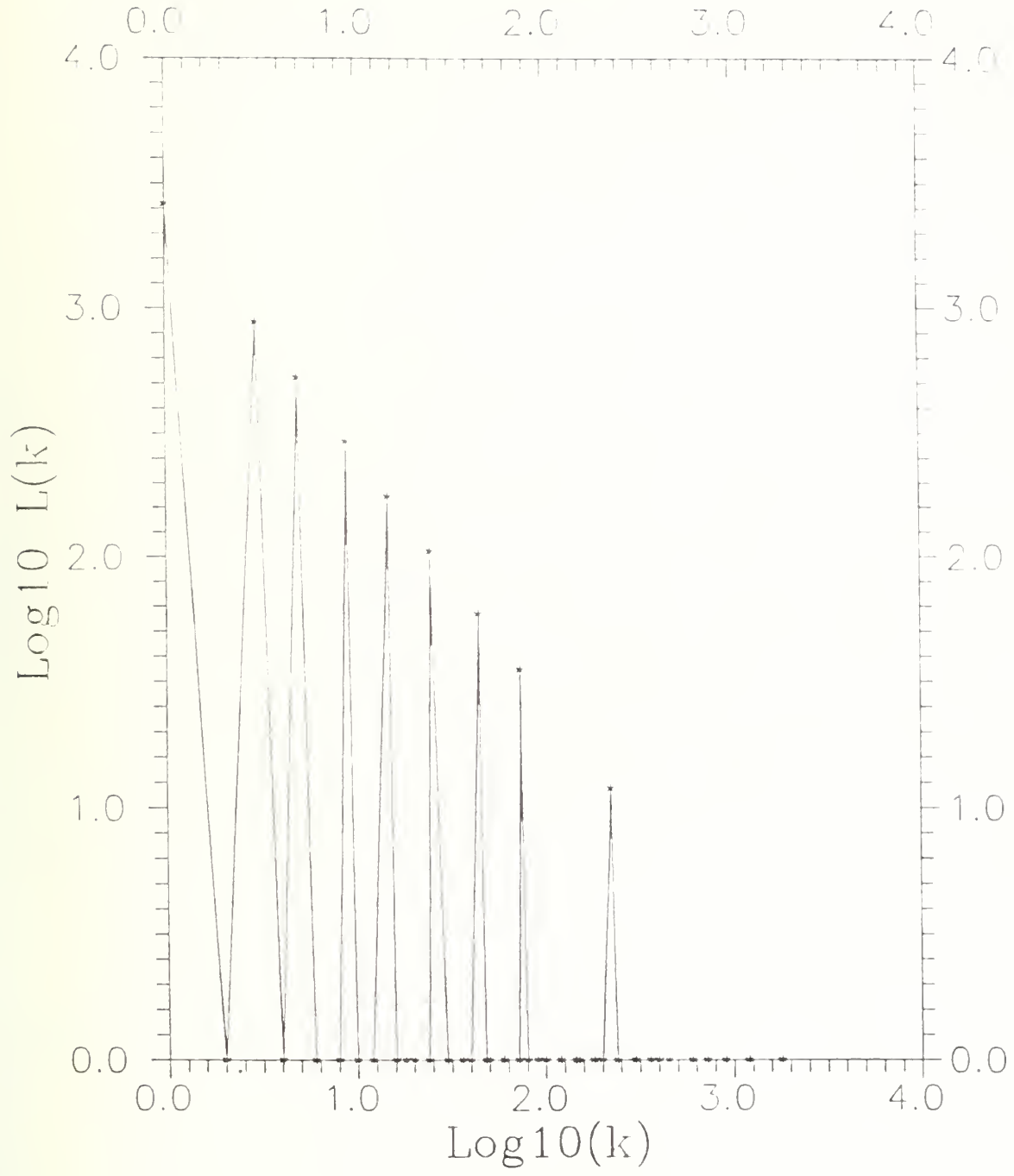

Figure 23. Henon Function, a = 0.8, b = 0.3, D_A = 0.664, Period Doubling.

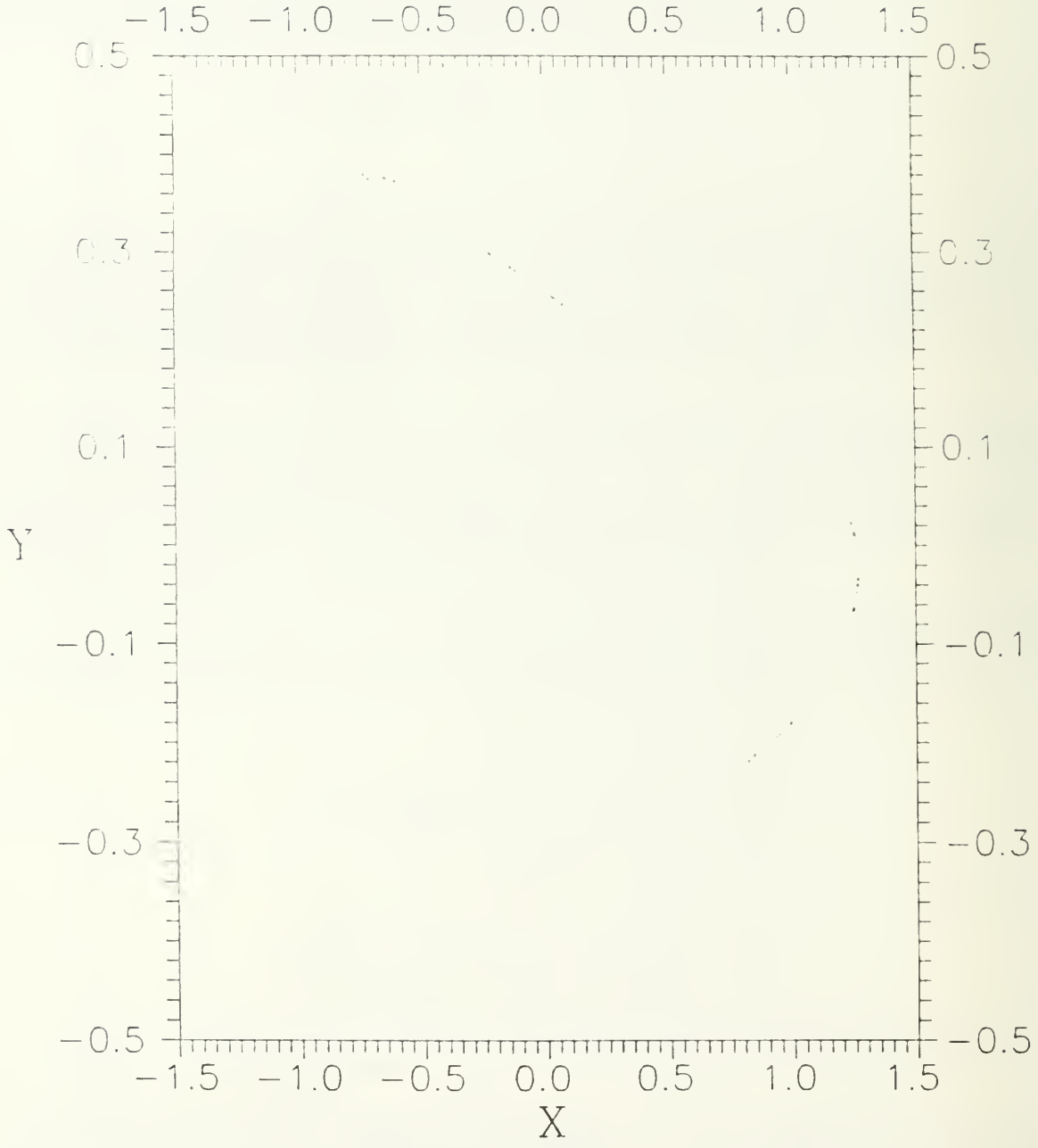

Figure 24. Henon Function, a = 1.057, b = 0.3, Onset of Chaos.

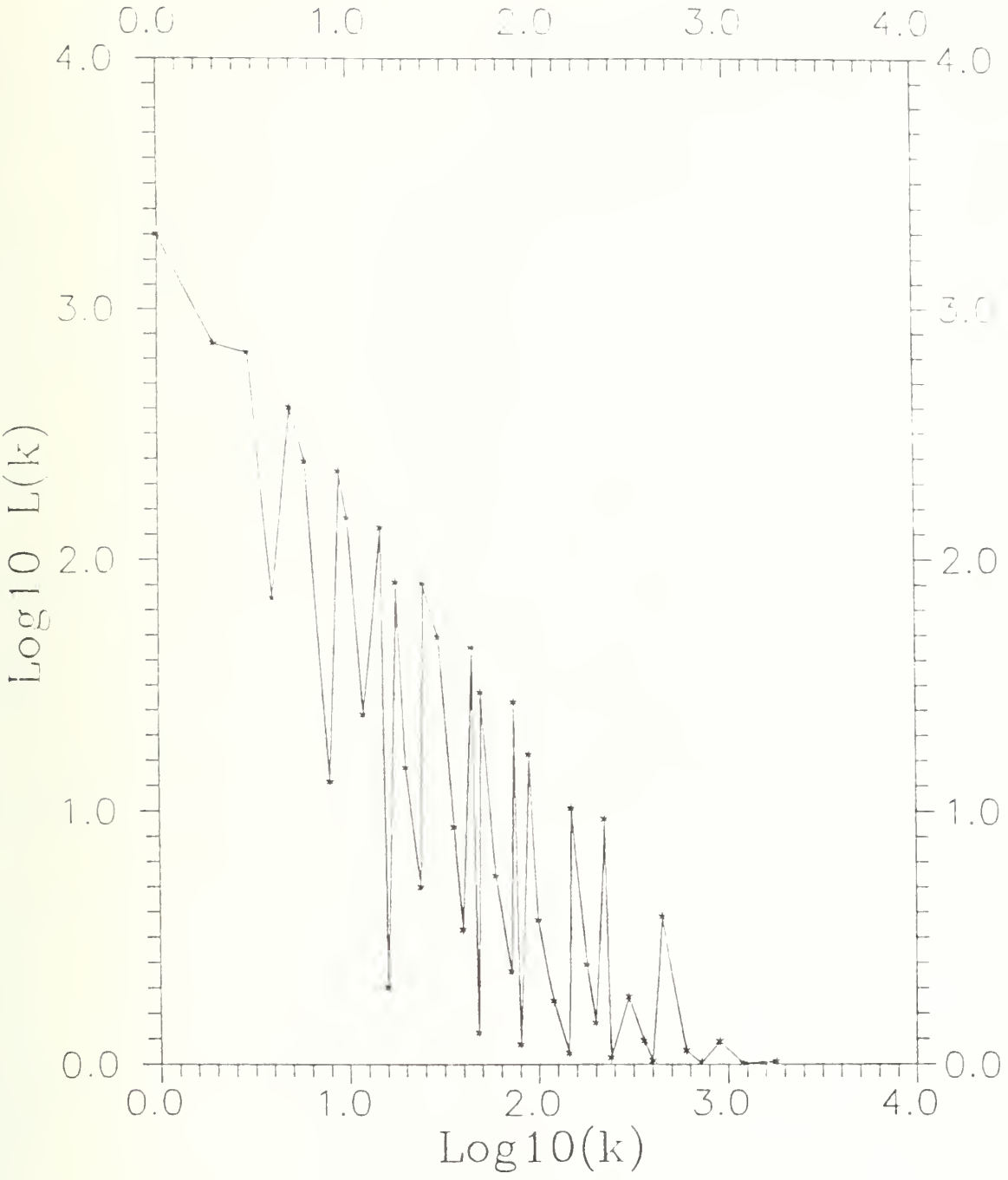

Figure 25. Henon Function, a = 1.057, b = 0.3, D_A = 1.114, Onset of Chaos.

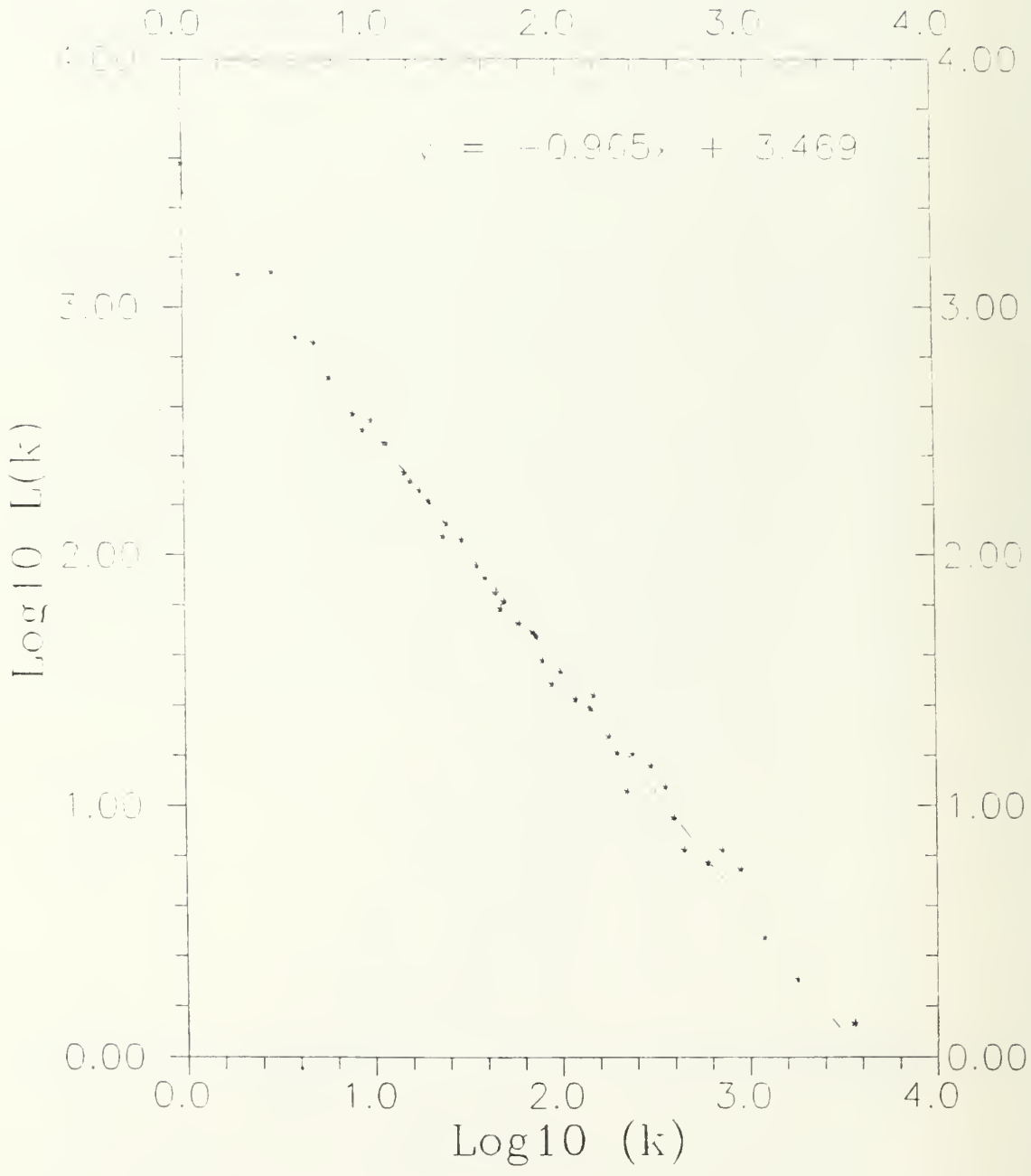

Figure 26. Henon Function, a=1.4, b=0.3, D_A=0.965.

later.

In the initial Henon bifurcation region there appears to be close correspondence between S and D_A [fig. 27]. Both show jumps occasioned by the onset of periods 2, 4, 8, and perhaps even 16. However, S and D_A sometimes show anti-correlated rather than correlated behavior whenever a window of periodicity appears within regions which are otherwise chaotic.

A higher resolution look at the region, $1.052 \leq a \leq 1.082$, displays some interesting complexity [fig. 28]. Not only are there normal bifurcations, but at $a \approx 1.062$ a new branch appears with no obvious connection to previous points. This does not correspond to the fissioning process observed earlier, but rather to an entirely new set of solutions. The new branch dictates sudden changes in the values of D_A and S. At $a \approx 1.080$, points from this new branch break away and drift toward the original branch.

At high resolution, D_A still jumps in amplitude whenever the bifurcation map shows a window of periodicity [fig. 29]. D_A, based on traversal distance along the x-axis rather than the total distance r, shows much the same: [fig. 30]. Strong peaks in D_A coincide with sharp dips in S, but sharp dips in S do not necessarily coincide with sharp peaks in D_A [fig. 31]. So a jump in average distance traversed between closely sequenced iterations always accompanies a drop in position randomness but not vice versa. This suggests that Henon periodicity also may result from the sudden appearance of fixed points less closely spaced than the mean distance between successive points in the surrounding chaos; of course D_A may again behave differently when entirely new solution lines appear which do not result from fission, as at $a \approx 1.062$.

Recognizing that there are two free parameters in the Henon equation (a and b), D_A and S were mapped for values of $0 \leq a \leq 1.5$ and $0 \leq b \leq 1.0$ [figs. 32, 33]. The two 3-dimensional maps are quite similar and suggest that $\exp(D_A)$ would be of the same order as S. The low periodicity regimes are well defined. Where D_A and S are zero, the Henon function has period 1, corresponding to one fixed attractor. The first jumps to periods 2 and 4 are well defined, as are other steps of discernible width for high a and b values, on the left and back sides of the graphical "mountain". Another feature is the behavior for high values of b, where both D_A and S show sudden increases in value. Even though S and D_A measure different parameters, the two metrics still show remarkably similar features in the Henon system.

Figure 27. Fractal Dimension (D_A) and Entropy (S) Analysis of Henon Function, with b = 0.3. Right axis: D_A. Left axis: S.

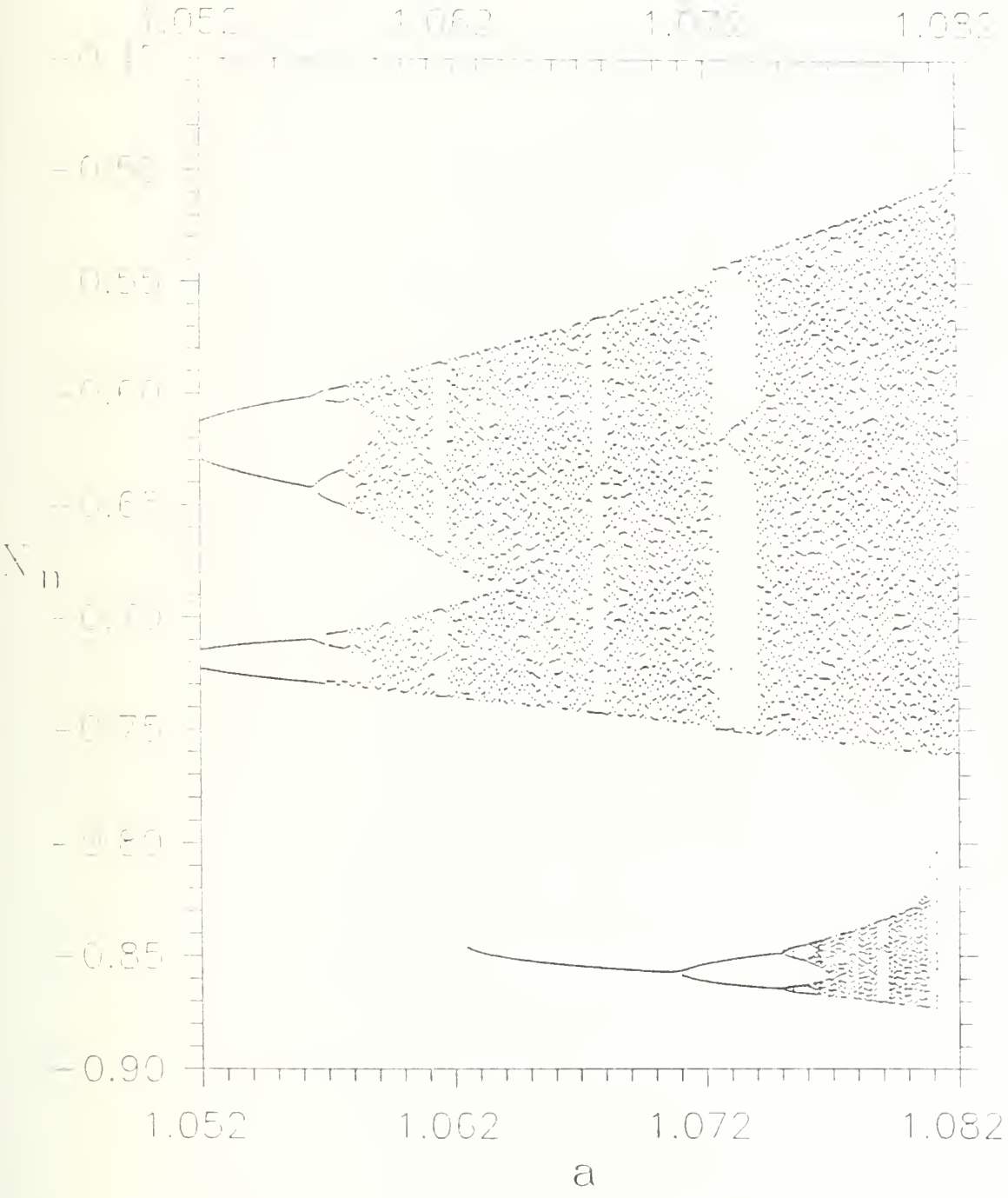

Figure 28. High resolution Henon Function Bifurcation Map, with a = 1.052 - 1.082, b = 0.3.

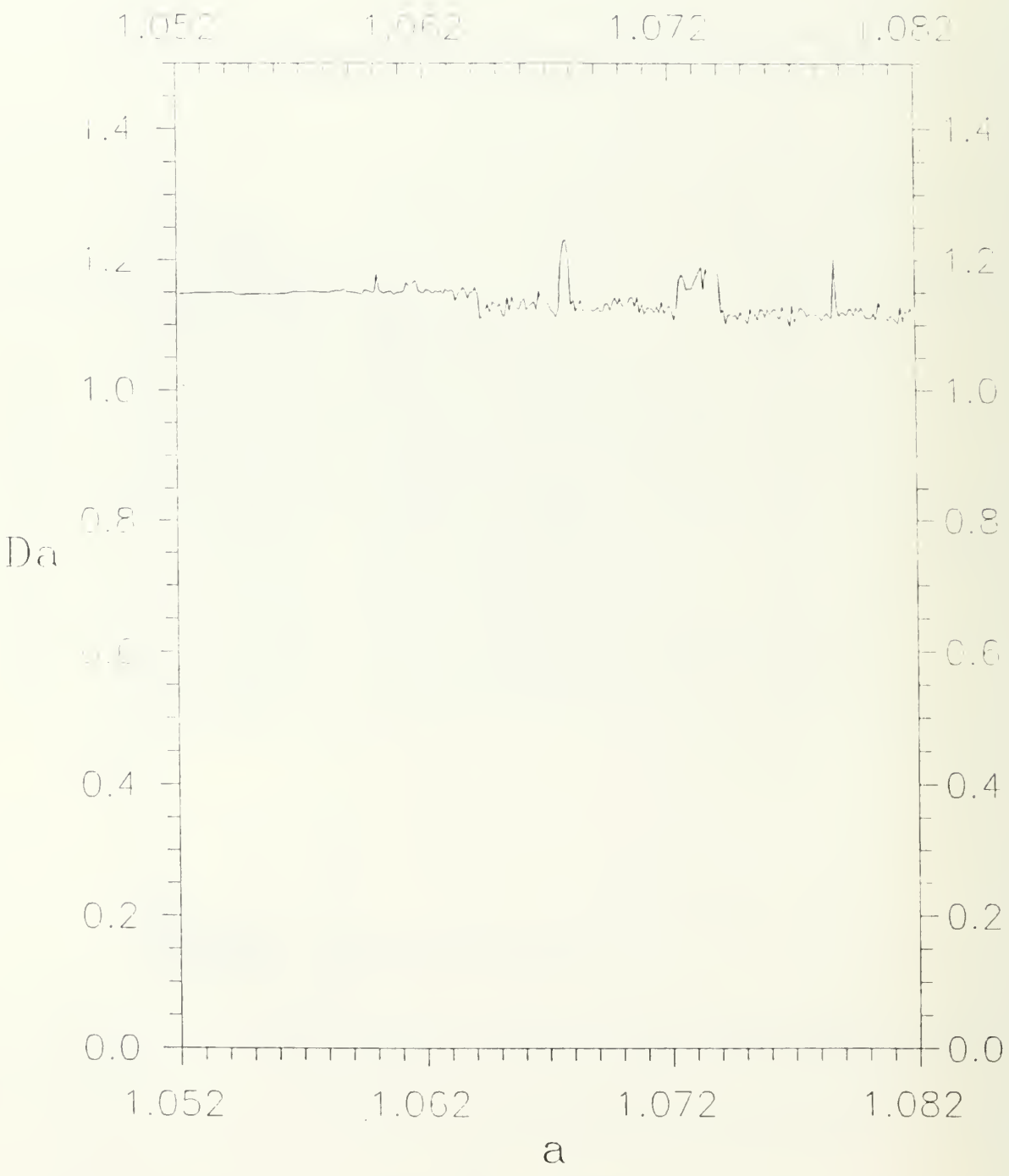

Figure 29. Fractal Dimension (D_A) Analysis of Henon Function, testing Δr with b = 0.3.

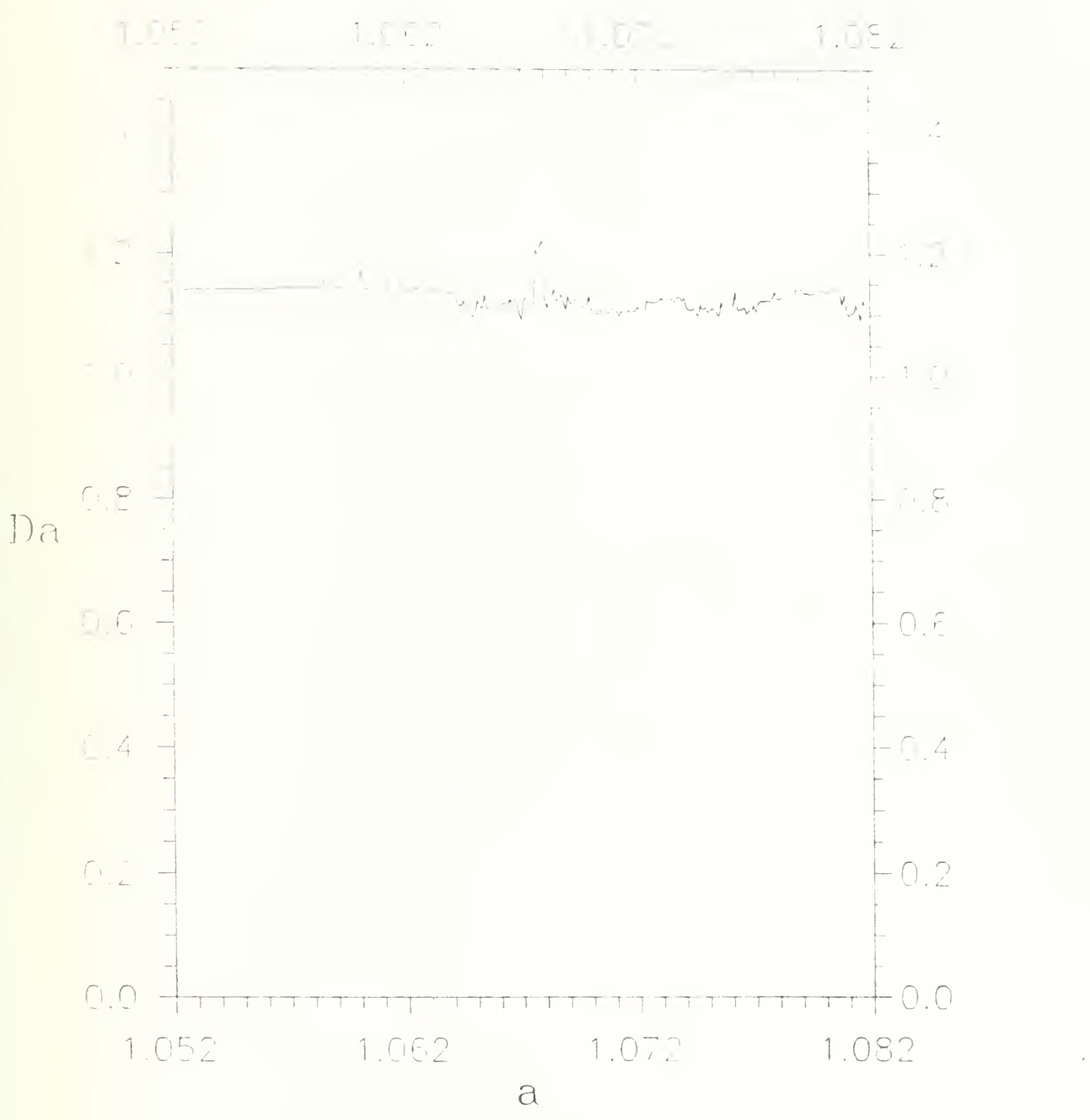

Figure 30. Fractal Dimension (D_A) Analysis of Henon Function, testing Δx, with b = 0.3.

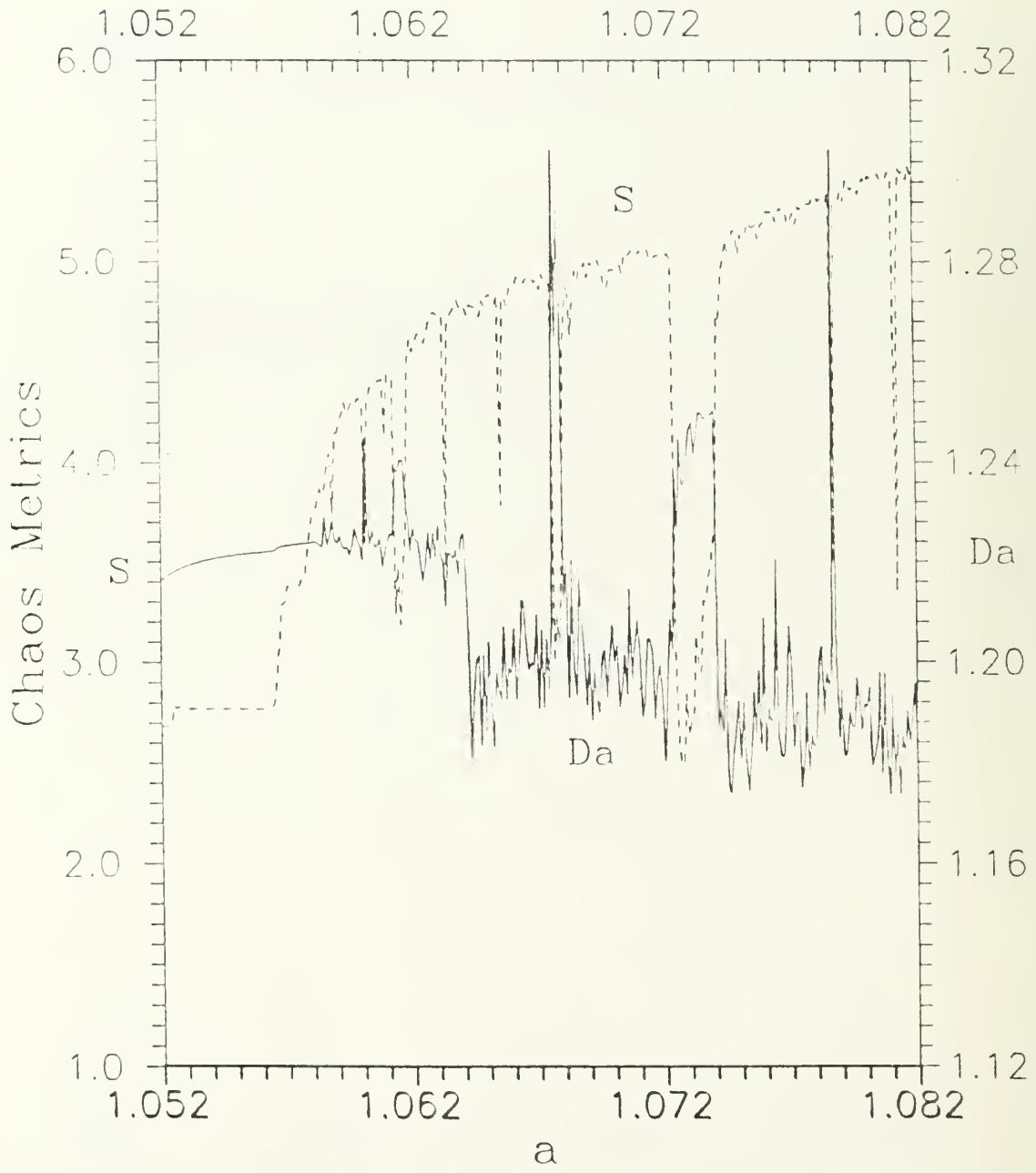

Figure 31. Comparison of Fractal Dimension (D_A), and Shannon Entropy (S) for the Henon Function, with b=0.3.

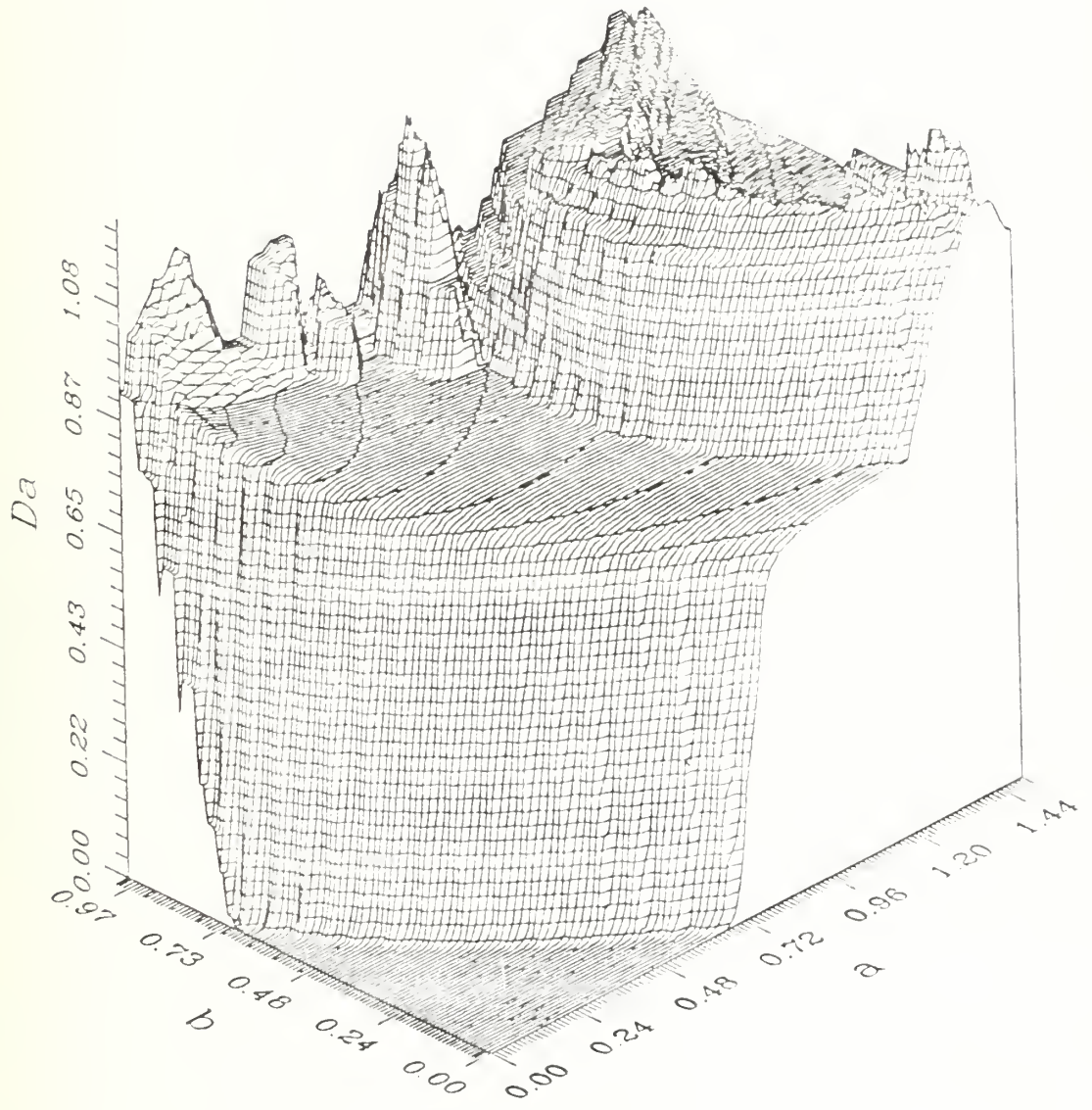

Figure 32. Fractal Dimension (D_A) Analysis of Henon Function, $x_{n+1} = 1-ax_n^2+y_n$, $y_{n+1} = bx_n$.

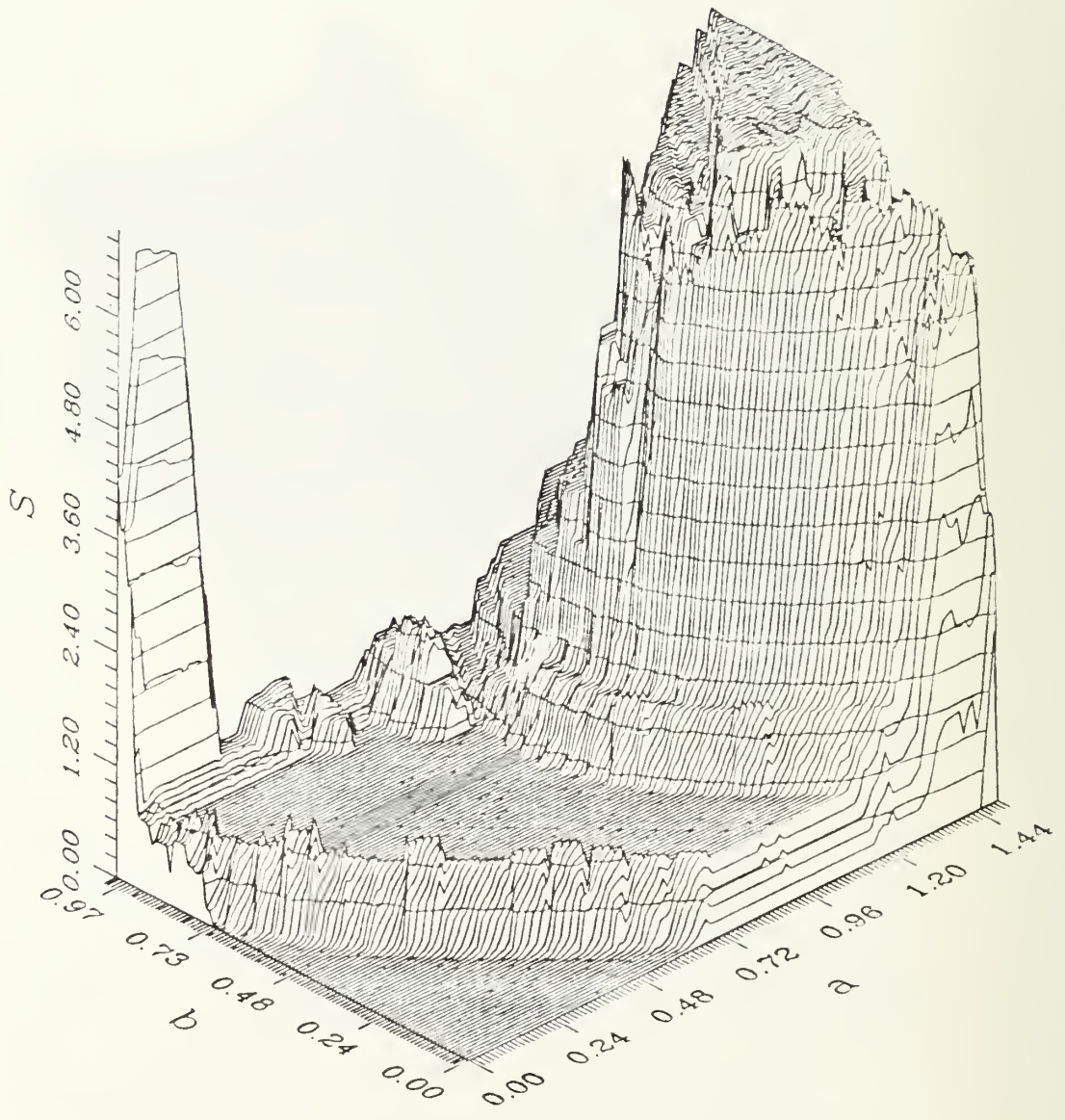

Figure 33. Entropy (S) Analysis of Henon Function, $x_{n+1} = 1-ax_n^2-y_n$, $y_{n+1} = bx_n$.

3. Conclusions drawn from Logistics Difference and Henon equation analysis

The self-affine fractal dimension, D_A, is a good discriminator of low frequencies in data, e.g., periods 2, 4, and 8 of a given length data set. However, at higher frequencies it is difficult to use D_A to distinguish periodicity from chaos. A sharp change in S always accompanies a sharp change in D_A, but not always vice versa. To explain this we note that S measures the degree of uniformity of particle position distribution and thus seems associated ultimately with diffusion or fine-scale blending; D_A measures the changing apparent jaggedness of the function as the resolution varies, indicated in chaotic regimes by the log of the ratio of the distance traversed between consecutive iterations versus distance traversed over a series of iterations. So taken together low S and high D_A seems to imply both mildly diffusive and dispersive behavior, while high S and low D_A imply both strong diffusion and dispersion. These are the main features seen in the Henon system once we move beyond the initial bifurcation regime. However, we occasionally see S drop sharply while D_A changes little, implying decreased diffusion without concommitant decreases in dispersion. This suggests that diffusion and dispersion are not equivalent even in the absence of mean flow at least in the Henon system.

In these simple systems the Lyapunov exponent provides perhaps the most definitive information: for a given value of λ, we know for certain whether the function is stable, periodic, or chaotic. Additionally, the Lyapunov exponent should be able to describe the degree of chaos: the greater the value of λ, the faster the orbital trajectory diverges, and therefore the more chaotic the function. However, the Lyapunov exponent is not so readily determined for multi-dimensional systems. The Lyapunov exponent correlates well with Shannon entropy and so seems more associated with diffusion than dispersion.

G. ATMOSPHERIC DIFFUSION MODEL ANALYSIS

1. Methodology

Three aspects of the McNider model were studied: the displacements of total and vertical position, and total velocity. Positions were measured as radial distance from the origin, arbitrarily set to x,y = 0, z = 100 meters. To enhance realism, the boundary layer inversion height was varied linearly from 2,000 to 200 meters as 1/L, the inverse Obukhov length, varied from -0.2 to 0.1 (see eqn. II-21, p. 12). Mean velocities were set to zero and total particle reflection was assumed at the ground surface and inversion.

Hints as to model behavior are again provided by the bifurcation maps, which in this context depicts the expansion and distribution

of particle range with decreasing stability as measured by 1/L. Model performance was checked against standard atmospheric measures such as the Brunt-Vaisala Frequency (BVF), tke, and vertical velocity variance (σ_w^2) (see eqn. II-17 and II-20, p. 11-12). Also computed were the two readily calculated chaos metrics: S, the entropy, and D_A, the self-affine fractal dimension, over the atmospheric range of 1/L. With 100 partitions, the maximum possible entropy in the analysis was

$$S_{max} \cong 4.6 \quad . \qquad \text{(III-5)}$$

Only the total space actually visited by the particles was so partitioned. For this study the value of 1/L was set, a single particle was released and followed for 3,600 time steps of a) Δt = 10 seconds each (10 hours total), and also for b) Δt = 0.05 times the Lagrangian time scale, T_L. Then 1/L was incremented by 0.01 m^{-1} and the run repeated until the entire stability range was spanned. Since the Lagrangian time scale tends to decrease with increasing stability, successive displacements from the original trajectory should become increasingly random as stability is increased at constant Δt. On the other hand, normalizing by T_L should keep the relative strength of the random velocity component fairly constant.

2. Results from the McNider Model Analysis

For real unstable atmospheres, the vertical velocity distribution is negatively skewed as in fig. 10. Updrafts have higher velocities and thus occupy less volume than downdrafts. However, for the initial analysis of the McNider model, the vertical velocity turbulence distribution was left unskewed. This was done to check the model without the ad hoc method McNider developed to introduce skewness, and which as outlined in Pielke (1984, pp. 178-179) appears to be incorrect.

If we plotted S and D_A at constant Δt as functions of 1/L for real turbulence, we might expect both to increase gradually with 1/L. D_A should increase because it is based on the small-to-large-time-scale displacement ratio; the amplitude spectral peaks should shift to smaller scales with increasing stability (eqn. III-4). Since the partitions used for S only span the range of locations actually visited by the particle, S does not account for range shrinkage with increasing stability. So we expect for constant Δt that S may also increase with stability, since total simulation time increases relative to the Lagrangian time scale. If the time step is instead a fixed fraction of the Lagrangian time scale, then we might expect both S and D_A to remain fairly constant despite changes in 1/L. However, for constant Δt strong stability may decrease S by vitiating turbulence into low order chaos. The random component of

diffusion in the models prevents the appearance of purely periodic patterns.

For the McNider model we see instead, for Δt = 10 secs on the negative (unstable) side, that S is fairly constant up to 1/L = 0, while D_A declines slowly but steadily [fig. 34]. Near the neutral transition, D_A spikes upward as expected, fluctuates in the mildly stable regime, then climbs slowly. S fluctuates violently across the slightly unstable-to-moderately stable regime, then falls steadily with increasing stability. For $\Delta t = 0.05T_L$ in the unstable regime, we see slight decreases in both S and D_A, violent fluctuations across the neutral transition amid general decreases, and steep increases in both at stronger stabilities [fig. 35].

The model's fluctuations in the near neutral regime are more likely due to discontinuities in the asymptotic values as stable boundary layer algorithms replace ones for unstable conditions. As stability varies, the maxiumum wavelength algorithms also do not remain well-proportioned with respect to the standard deviation of velocity. So T_L also fluctuates substantially in this region.

The tke in the bulk of the real boundary layer and in large eddy simulations is fairly isotropic. So in the unstable and near-neutral regimes the vertical velocity variance should be about two-thirds the magnitude of the total tke, defined as $(1/2)(\sigma_u^2 + \sigma_v^2 + \sigma_w^2)$. This ratio should decrease gradually with 1/L as stability supresses vertical motions. Instead in both figs. 34 and 35 the McNider model shows the σ_w^2/tke ratio exceeding unity in the unstable region, dropping to near zero across the transition, climbing to a small peak along with total tke at moderate stability levels, then gradually subsiding to near zero again as stability increases. The dip to near zero is due to the very low mean wind shear values in these flow simulations. This may not be as significant a problem in the prognostic windflow models for which the McNider model was originally designed as it is in the similarity-based flow model simulator used in this study. However, an artificial "dip" would probably still appear. The tke and σ_w^2 values are also much too large. An expected maximum σ_w^2 might be ~ $10 m^2/s^2$, while the plots show ~ 25-35 m^2/s^2. The Brunt-Vaisala frequency is plotted in the stable regime to ensure that the actual stability encountered by the Lagrangian particle indeed increases monotonically with 1/L.

For real turbulence we might expect the total range of locations visited to decrease steadily with increasing stability; the decrease would probably be steeper, if the measurement time step remained proportional to the steadily diminishing Lagrangian time scale. The McNider bifurcation diagram for Δt = 10 secs shows as expected that the total range of positions decreases steadily with increasing stability for 1/L < 0 [fig. 36]. However, it drops

discontinuously across the neutral transition, then quite slowly in the stable regime beyond $1/L = 0$. The general pattern is repeated for $\Delta t = 0.05\ T_L$ [fig. 37], except that we see unrealistic

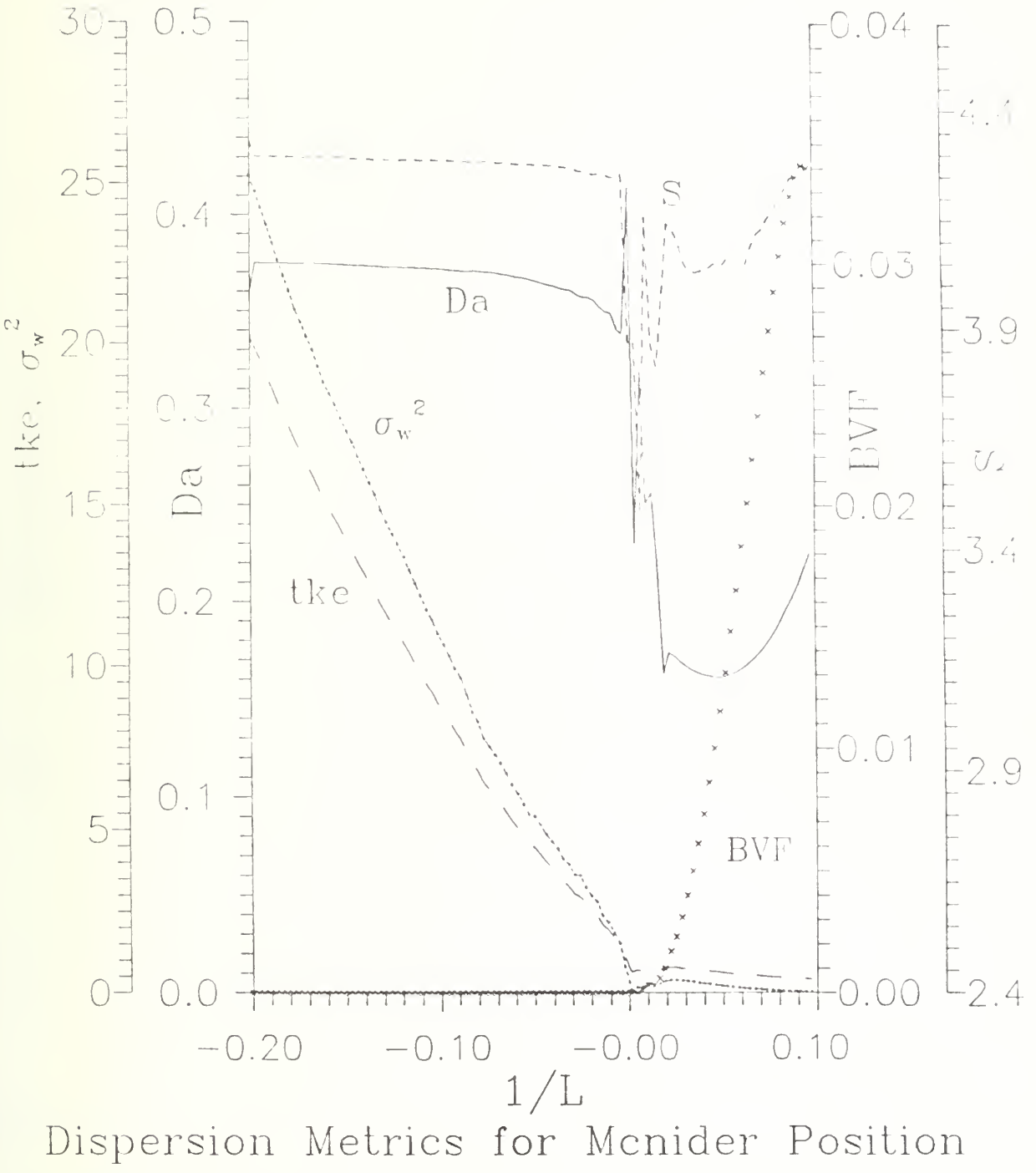

Figure 34. McNider Particle Dispersion Model. D_A, S, σ_w^2, tke, and BVF versus 1/L. Δt = 10 secs.

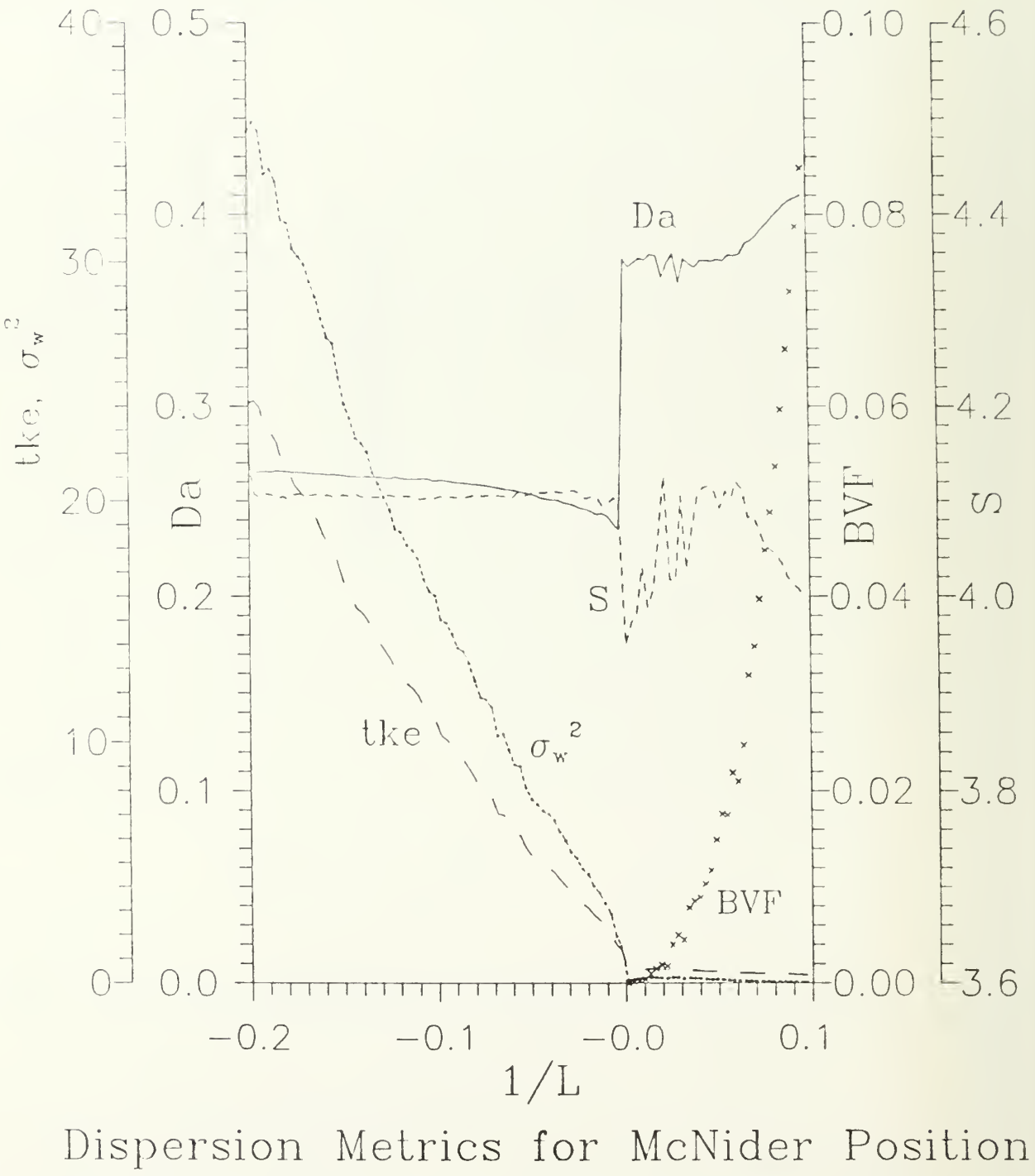

Figure 35. McNider Particle Dispersion Model. D_A, S, σ_w^2, tke, and BVF versus 1/L. $\Delta t = 0.05\ T_L$.

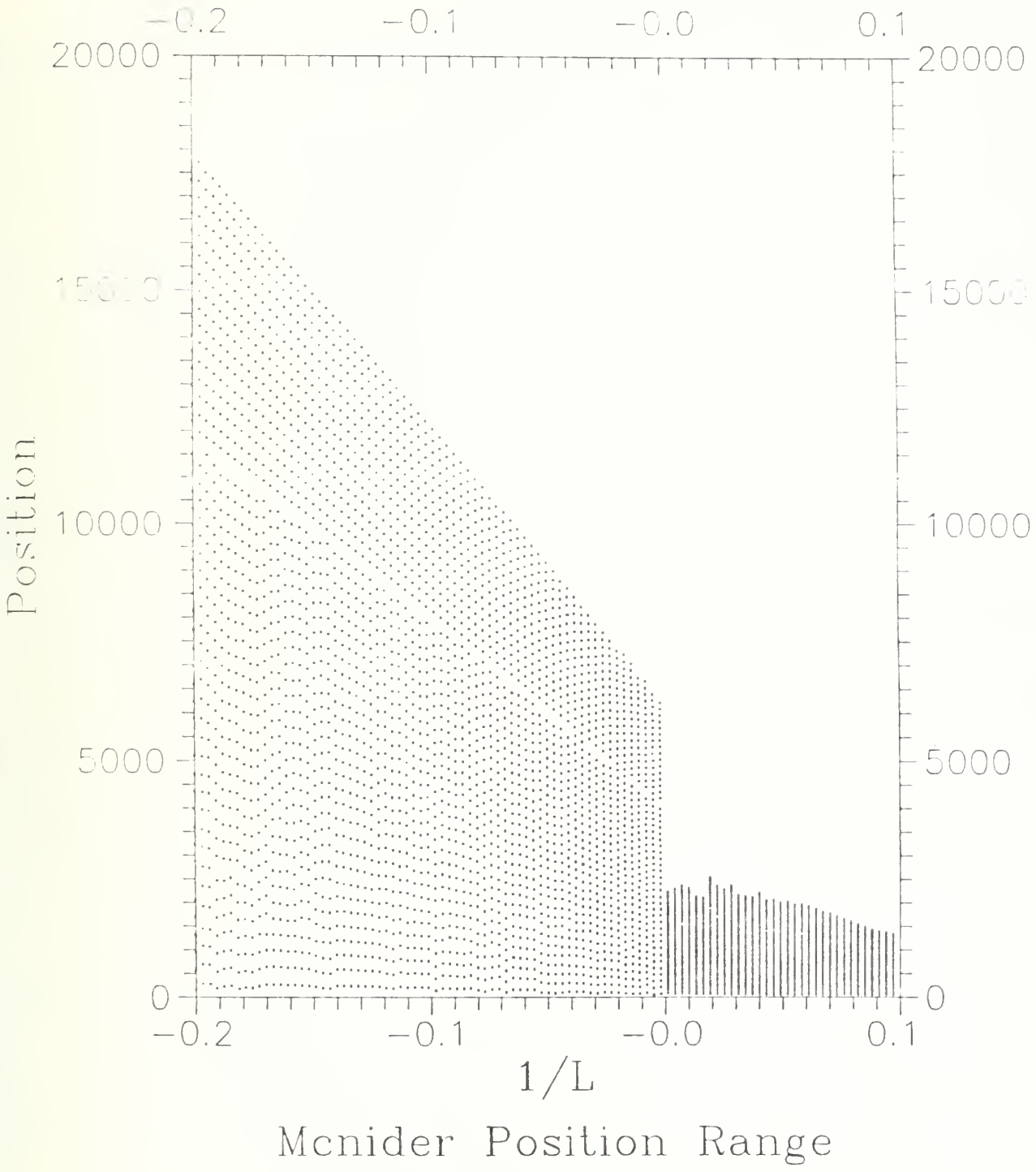

Figure 36. McNider Particle Dispersion Model bifurcation map. Shows total displacement range versus 1/L. Δt = 10 secs.

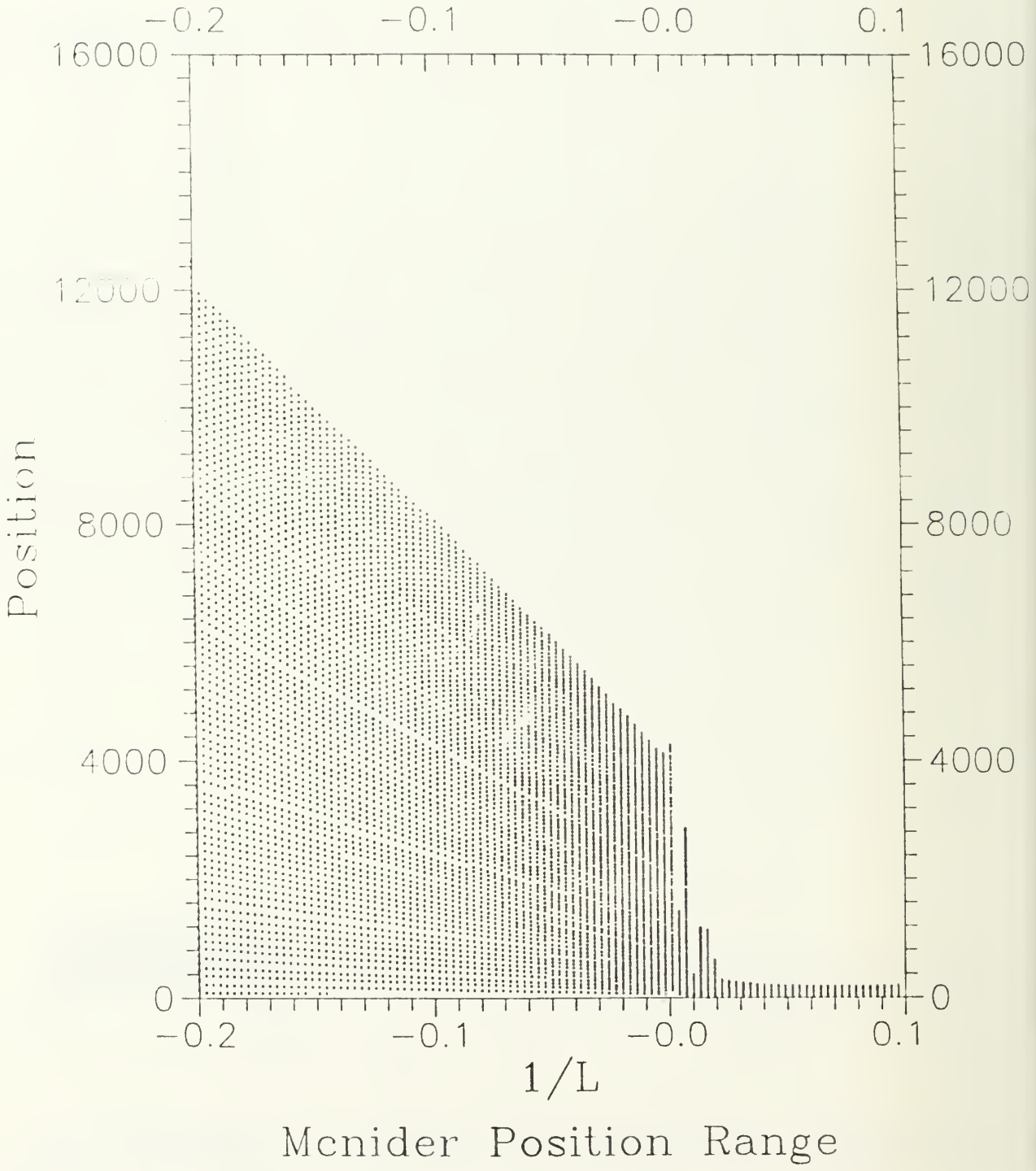

Figure 37. McNider Particle Dispersion Model bifurcation map. Shows total displacement range versus 1/L. $\Delta t = 0.05\ T_L$.

fluctuations across the neutral transition, while the range in the stable regime is much smaller, as expected.

If the above metrics are applied only to vertical rather than total displacement, the behavior appears quite different. We would expect stronger stability effects on purely vertical motions, so that the trends seen in the total displacement plots would appear more exaggerated. However, the results are more complex than that. For Δt = 10 secs D_A fluctuates more in the unstable regime and particularly across the neutral transition [fig. 38]. D_A decreases as neutrality is approached, then assumes a generally constant value in the stable regime. So vertical behavior exaggerates the total displacement trends for D_A in the unstable regime, but the jump across neutrality is not seen, nor is the rise in the stable regime. This suggests that the jump and rise were engendered mostly by algorithms for the horizontal boundary layer parameters. On the other hand in the unstable regime, S generally rises with increasing stability, jumps sharply across the transition, fluctuates substantially in moderate stability, then falls drastically as stability strengthens. This behavior might be interpreted as mostly exaggerations of those seen for total displacement, except that S jumps rather than drops at neutral stability. The similarities between total and vertical displacement behavior are more striking for $\Delta t = 0.05\ T_L$ [fig. 39]. S tends generally upward with stability interrupted by fluctuations near neutrality. D_A drops precipitously at neutrality, but both the stable and unstable regimes are fairly constant. The upward rise in D_A seen at stronger stabilities in the total displacement plot is not seen for purely vertical motions. So the upward trend is not due to strengthening stability. In fact we cannot immediately correlate some of these differences with specific features of the boundary layer algorithms, but these artifacts do stray from expectations based on real atmospheric turbulence. The McNider vertical position range plots (bifurcation maps) are quite similar to the ones for total displacement with a discontinuous drop across neutrality for Δt = 10 secs and fluctuations for $\Delta t = 0.05\ T_L$ [figs. 40 and 41].

If we plot total velocity rather than displacement, for Δt = 10 secs D_A seems roughly constant save for a slight jump across neutrality, while S shows a bigger jump at the same point [fig. 42]. For $\Delta t = 0.05\ T_L$ S shows a similar neutrality jump amid a definite rising trend. On the stable side D_A decreases quickly then rises at stronger stabilities [fig. 43]. Again for real turbulence we might expect generally rising trends for both at constant Δt, but such trends might be factored out by normalizing Δt by T_L.

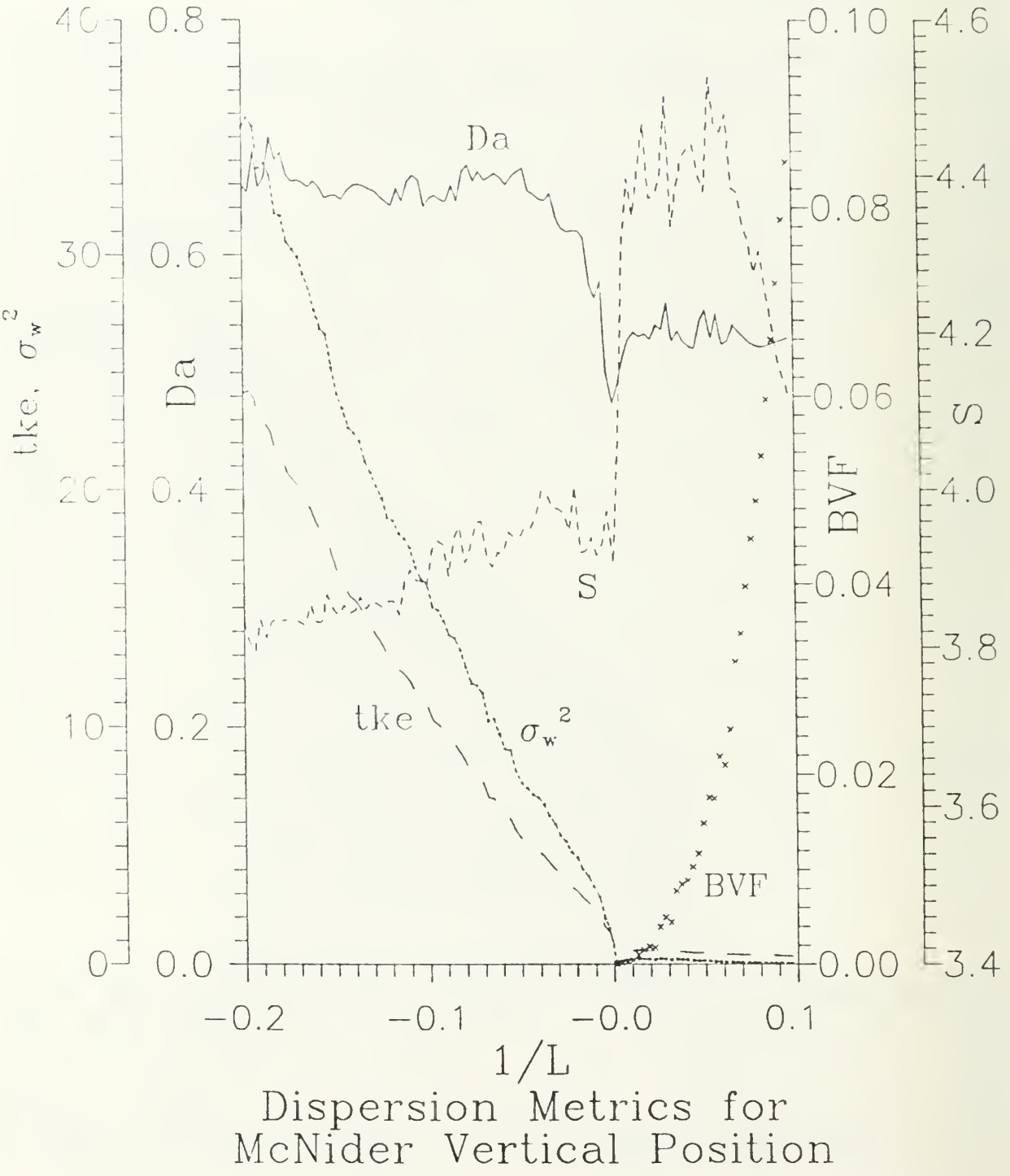

Figure 38. McNider Particle Dispersion Model. Same as fig. 34 except for vertical displacements only.

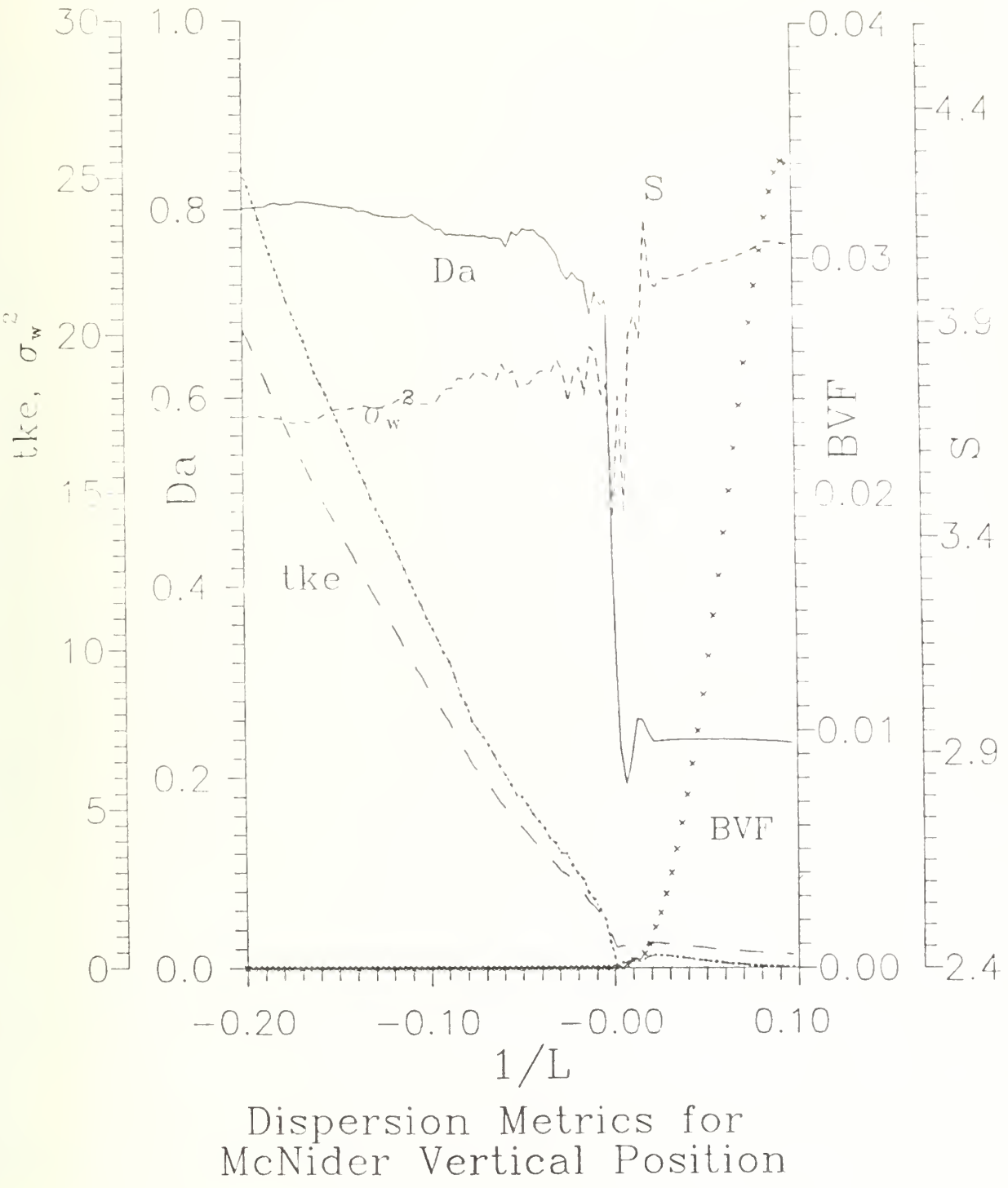

Figure 39. McNider Particle Dispersion Model. Same as fig. 35. except for vertical displacements only.

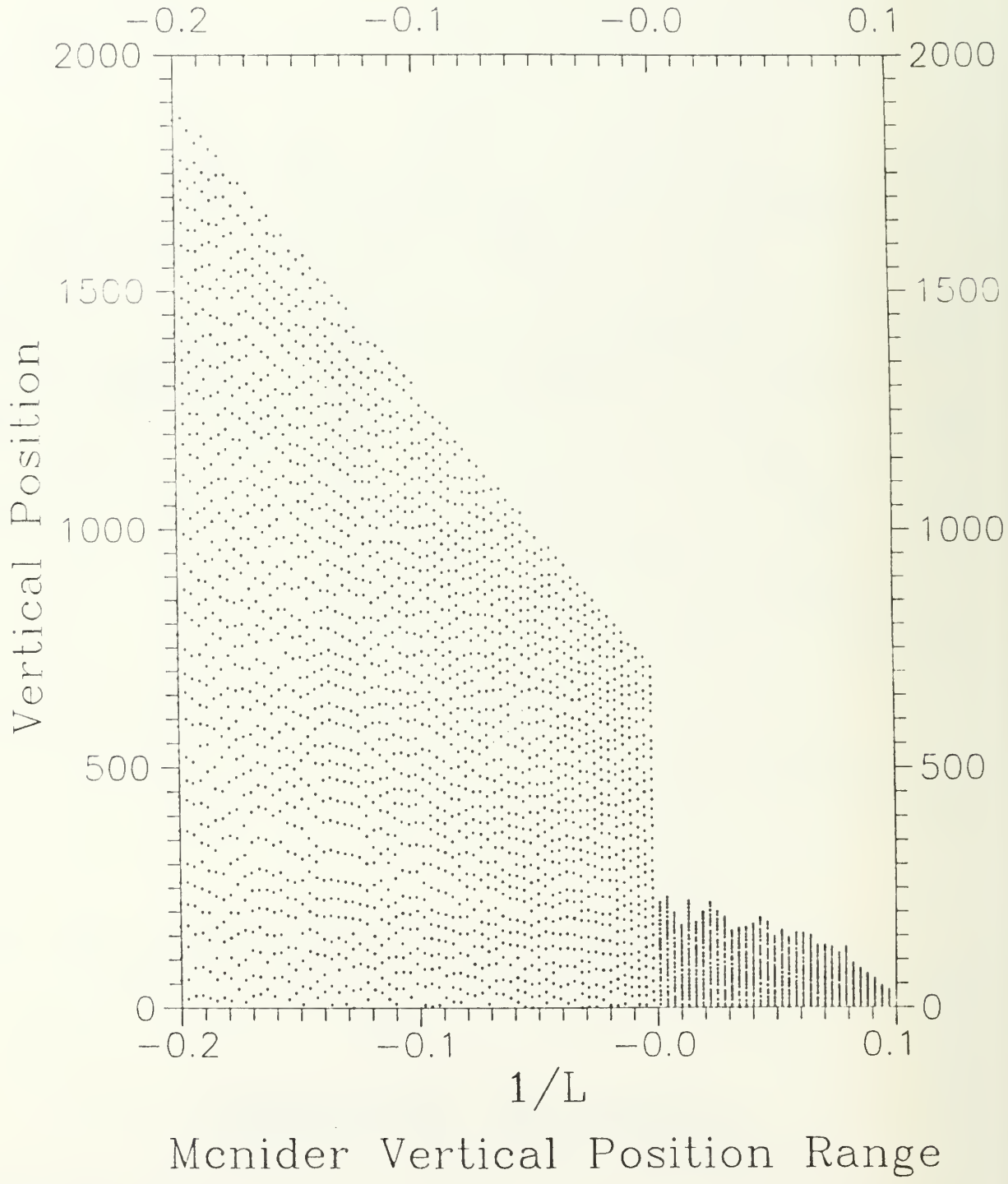

Figure 40. McNider Particle Dispersion Model bifurcation map. Same as fig. 36, except for vertical displacements only.

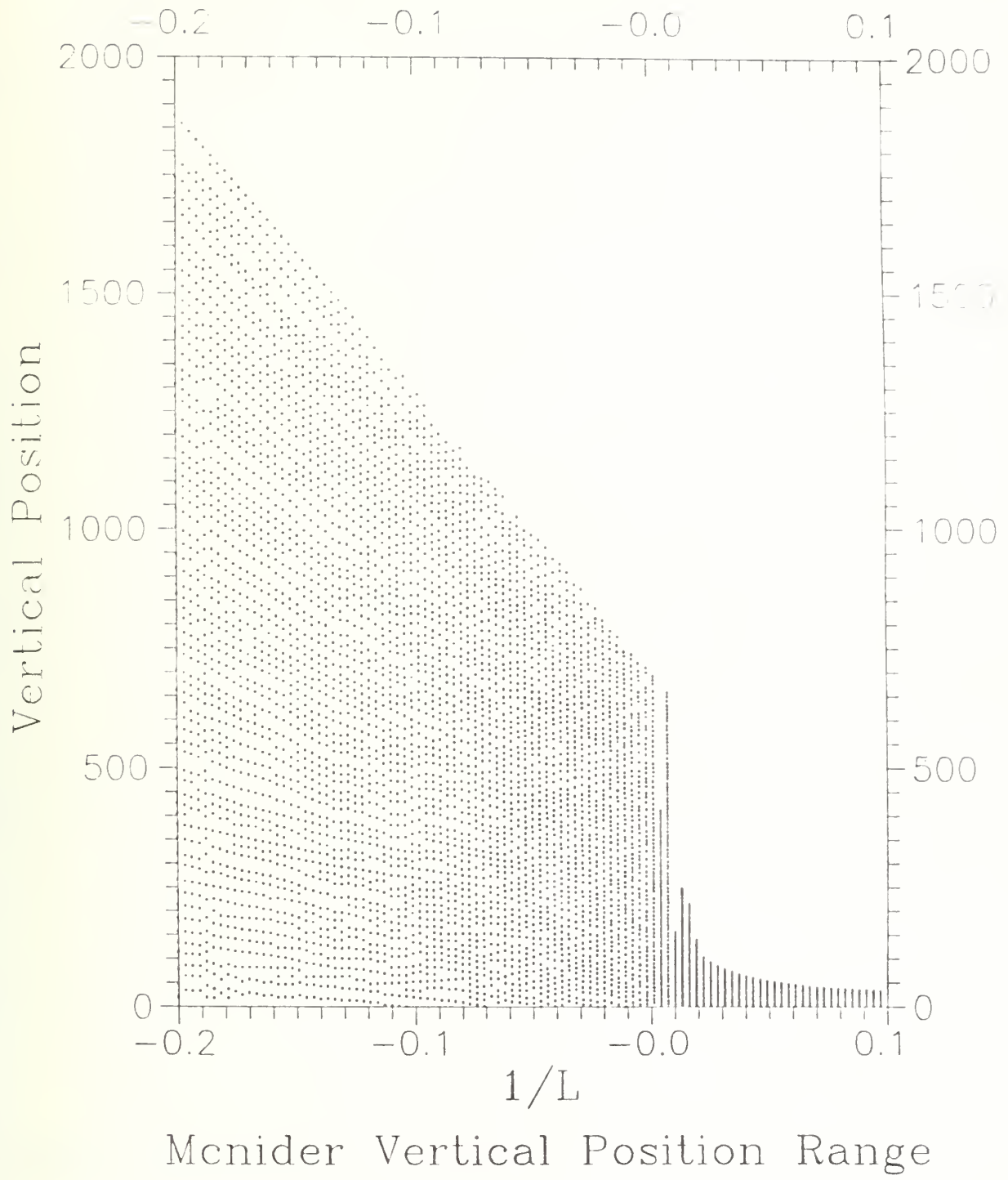

Figure 41. McNider Particle Dispersion Model bifurcation map. Same as fig. 37, except for vertical displacements only.

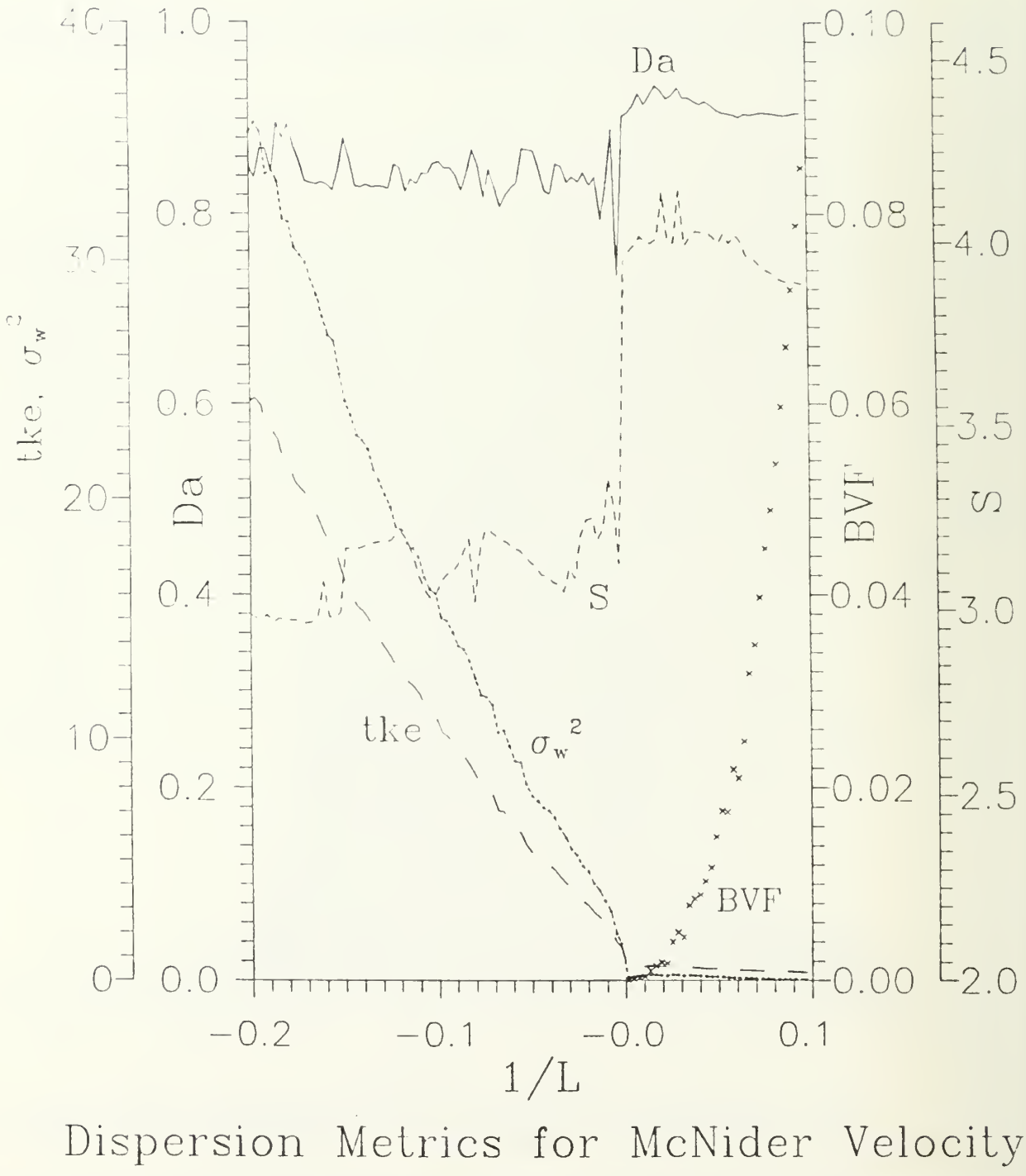

Dispersion Metrics for McNider Velocity

Figure 42. McNider Particle Dispersion Model. Same as fig. 34, except that total velocity is substituted for total displacement.

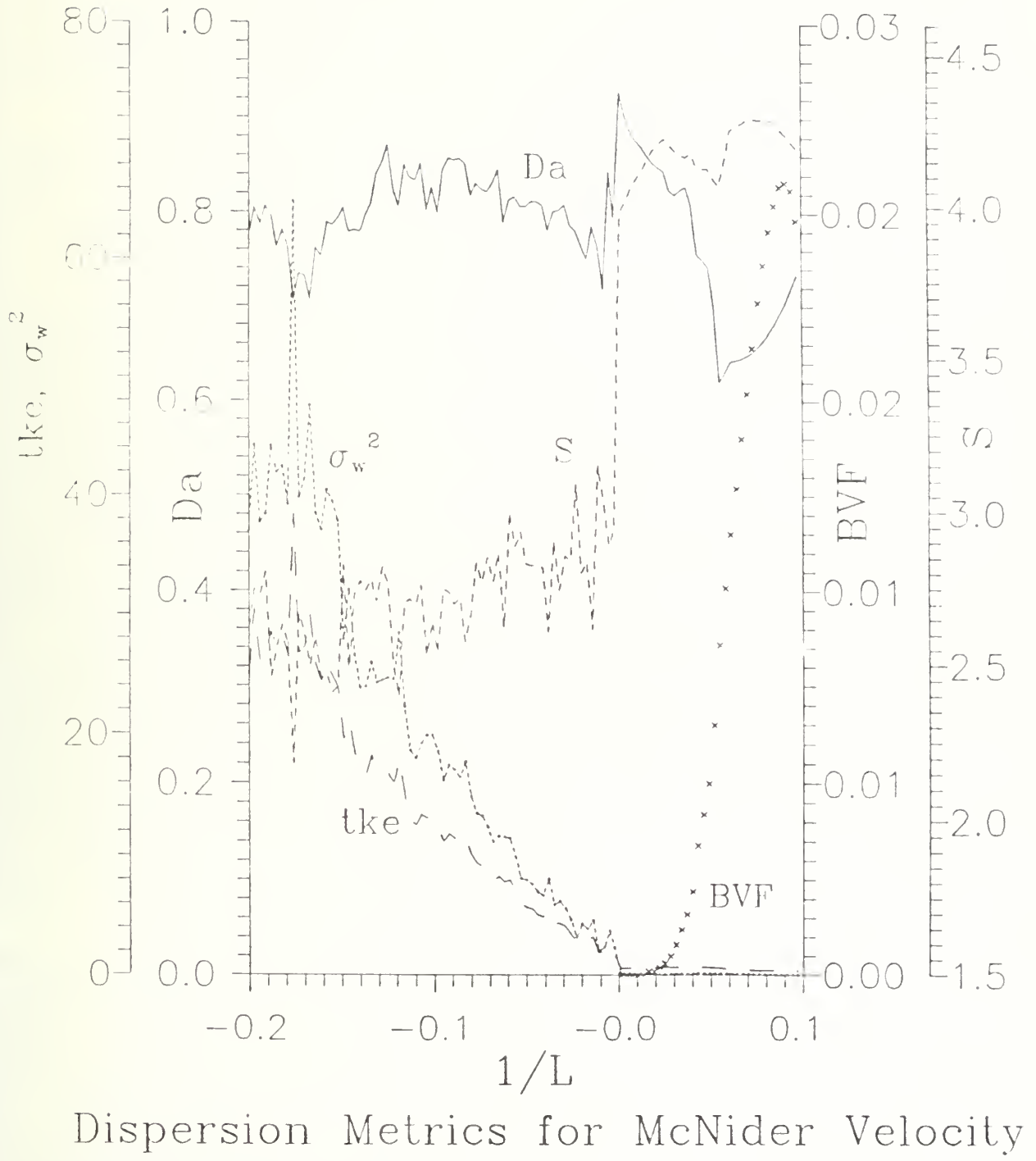

Figure 43. McNider Particle Dispersion Model. Same as fig. 35, except that total velocity is substituted for total displacement.

The bifurcation maps for both constant and T_L normalized Δt show more scatter and the magnitude ranges are unrealistically large in the unstable regime, particularly for $\Delta t = 0.05\ T_L$ [figs. 44 and 45]. Evidently, these features result from the McNider algorithms for the velocity standard deviations, maximum wavelengths, and Lagrangian time scales. Again, we also see a fluctuation at neutrality and a sudden dip in velocity range at moderate stabilities. The cause of the latter is not obvious.

If MKS units are retained, the total velocities are quite small compared to total displacements, so phase velocity plots are almost identical to total position plots, so are not shown.

3. Results from the LPM Model Analysis

The LPM model [figs. 46 and 47] avoids the problems of the McNider model [figs. 34 and 35] regarding inappropriately high values for velocity, turbulence kinetic energy, and vertical velocity variance in the unstable regime. Also, the σ_w^2/tke ratios better reflect the behavior of real fluids: σ_w^2/tke exceeds 2/3 for unstable values of 1/L, but not for stable ones. The sharp discontinuity crossing neutrality is somewhat reduced. Presumably stochastic fluctuations in D_A and S remain evident in the unstable regime, but both rise rather than fall across the neutral zone when monitoring total displacement at $\Delta t = 10$ secs. The general trend in D_A is clearly upward with increasing stability. Both metrics rise at stronger stabilities, but there are slight dips at moderate stability. For $\Delta t = 0.05\ T_L$ S remains roughly constant with stability except for a sudden reverse spike at $1/L = 0$. This seems more in keeping with the behavior expected for real turbulence. However, the D_A behavior is puzzling; it increases even more rapidly with stability, leaps at neutral, then drops precipitously and monotonically in the stable regime as 1/L grows more positive. One possible interpretation is that once positive stability is achieved, the LPM algorithms dictate a drastic decrease in maximum wavelength which propels D_A to large values, but the smaller displacements may themselves diminish with increasing stability within the stable regime, if the time increments keep shrinking.

The total position displacement plots (bifurcation maps) show some stochastic scatter in the general decrease with stability and a sudden drop at neutrality for both $\Delta t = 10$ secs and $0.05\ T_L$ [figs. 48 and 49]. For $\Delta t = 0.05\ T_L$ a small hump is seen in the slightly stable regime before diminishing to rather small values for strong stability. There are a number of competing effects. However, the computed Lagrangian time scale may actually increase temporarily in the slightly stable regime. Recall that the maximum wavelengths in the stable regime are the same as those used in McNider (eqns. II-36 and II-43). However, the velocity standard deviations are

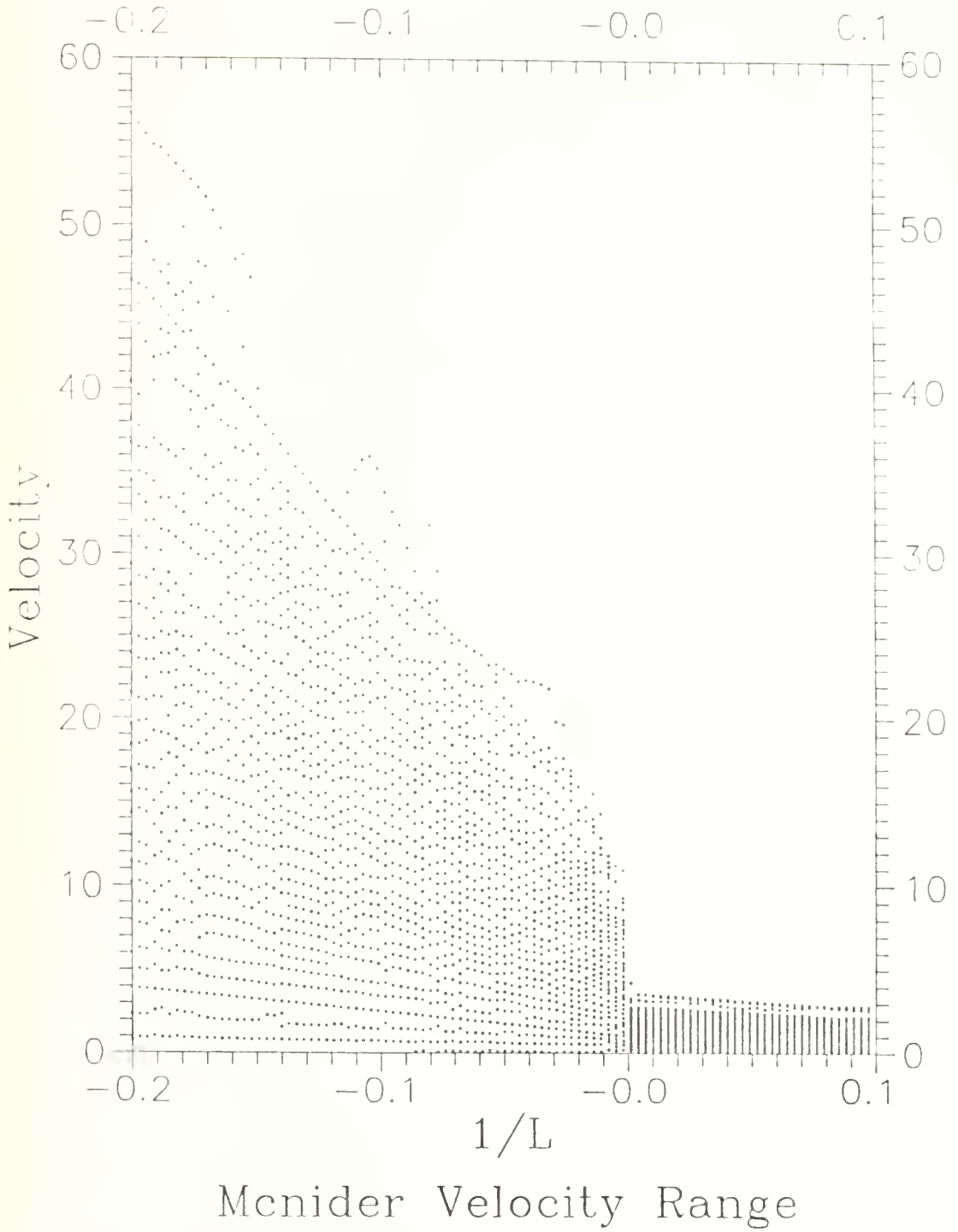

Figure 44. McNider Particle Dispersion Model bifurcation map. Same as fig. 36, except using total velocity in place of total displacement.

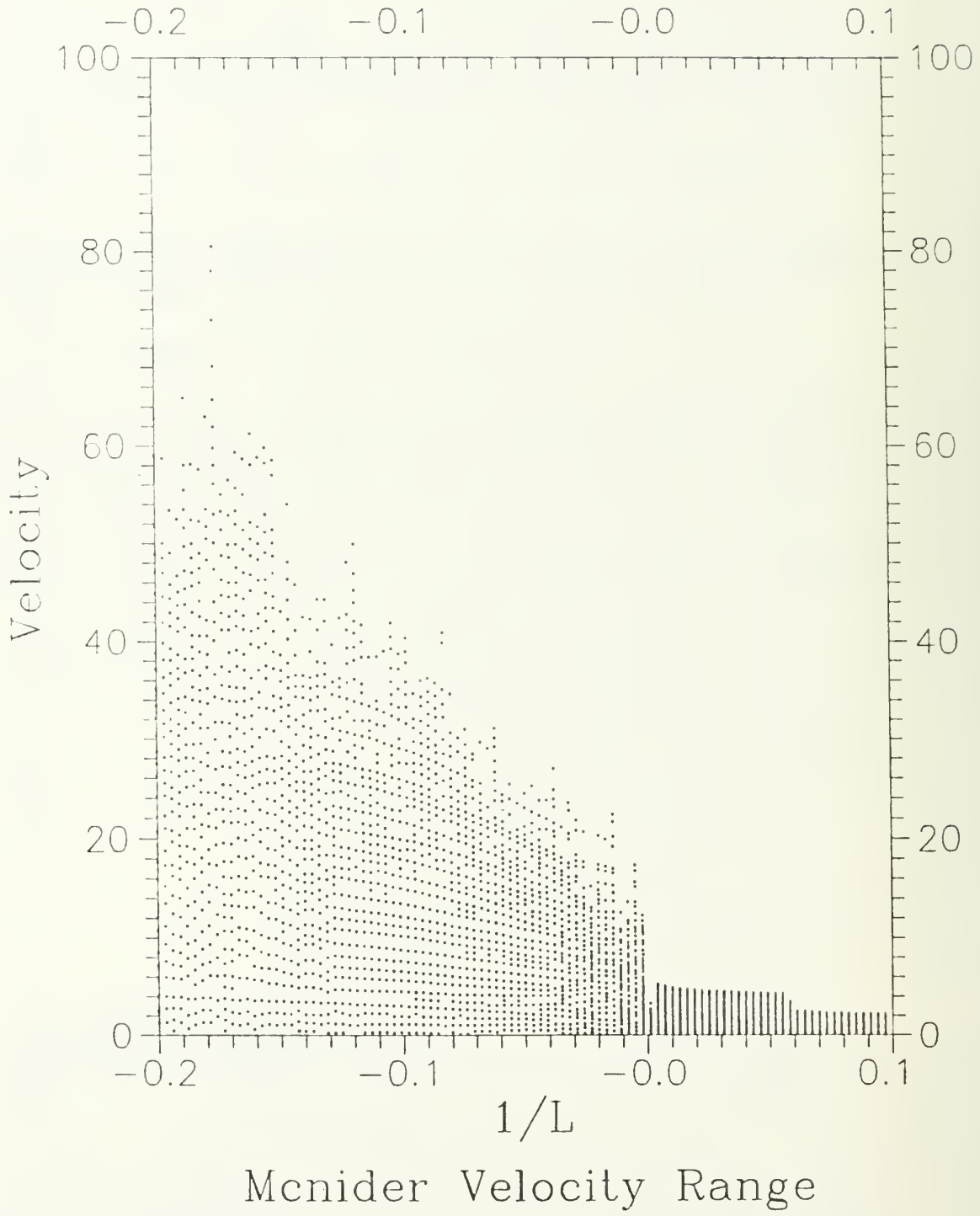

Figure 45. McNider Particle Dispersion Model bifurcation map. Same as fig. 37, except using total velocity in place of total displacement.

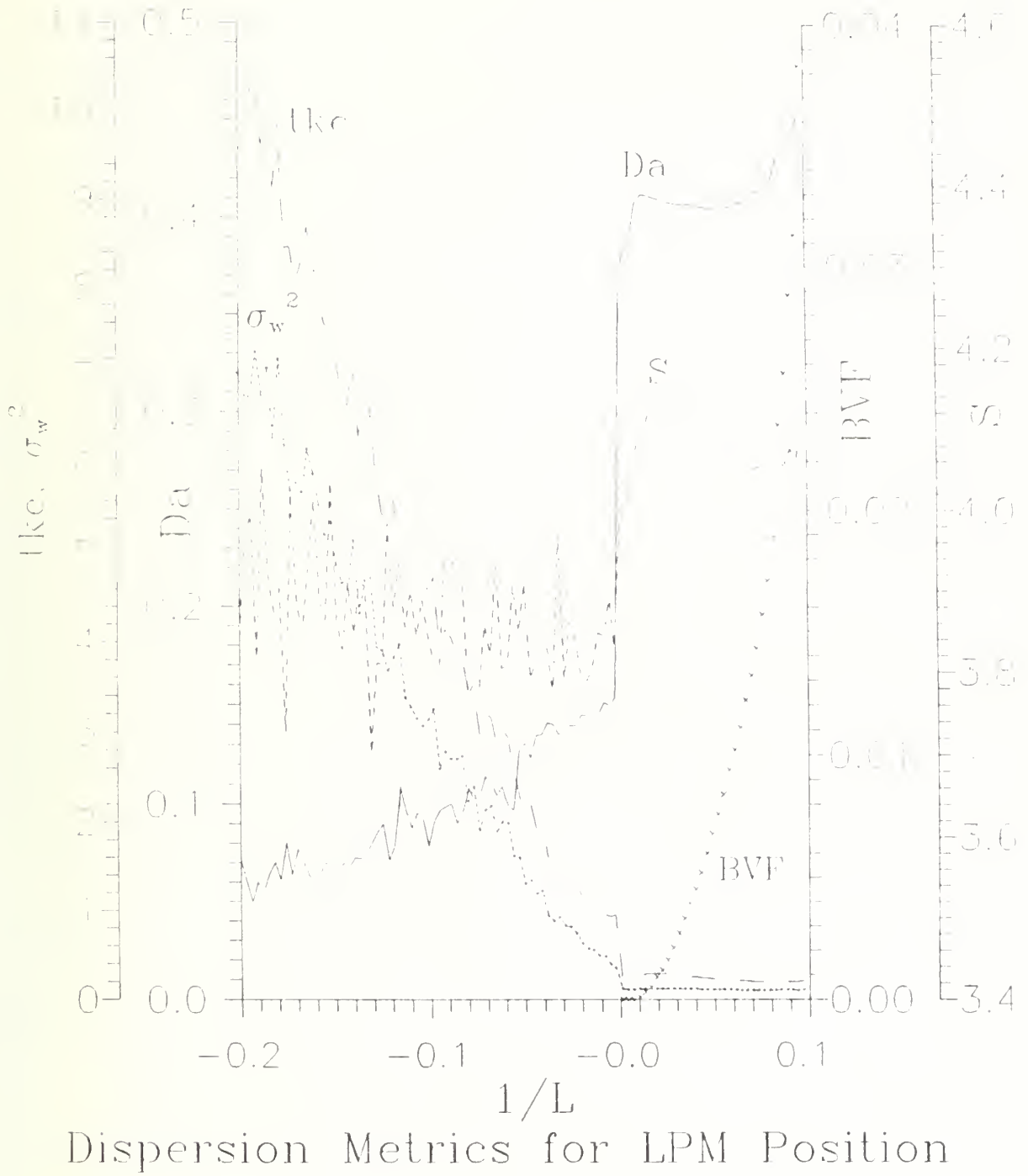

Figure 46. LPM Particle Dispersion Model. D_A, S, σ_w^2, tke, and BVF versus 1/L. Δt = 10 secs.

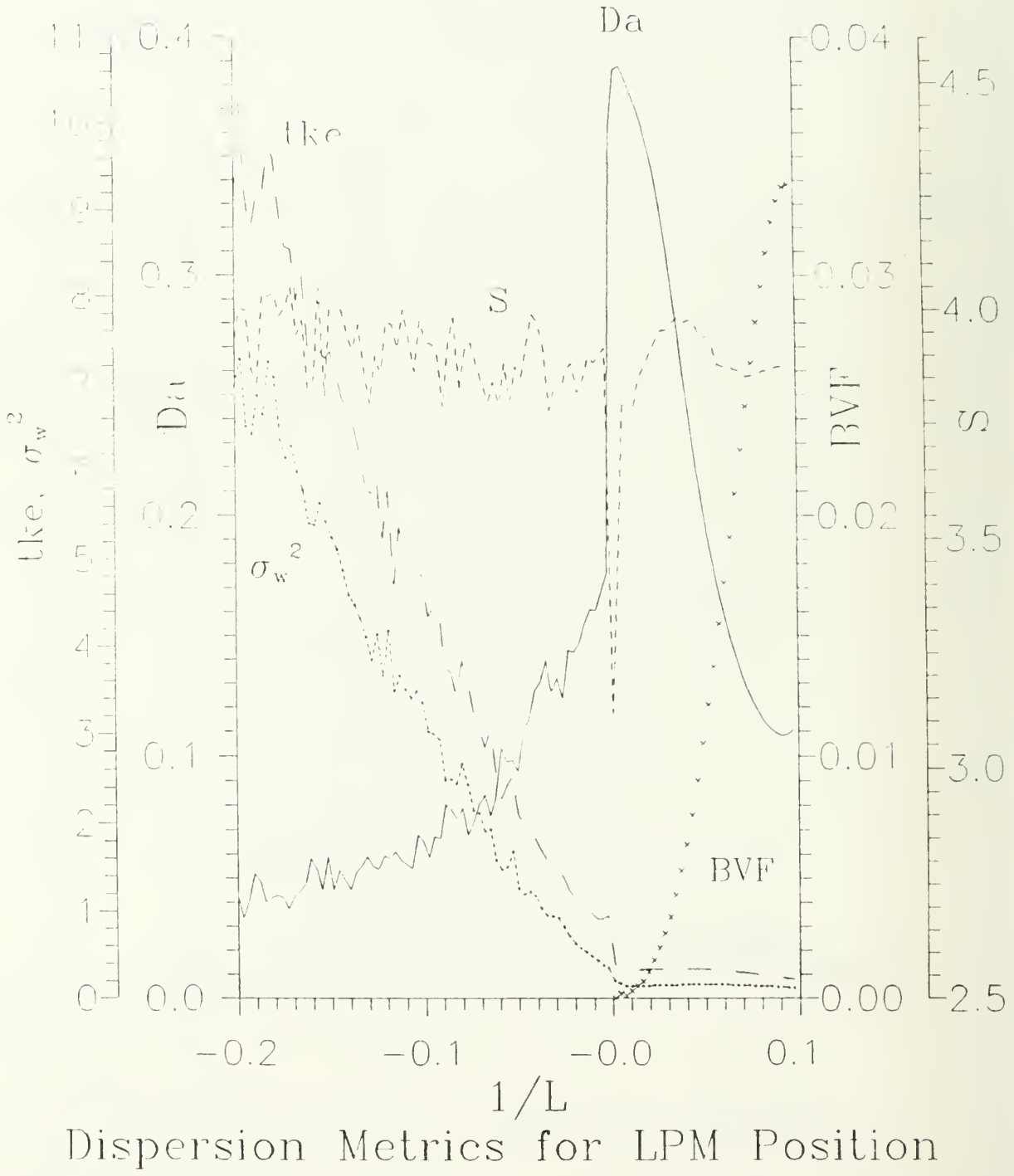

Figure 47. LPM Particle Dispersion Model. D_A, S, σ_w^2, tke, and BVF versus 1/L. $\Delta t = 0.05\ T_L$.

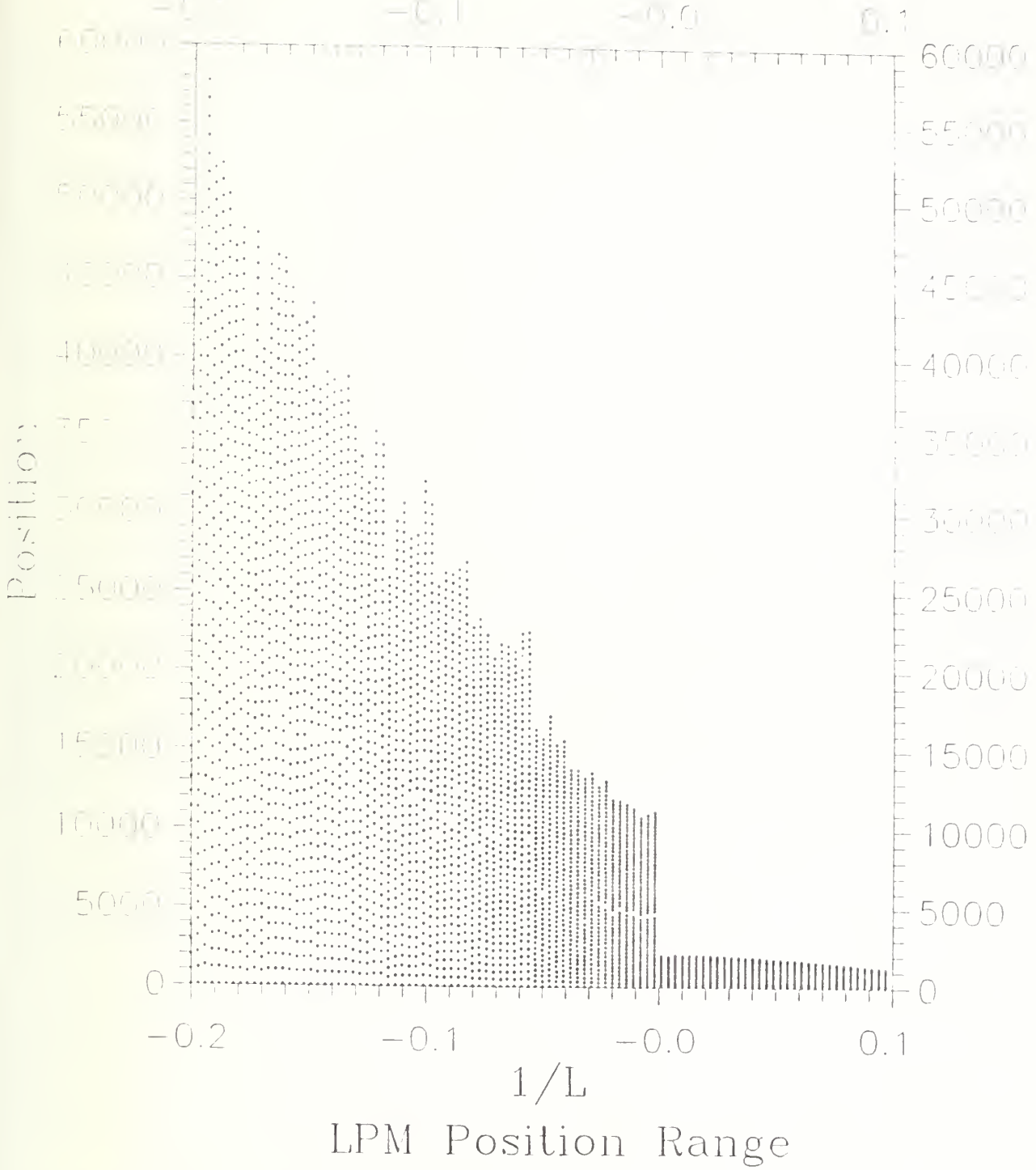

Figure 48. LPM Particle Dispersion Model bifurcation map. Shows total displacement range versus 1/L. Δt = 10 secs.

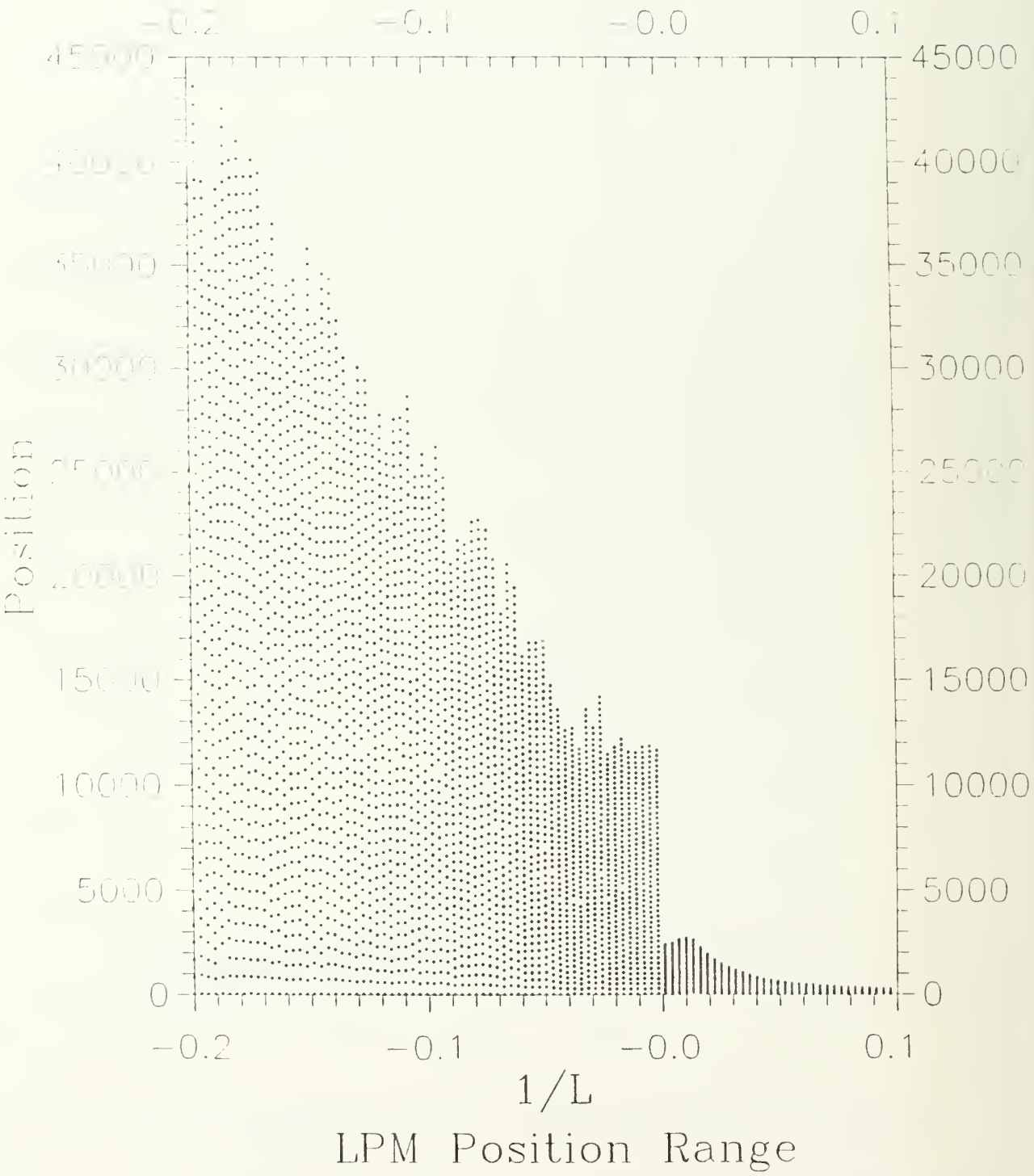

Figure 49. LPM Particle Dispersion Model bifurcation map. Shows total displacement range versus 1/L. $\Delta t = 0.05\ T_L$.

computed differently and are somewhat larger. Another item to note is that the total displacement range is substantially larger, up to roughly 60 km versus 18 km for the McNider model [fig. 36] for the most unstable values. This stems from smaller velocity standard deviations causing larger Lagrangian time scales which result in larger correlation coefficients which in turn induce more correlated and thus directed motions. These LPM results are clearly more in line with expectations for real turbulence. I.e., it is hard to imagine atmospheric plume widths of less than 35 km after ten hours of dispersion, when turbulent velocities are on the order of 20 - 30 ms^{-1} as seen with the McNider model. Yet we see that the LPM still displays some puzzling, as well as unrealistic behavior, when analyzed with chaos metrics. The discontinuities at neutrality for instance seem to stem from the fact that transitions between unstable and stable algorithms are still not seamless. And the slopes do not always display the expected sign.

In fact, when the LPM vertical displacements are segregated, there are decided decreases in S and D_A with Δt = 10 secs in the unstable regime, spikes at neutrality, and recovery with somewhat smoother behavior in the stable regime [fig. 50]. For $\Delta t = 0.05\ T_L$, both S and D_A are roughly constant in the unstable regime, again spike near neutrality, and recover in the mildly unstable region. However, with stronger stability D_A sharply plummets while S increases slightly [fig. 51]. The D_A behavior seems to be a subset of that for the total displacement, while the behavior of S is more difficult to analyze in terms of components.

However, changes in the vertical position range with stability appear to be much smoother for both types of time increments in the LPM model [figs. 52 and 53] than were seen in the McNider model, particularly across the neutral transition [figs. 38 and 39].

When we apply the chaos metrics to the velocity series [figs. 54 and 55], we see that the changes across both types of time increment plots are somewhat less violent than for McNider but perhaps not clearly improved. The main problem again seems to be in attempting to cross the neutral transition with algorithms which have non-overlapping asymptotic values. This is seen quite clearly in the LPM velocity range (bifurcation maps) where a sudden spike occurs just before neutrality [figs. 56 and 57]. Eliminating this kind of error would improve LPM's performance substantially at the chaos micro-level as well as the gross performance level. In fig. 57 a velocity bump also appears at moderate stabilities which seems unrealistic and needs explaining.

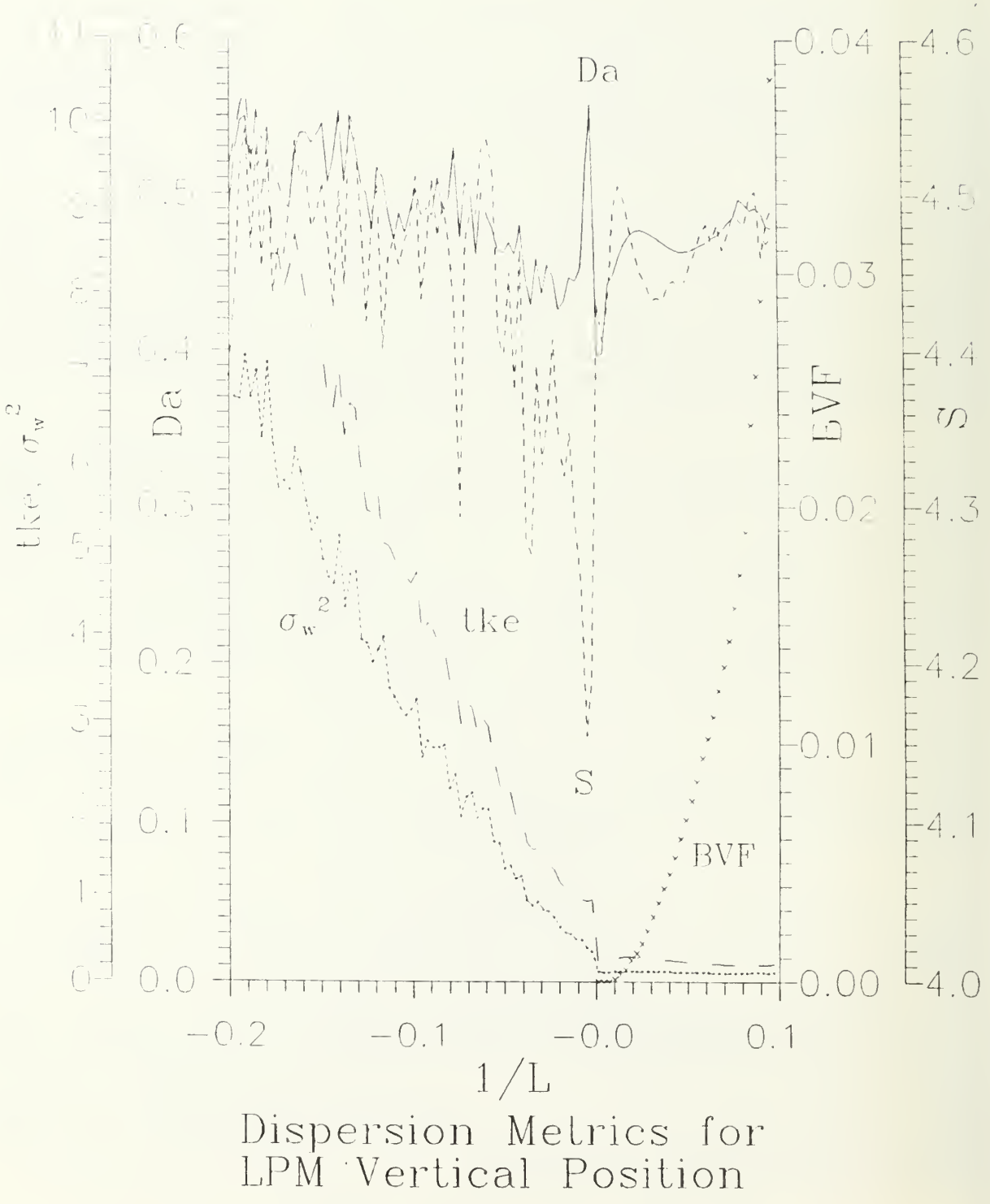

Figure 50. LPM Particle Dispersion Model. Same as fig. 46, except analyzing vertical rather than total displacement.

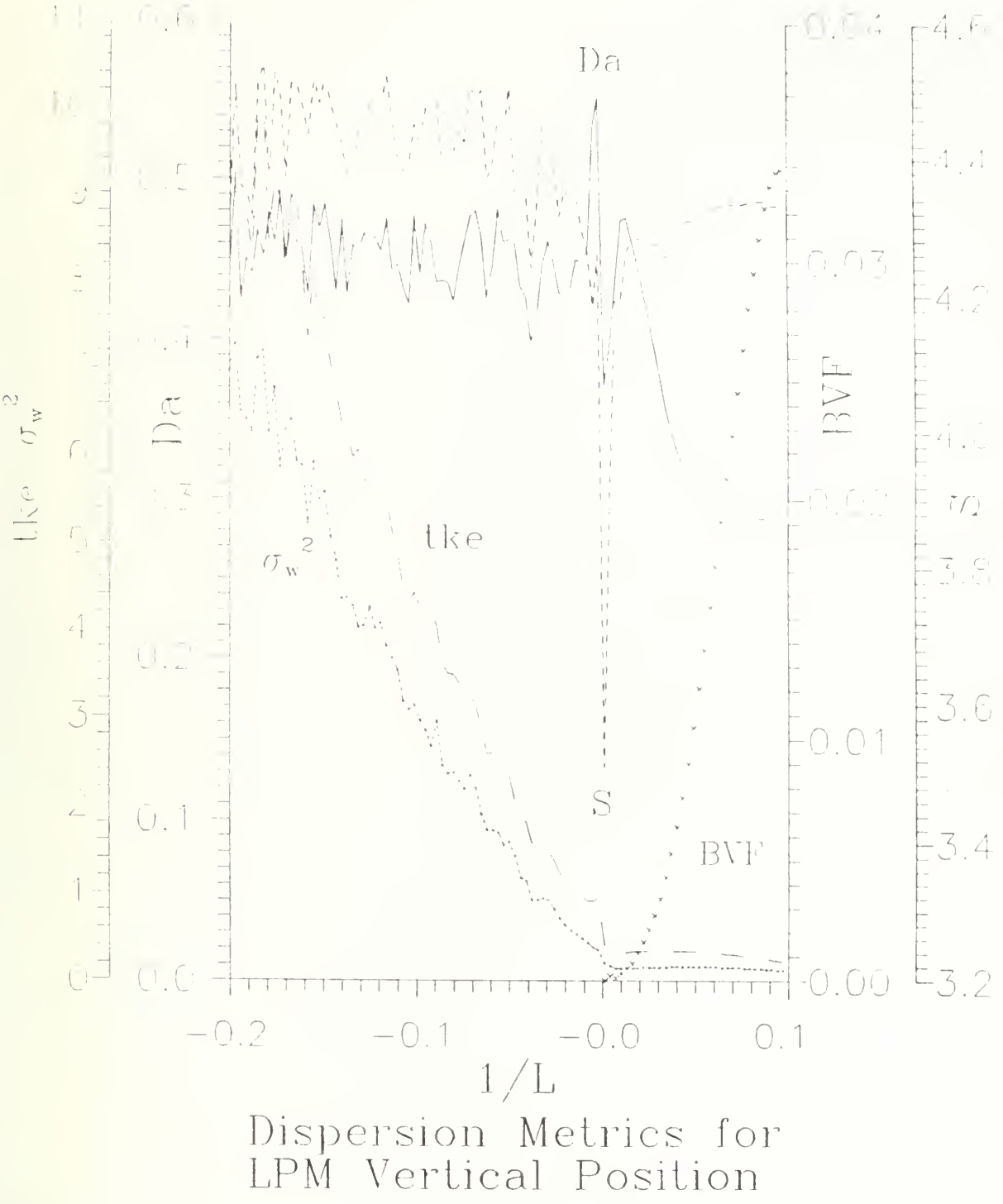

Figure 51. LPM Particle Dispersion Model. Same as fig. 47, except analyzing vertical rather than total displacement.

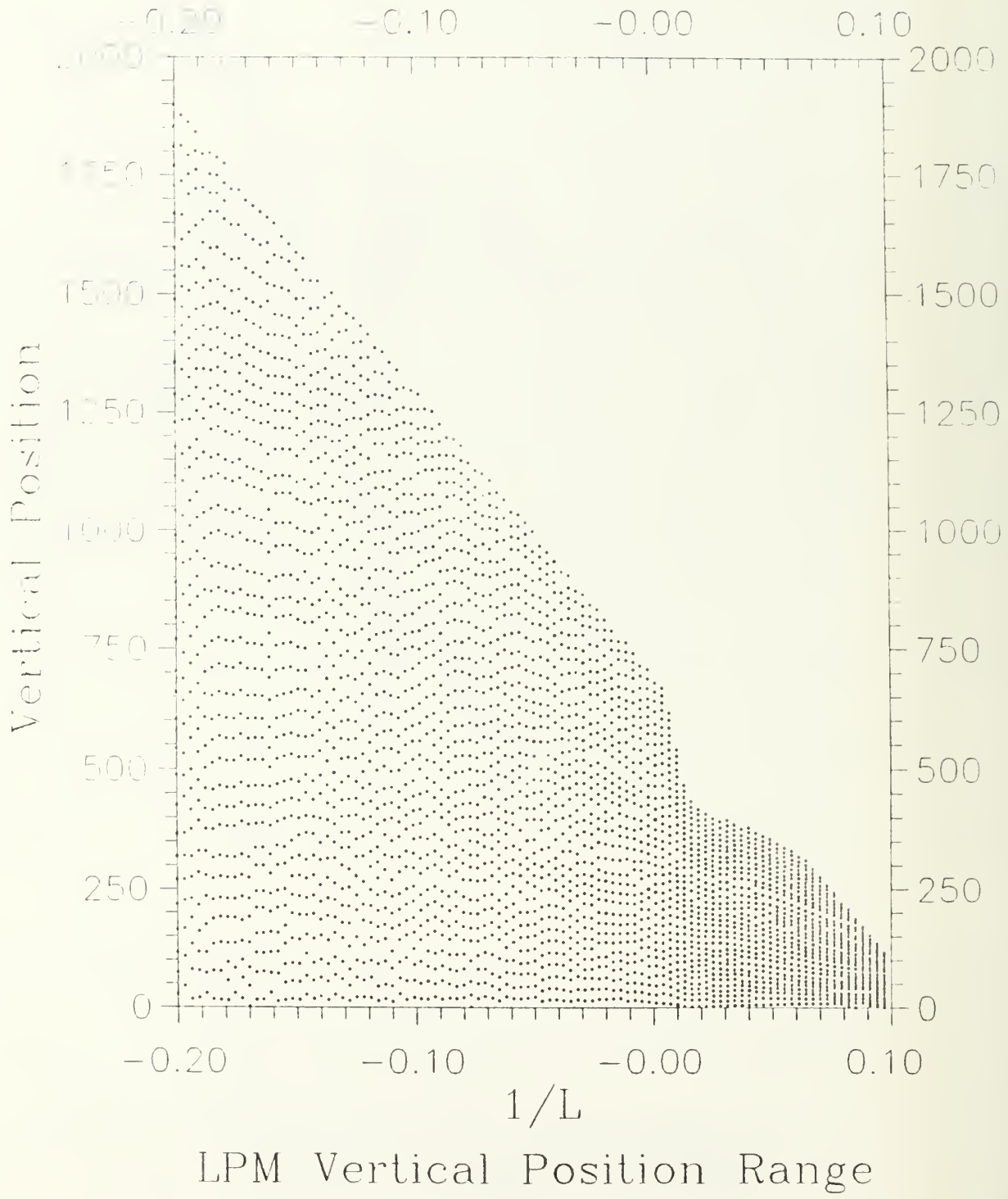

Figure 52. LPM Particle Dispersion Model bifurcation map. Same as fig. 48, except analyzing vertical rather than total displacement.

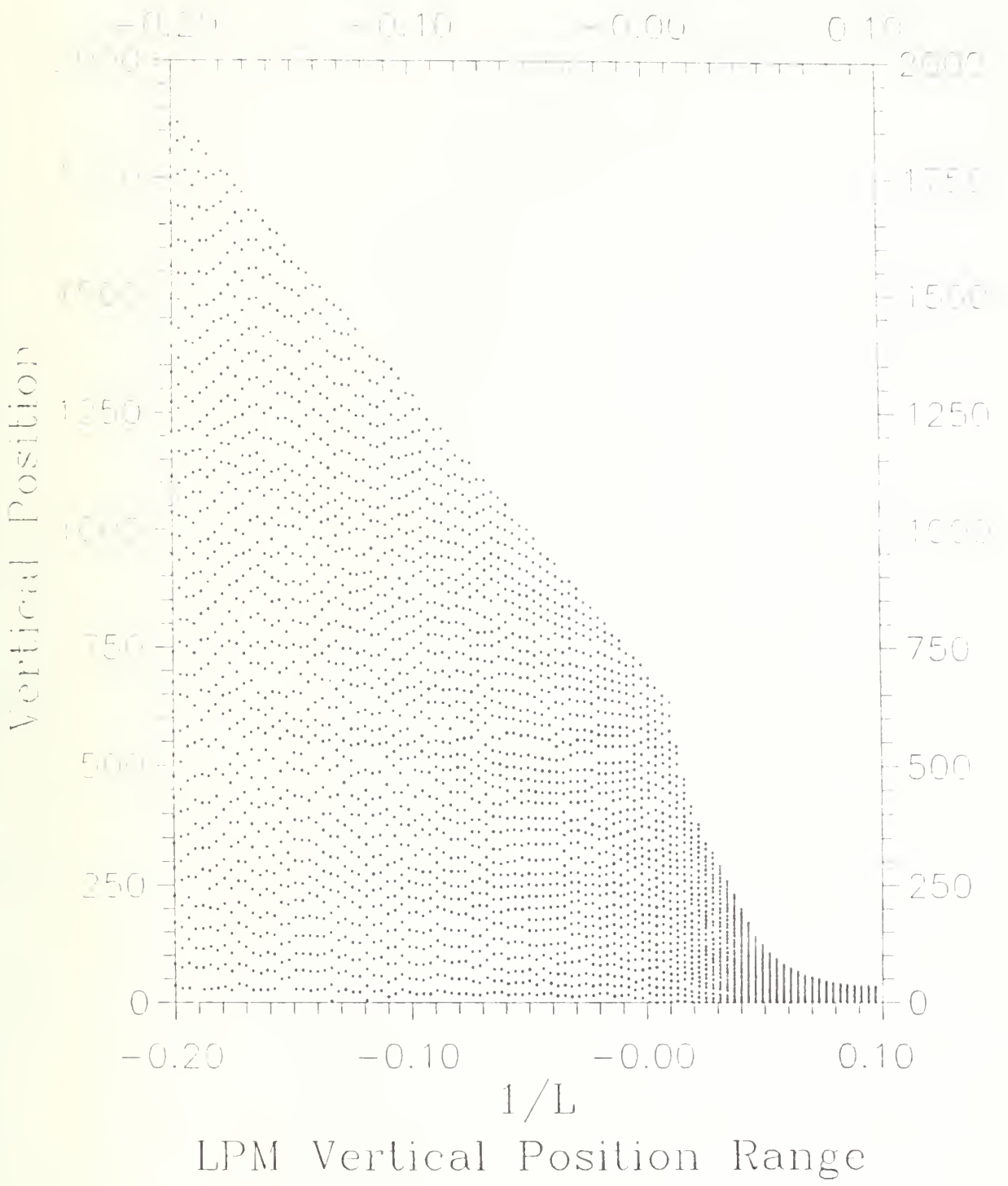

Figure 53. LPM Particle Dispersion Model bifurcation map. Same as fig. 49, except analyzing vertical rather than total displacement.

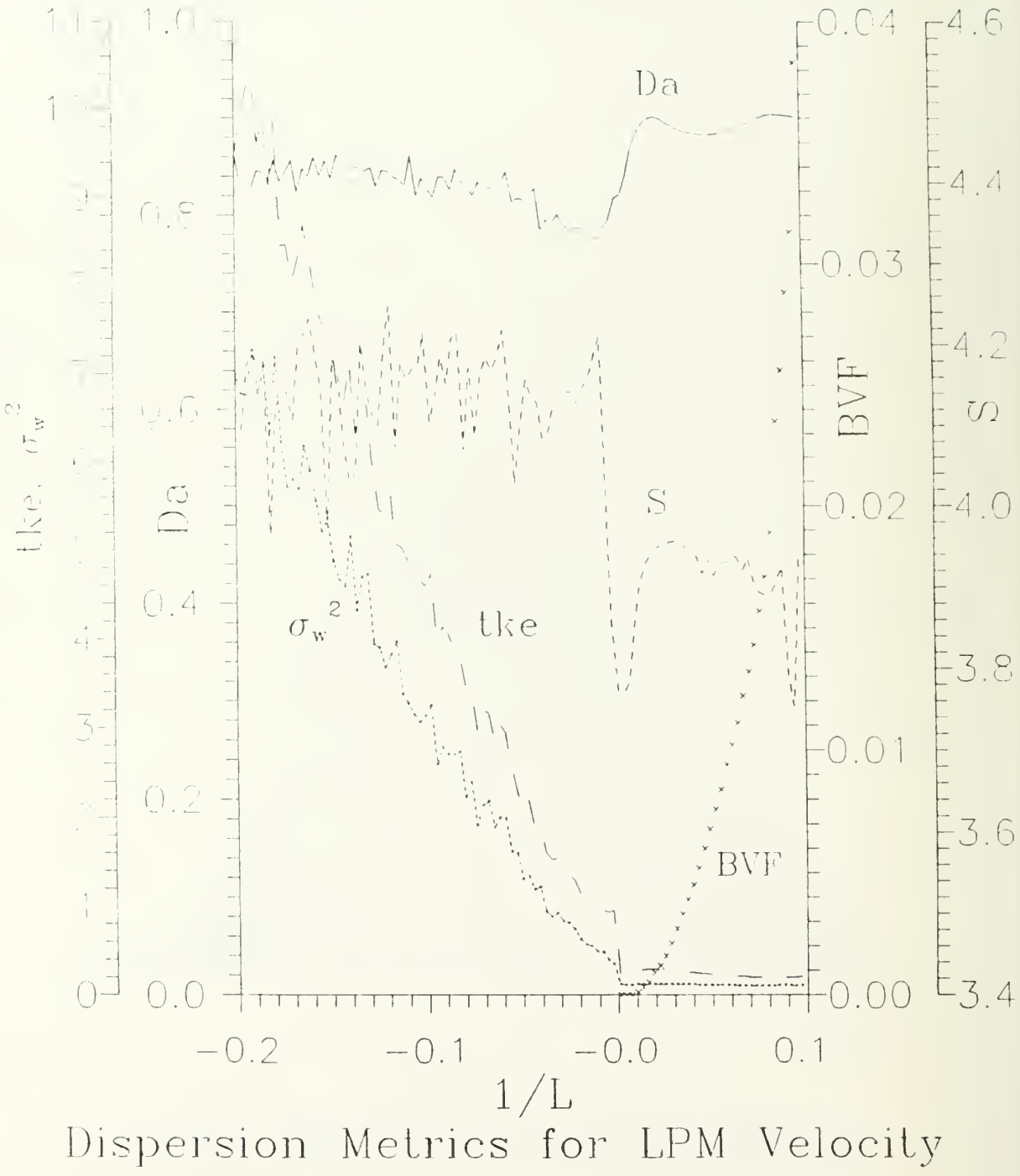

Figure 54. LPM Particle Dispersion Model. Same as fig. 46, except analyzing total velocity rather than displacement.

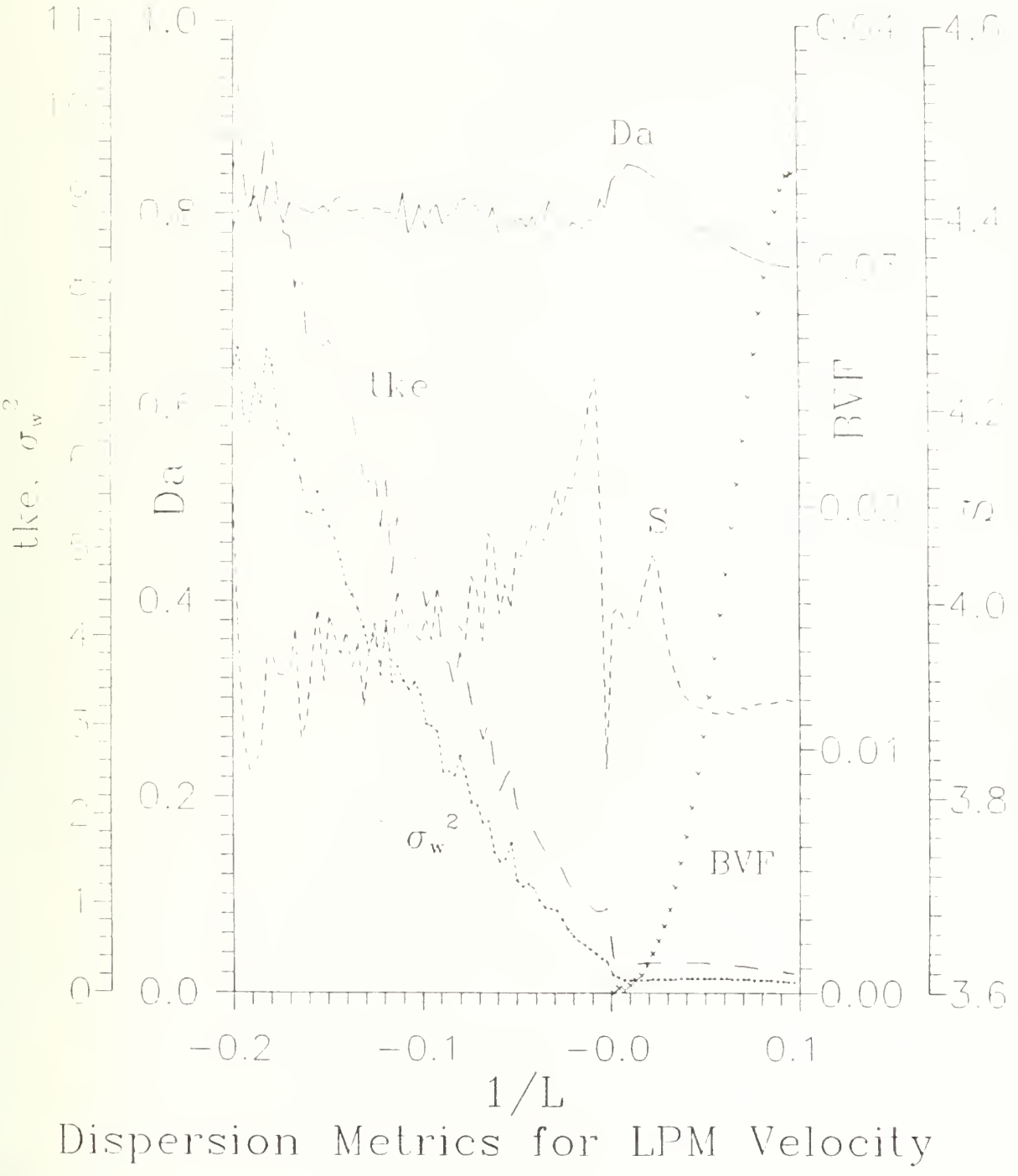

Figure 55. LPM Particle Dispersion Model. Same as fig. 47, except analyzing total velocity rather than displacement.

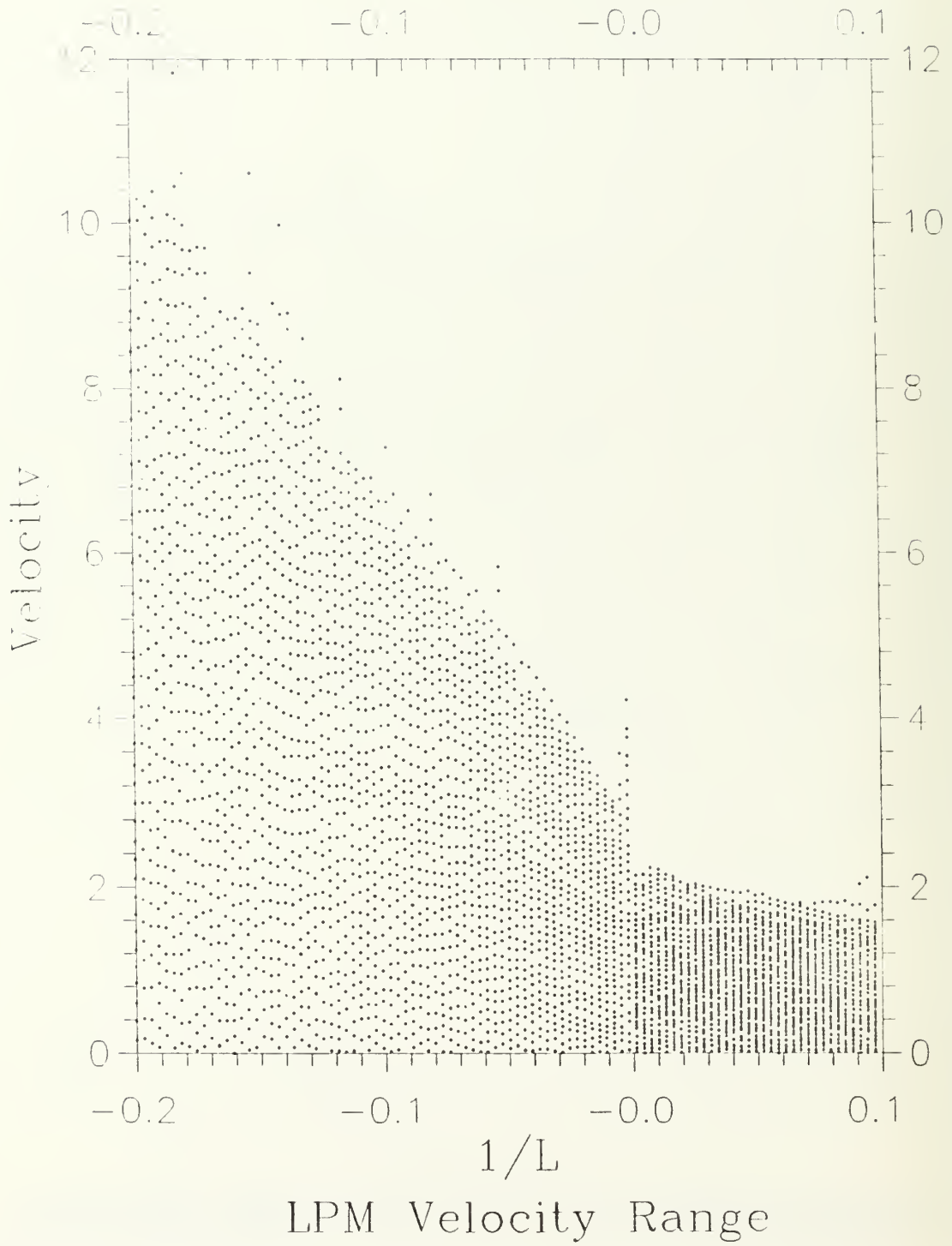

Figure 56. LPM Particle Dispersion Model bifurcation map. Same as fig. 48 except analyzing total velocity rather than displacement.

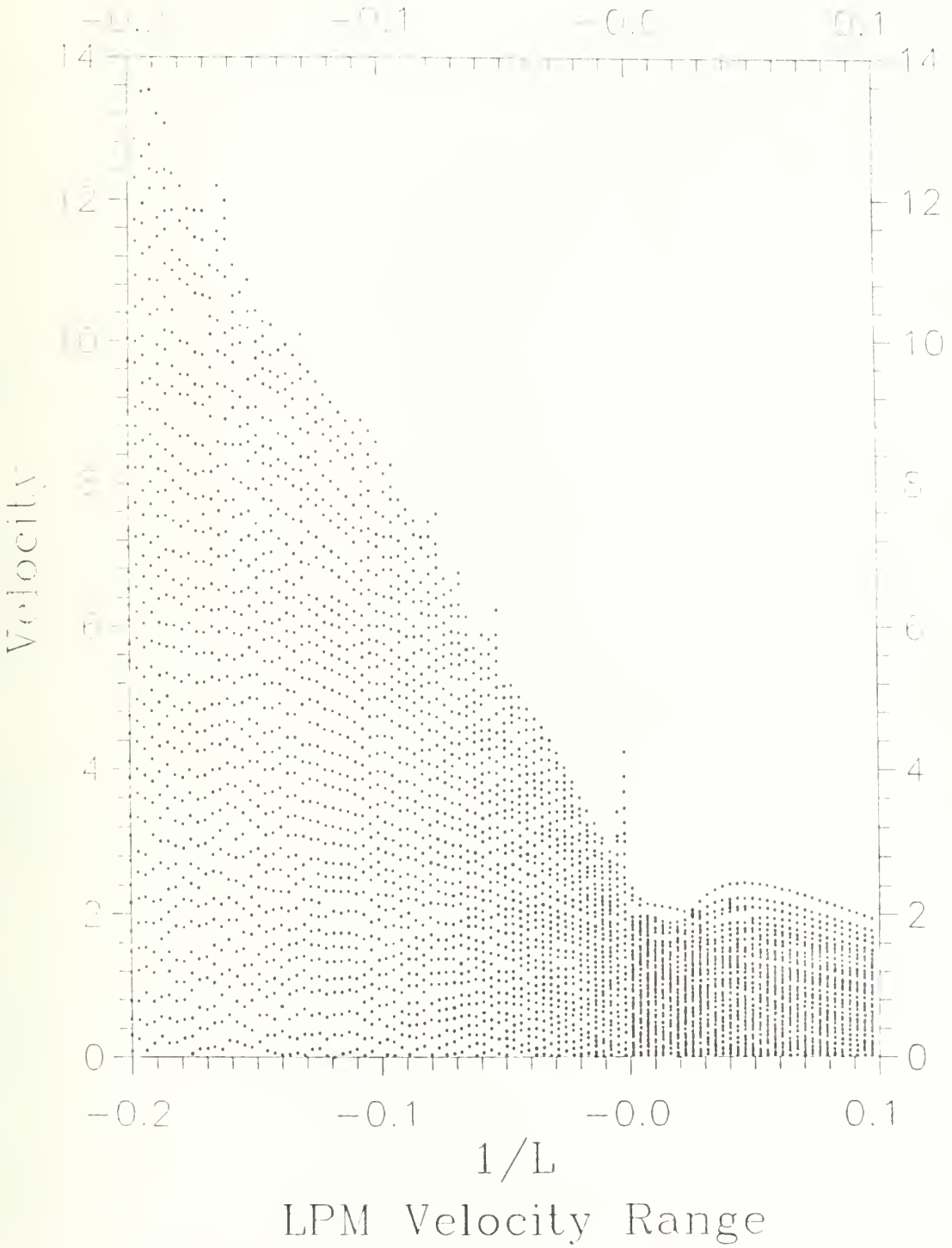

Figure 57. LPM Particle Dispersion Model bifurcation map. Same as fig. 49, except analyzing total velocity rather than displacement.

4. Conclusions from the Atmospheric Diffusion Model Analysis

Most importantly, the above analysis demonstrates that chaos metrics can be a useful new tool in micro-analyzing the behavior of Lagrangian particle models. Absolute values and changes in the values of the Shannon entropy, S, and the self-affine fractal, D_A, over a range of stabilities can illustrate weak points in the algorithms specifying particle motions which might otherwise be overlooked. For example, the turbulence kinetic energy (tke) and vertical velocity variance (σ_w^2) ratios and magnitudes and the particle range maps suggest that LPM is a distinct improvement over the McNider model on the gross diffusion level. However, S and D_A illustrate that LPM displays some remaining problems which prompt further investigation, if the purpose is to truly simulate particle motions in atmospheric turbulence. The results of this study suggest that chaos metrics can be used, not only to assess improvements in the McNider and LPM models, but also to analyze other Lagrangian particle models.

This study is suited to detect discontinuities and slope signs of S and D_A with respect to stability which manifest asymptotic mismatches of values or faulty turbulence algorithms. Changes in chaos metric behavior between constant time steps and ones proportioned by Lagrangian time scale indicate the effect of changes in the mix of random versus correlated motion. These effects are not so apparent when analyzing gross parameters such as tke or velocity variances.

The particle range plots can display the effects of algorithmic discontinuities across the neutral stability transition quite clearly. Peculiarities and weaknesses in Lagrangian particle algorithms can be illustrated by changes in the slopes across the whole band of stability and over particular regimes at both constant time increment and proportioned by Lagrangian time scale.

Both models deviate from the behavior expected in real atmospheric turbulence. E.g., D_A decreases with increasing stability indicate improper simulation of the spectrum of motions, particularly in the McNider model. This may be because the velocity distributions are Gaussian normalized around a single set of component velocity standard deviations. We wonder whether an explicitly spectral model such as Stull's transilient matrix would display more appropriate behavior (Stull, 1988). For the LPM model we note that the general decrease in S for velocities across the unstable/stable transition at constant Δt is in keeping with its expected correlation with the Lyapunov exponent as a measure of turbulent vigor.

IV. OVERALL CONCLUSIONS

Chaos metrics such as the self-affine fractal dimension, D_A, Shannon information entropy, S, and Lyapunov exponent, λ, are shown to be useful tools in the analysis of the characteristics and behavior of Lagrangian particle models. D_A measures the jaggedness of a trajectory, or relative intensity of small versus large scale fluctuations. The Shannon entropy measures the randomness of state distribution. The Lyapunov exponent, difficult to implement in higher dimensions, measures the divergence of trajectories, and leads to a predictability time scale.

The simple one and two-dimensional logistics difference and Henon attractors were studied to ensure that we could reproduce, analyze, and understand classical results before moving to more complex systems. For simple attractors D_A is found to be a good discriminator of low frequencies in data, e.g., periods 2, 4, and 8 of a given length data set. However, at higher frequencies it is difficult to use D_A to distinguish periodicity from chaos. In both the chaos and atmospheric systems, D_A and S often correspond closely, but not always. In the Henon system we occasionally see a sharp drop in S while D_A changes little, implying decreased diffusion as measured by S without concommitant decreases in dispersion as measured by D_A. This suggests that diffusion and dispersion are not equivalent terms nor are they in perpetual agreement, even in the absence of mean flow. In the Henon system we find that $\exp(D_A)$ is often of the same order as S.

These same chaos metrics when used in conjunction with standard geophysical measures such as turbulent kinetic energy, tke, vertical velocity variance, σ_w^2, and the Brunt-Vaisala frequency, BVF, can be applied usefully to atmospheric 3-D particle diffusion models. We find that the behavioral similarities between the simple attractors and more complex atmospheric simulations are striking, as are some of the differences.

In terms of similarities we find that the chaos metrics and bifurcation map algorithms used for the simple attractors can be applied to atmospheric Lagrangian particles virtually without modification. Again, as in the simple attractors, sudden spikes in S, while crossing the neutral transition in the atmospheric models, are usually accompanied by the same or opposite behaviors in D_A. However, in the case of atmospheric models, whether the spikes in D_A are inverted or not may depend as much on the effect of sudden new constraints on larger rather than smaller scale motions. Study of complete motion spectra may resolve such points.

In terms of differences we find that simple periodic motions preceding chaos in classical bifurcatory systems are not wholly

equivalent to laminar wave behavior prior to the onset of turbulence. For example, if the time resolution of the analysis is much shorter than the period, the Shannon entropy for an atmospheric Lagrangian particle model may be quite large for wave motion, but small for periodic behavior. This is because the number of possible states in wave motion is not limited to the amplitude extrema as in bifurcated periodic motion.

With mathematically based simple attractors the distance between successive iterates is not limited by physical constraints. So bifurcations or new solutions can cause sudden spikes in D_A which may not be possible in systems which accurately simulate continuous physical fluids. On the other hand, distances spanned in physical systems are not limited by artificial mathematical constructs such as crossing of the parabolic symmetry fold in the logistics difference equation.

Moreover, since random components in the atmospheric models prevent the appearance of any true periodicity or fixed point attractors, the interpretation of the bifurcation map changes to that of a total range indicater. The density of points within the range maps is too great to assess the degree of randomness by eye, particularly within the stable regime. However, we still see peculiar unexplained empty channels which appear consistently over a range of stabilities, such as in figs. 36, 42, 56, and 57.

Previous performance metrics for atmospheric particle models were only designed to measure aggregate particle behavior. The above chaos metrics also offer some insight into the modeled micro-behavior of individual particles. Results suggest that atmospheric diffusion models require further development at a fundamental level in replicating turbulent diffusion. For example, large fractal dimensions in the McNider model are seen for unstable, rather than stable, conditions, contrary to what seems likely for real turbulence. This points to the neglect in such models of motions at scales other than the dominant scale determined by $\sigma_{u,v,w}$. Thus, atmospheric Lagrangian particle models may simulate only single scale or at most a limited range of large scale diffusion processes. Fluctuations more in accord with real velocity spectra, such as from explicitly spectral models, might display more realistic entropy and fractal behavior. As is, S and D_A behave oppositely at times. This indicates that diffusion and dispersion rates do not have equivalent meaning, even in the absence of mean windflow, not only for the Henon system, but also for complex atmospheric models as well.

The McNider algorithms also display stark inherent discontinuities as the inverse Obukhov length crosses the transition from unstable to stable buoyancy. This sharp discontinuity does not correspond to the real atmosphere, which suggests that model performance

suffers at small values of 1/L. The LPM particle diffusion model's measured performance seems to better reflect reality by somewhat reducing the discontinuity in transition from negative to positive values of 1/L and allowing more reasonable slopes for D_A and S, particularly in the unstable regime. However, the chaos metrics also highlight some remaining problems in LPM which can remain hidden from parameters designed to assess only gross behavior. Complete spectra, higher order moments, and study of intermediate terms may be necessary to complete the analysis. However, this preliminary study shows that chaos metrics can ferret out weaknesses and may be of significant help in testing and improving Lagrangian particle models.

Perhaps the largest missing piece of the puzzle is the lack of data on the micro-behavior of real Lagrangian particles in the atmosphere, or even within wind tunnel and tank simulations with which to compare modeling results. Lagrangian tracer studies using inert gases, smoke, fine particles, and aluminum chaff have all been done in the aggregate, driven by practical concerns regarding the dispersion of toxic clouds and air pollution. Field measurements of single particle motions geared to study turbulence have apparently not been performed. This suggests a need for the development of Lagrangian-based sensing in fluid turbulence experiments. Trackable constant density balloons cannot be made small enough to assess very fine scale motions, but perhaps could be used to analyze a significant range of the spectrum. It may well be possible to laser illuminate and fluorescence track near-microscopic particles in a wind tunnel or water tank. It is certainly possible to track particles in direct Navier-Stokes computer simulations of low order turbulence. Such data have not been pursued, perhaps because no micro-analysis tools previously existed.

Since most current atmospheric data is obtained in the Eulerian rather than Lagrangian frame, the study results suggest that more extended application of chaos metrics to Eulerian measurements of turbulence in real fluids is warranted in order to gauge the performance of Eulerian turbulence models. Such applications need not be restricted to small-scale phenomena, since mesoscale Rayleigh-Benard convection also displays transitions from laminar cellular to chaotic behavior (Agee *et al.*, 1973). Model improvements based on such tests may then be extended to the Lagrangian frame.

With regard to the Eulerian frame, both fractal dimension and Shannon entropy are simple calculations which can be performed real-time *in situ* with current sampling devices, and should be simpler to implement than FFTs, since there are no transform matrices. One area to consider when conducting measurements of the self-affine fractal dimension is the size of both ϵ, the time

increment, and T, the time window width over which the length is being defined. ϵ has a minimum size dictated by the response time of the sensors, while the size of T is critical when looking for intermittent or low frequency events, e.g., gravity waves governed by the Brunt-Vaisala Frequency. If ϵ_{min} is too small, then the time increment will fall in the range where the velocity autocorrelation decay is not exponential but constrained to be parabolic due to continuity and the viscosity of real fluids. At the same time ϵ_{min} must be at least ~ 3 orders of magnitude smaller than T to establish statistical validity. Establishing the appropriate ϵ_{min} is crucial to distinguish waves from turbulence, and probably applies equally for distinguishing intermittent and coherent structures in general (Kamada and DeCaria, 1992 and Kamada 1992b).

We note that the Lyapunov exponent was not employed in the atmospheric Lagrangian particle study due to its complexity in multi-dimensional form. Although difficult to compute in 3-D, λ provides a definite test of chaos in the particle diffusion rate. So a study of all three chaos metrics may be necessary to clarify the relationship of diffusion rate to dispersion rate in these models. At the same time, analysis of our results from the logistic difference equation indicated a perfect correlation between the behavior of the Shannon entropy and Lyapunov exponent, at least in one dimension. Also, the most interesting aspect of Lyapunov behavior is in the transition to low order chaos when the exponent changes sign. We expect the atmospheric simulations to occur mostly at more vigorous turbulence levels where the Lyapunov exponent simply becomes more positive.

Standard geophysical turbulence measures such as tke and σ_w^2 might also be applied to classical chaotic systems such as the logistics difference and Henon equations. The definitions of timescale and averaging time must first be established, e.g., one iteration equals one time unit. The corresponding tke would be zero for a fixed point, and definite magnitude changes would occur as the function bifurcates to periods 2, 4, 8, and to chaos.

The utility of chaos metrics in analyzing the 3-D Monte Carlo based particle diffusion models also suggests the possible study of laminar/turbulent particle motions in other media. These might include plasmas, acoustics, and laser cavities. Solid state free electron gas systems may also find these chaos metrics useful in describing phonon and electron transport. Phonon resonance in crystal lattices also reminds one that particle behavior in lattice gases and cellular automata may be studied with such chaos metrics. These measures might also be useful in modeling gas or liquid phase complex chemical kinetics or radiation which have long been simulated by Monte Carlo schemes.

Agee, A., T. Chen, and K. Dowell, 1973: A review of mesoscale cellular convection. Bull. Amer. Met. Soc., **54**, No. 10, pp. 1004-1012.

Andre, J.C., G. De Moor, P. LaCarrere, G. Therry, and R. du Vachat, 1978: Modeling the 24-hour evolution of the mean and turbulent structures of the planetary boundary layer. J. Atmos. Sci. **35**, pp. 1861-1883.

Baker, G., and J. Gollub, 1990: Chaotic dynamics, Cambridge University Press, Cambridge, MA.

Businger, J.A., 1973: Turbulent transfer in the atmospheric surface layer., Workshop on micrometeorology. ed. D.A. Haugen, American Meteorological Society, Boston, MA, pp. 67-100.

Devaney, R.L., 1990: Chaos, fractals, and dynamics: computer experiments in mathematics. Addison-Wesley Publishing Co., Menlo Park, CA.

Gleich, J., 1987: Chaos: making a new science. Viking Penguin, Inc., New York.

Gould, H., and J. Tobochnik, 1988: An introduction to computer simulation methods, applications to physical systems, part 1. Addison-Wesley Publishing Co., Reading, MA, pp. 151-178.

Grassberger, P., 1986: Estimating the fractal dimensions and entropies of strange attractors., Chaos. ed. A. Holden, Princeton University Press, Princeton, N.J., pp. 291-311.

Kamada, R.F., 1992: Generalizing w_* to mixed forced/free convection in dispersion and boundary layer analyses. Proc. 10th Symp. on Turb. and Diff., Portland, OR, Oct 29-Nov 2.

------, 1992: Multi-fractal analysis of coherent structures in fluid dynamical time series. Proc. 10th Symp. on Turb. and Diff., Portland, OR, Oct 29-Nov 2.

------, 1992: Appendix A: Boundary Layer Parameterizations, from Skupniewicz, C.E., R.F. Kamada, and S.A. Drake, 1992: Lompoc Valley Diffusion Experiment, Final Report. Nav. Postgrad. Sch. Tech. Rep., NPS-ph-92-004.

------ and A.J. DeCaria, 1992: A self-affine multi-fractal wave/turbulence discrimination method using data from single point

fast response sensors in a nocturnal atmospheric boundary layer. Nav. Postgrad. Sch. Tech. Rep., NPS-ph-92-008.

------, and S.A. Drake, 1992: An e-ϵ turbulence closure scheme for mesoscale windflow models with large horizontal/vertical grid aspect ratios. Proc. 10th Symp. on Turb. and Diff., Portland, OR.

Lenschow, D.H., J.C. Wyngaard, and W.T. Pennell, 1980: Mean-field and second-moment budgets in a baroclinic, convective boundary layer. J. Atmos. Sci., **37**, pp. 1313-1326.

Mason, P.J. and D.J. Thompson, 1987: Large eddy simulations of the neutral-static-stability planetary boundary layer. Quart. J. Roy. Meteor. Soc., **113**, pp. 413-443.

McHardy, I., and B. Czerny, 1987: Fractal X-ray time variability and spectral invariance of the Seyfert galaxy NGC5506. Nature, **325**, pp. 696-698.

McNider, R., M. Moran, and R. Pielke, 1988: Influence of diurnal and inertial boundary-layer oscillations on long-range dispersion. Atmos. Environ., **22**, No. 11, pp. 2445-2462.

Panofsky, H., and J. Dutton, 1984: Atmospheric Turbulence. Wiley, New York.

Pielke, R.A., 1984: Mesoscale meteorological modeling. Academic Press, Orlando, FL, pp. 173-186.

Sorbjan, Z., 1990: Structure of the atmospheric boundary layer. Prentice-Hall, Inc., Englewood Cliffs, N.J., pp. 67-124.

Stull, R., 1988: An introduction to boundary layer meteorology. Kluwer Academic Publishers, Dordrecht, The Netherlands.

Therry, G. and P. Lacarrere, 1983: Improving the eddy kinetic energy model for planetary boundary layer description. Boundary Layer Meteorol., **25**, pp. 63-88.

Tribus, M., and E. McIrvine, 1971: Energy and information. Sci. Am., **224**, No. 3, pp. 179-188.

Venkatram, A., and J. Wyngaard, 1988: Lectures on air pollution modeling. American Meteorological Society, Boston, MA, pp. 39-61.

Wolf, A., 1986: Quantifying chaos with Lyapunov exponents. Chaos. ed. A. Holden, Princeton University Press, Princeton, N.J., pp. 273-290.

DISTRIBUTION LIST	No. of Copies
Defense Technical Information Center Cameron Station Alexandria, VA 22314	2
Dudley Knox Library Naval Postgraduate School Monterey, CA 93943-5000	2
Director of Research (012) Naval Postgraduate School Monterey, CA 93943-5000	1
Dept. of Physics (PH) Naval Postgraduate School Monterey, CA 93943-5000	2
Dr. Ray Kamada/phkd Naval Postgraduate School Monterey, CA 93943-5100	9
Mr. Steve Arnold and Davis Downing Geodynamics Corp. PO Box 5548 Vandenberg AFB, CA 93437	1
Drs. Steve Burke and Ted Tsui Naval Research Laboratory Monterey, CA 93943-5006	2
Dr. Ron Meyers US Army Atmospheric Sciences Lab SLCAS-BA-M White Sands Missile Range, NM 88002-5501	1
Profs. John Carroll and Roger Shaw Dept. of Land, Air, and Water Resources Hoagland Hall University of California at Davis Davis, CA 95616	2
Drs. D Ermak, P. Gudiksen, and R. Lange Lawrence Livermore National Lab P.O. Box 808, L-262 Livermore, CA 94550	3
Dr. Roger Gibbs Naval Surface Warfare Center Dahlgren, Virginia 22448-5000	1

Mr. Bart Lundblad and Lt. Matthew Willis 2
Chemical Systems Directorate
Space Launch Vehicle Operations
Box 92957, Los Angeles, CA 90009-2957

Mr. George Lai 1
NASA
Goddard Space Flight Center
Greenbelt, Maryland

Prof. Monique LeClerc 1
Dept. of Physics
University of Quebec at Montreal
P.O. Box 8888, Station A, H3C 3P8
Montreal, Quebec, Canada

Mr. Frank Ludwig 1
SRI, Int.
Menlo Park, CA 94025

Dr. Walt Lyons 1
ASTeR
Atmospheric Science Dept.
Colorado State University
Fort Collins, CO 80524

Prof. Larry Mahrt 1
Dept. of Atmospheric Science
Oregon State University
Corvallis, OR 97331-2209

Mr. Larry Mendenhall 1
Geodynamics Corp.
21171 Western Ave
Suite 100
Torrence, CA 90501

Drs. Torben Mikkelsen, Soren Larsen, Mathias 3
Meteorology and Wind Energy Dept.
RISO National Laboratory
DK 4000 Roskilde, Denmark

Mr. Randall Nyman 1
ACTA
Vandenberg AFB, CA 93437-5000

Drs. K. S. Rao and C. J. Nappo 2
Atmospheric Turbulence and Diffusion Division
NOAA/ARL
P.O. Box 2456
Oak Ridge, TN 37831

Dr. D. O. Revelle
Meteorology Program
Northern Illinois University
DeKalb, Illinois 60115-2584 1

Mr. Steve Sambol
(30 WS/WES) Bldg. 21150
Vandenberg AFB, CA 93437-5000 1

Dr. Brian Sawford
CSIRO Division of Atmospheric Research
Private Bag No. 1
Mordialloc, VIC 3195, Australia 1

Prof. Gordon Schacher
Dean of Faculty and Graduate Studies
Naval Postgraduate School
Monterey, CA 93943-5100 1

Col. David Schmargie (ET)
Vandenberg AFB, CA 93437-5000 1

Dr. D.G. Steyn
Atmospheric Science Program
Dept. of Geography
University of British Columbia
1984 West Mall
Vancouver, B. C.
Canada V6T 1Z2 1

Prof. Roland Stull
Dept. of Atmospheric Science
University of Wisconsin
1225 Dayton St.
Madison, WI 53706 1

Dr. Saffet Tanrikulu
California Air Resources Board
Box 2815
Sacramento, CA 95812 1

Dr. J. C. Weil
NCAR
P.O. Box 3000
Boulder, CO 80307 1

Dr. Tetsuji Yamada
Yamada Science and Art
147 Monterey Bay Dr. S.
Los Alamos, NM 87544 1

DUDLEY KNOX LIBRARY
3 2768 00392850 8